12-2014

# Investigations into Ambient Ionization Mechanisms: Electrospray Ionization and Direct Analysis in Real Time Mass Spectrometry

Stephen Colin Gibson
*University of Tennessee - Knoxville*, sgibso12@vols.utk.edu

To the Graduate Council:

I am submitting herewith a dissertation written by Stephen Colin Gibson entitled "Investigations into Ambient Ionization Mechanisms: Electrospray Ionization and Direct Analysis in Real Time Mass Spectrometry." I have examined the final electronic copy of this dissertation for form and content and recommend that it be accepted in partial fulfillment of the requirements for the degree of Doctor of Philosophy, with a major in Chemistry.

Charles S. Feigerle, Major Professor

We have read this dissertation and recommend its acceptance:

Kelsey D. Cook, Michael J. Sepaniak, Elias J. Fernandez

Accepted for the Council:
Carolyn R. Hodges

Vice Provost and Dean of the Graduate School

(Original signatures are on file with official student records.)

# Investigations into Ambient Ionization Mechanisms: Electrospray Ionization and Direct Analysis in Real Time Mass Spectrometry

A Dissertation Presented for the

Doctor of Philosophy

Degree

The University of Tennessee, Knoxville

Stephen Colin Gibson

December 2014

## Dedication

*To my Mother, who would give up everything so I may be enabled to do anything.*

*To my Father and his memory, for his unconditional love for me.*

## Acknowledgements

As my graduate school career comes to a close, I realize I've been humbled to meet so many people that have influenced my life greatly, both professionally and personally. First and foremost on that list are Dr. Kelsey Cook and Dr. Charles Feigerle, my co-advisors. I cannot thank them enough for their guidance, compassion, patience, support, encouragement, and advice over the years. I have never met two more hardworking men who are both fully dedicated to their science and families. I have learned more in my time under their tutelage about how to think critically and conduct scientific research than I knew was possible. Also, I am very appreciative of Dr. Michael Sepaniak and Dr. Elias Fernandez for their support as committee members and taking the time to read this long, yet incredibly insightful document! I'd also like to thank Dr. Jon Camden, a professor who served on my committee through my ORP defense and until his departure from UT.

I'd like to thank University of Tennessee's Department of Chemistry for their financial support by offering me teaching and student operator assistantships throughout my graduate career. These assistantships afforded me the opportunity to regularly work with two other individuals that had a large effect on my graduate school career: Dr. Liguo Song and Dr. Yvette Yang. Dr. Song, Director of UT's Center for Mass Spectrometry, was my supervisor during my part time assistantship as student operator in the Center. He was always supportive as I learned the instrumentation, understanding if I had other obligations to which I needed to attend, and always gave me opportunities to expand myself scientifically whenever I

wanted. His guidance and opportunities in the Center allowed me to become a greatly more versatile scientist. Dr. Yang, whom I taught under for most of my graduate career, was incredibly easy to work with. Her kindness and generosity will always be remembered.

Although not on my committee, I'd also like to thank Dr. John Bartmess, Dr. Frank Vogt, and Dr. Ziling Xue for their support and guidance over my graduate school career.

Over the years, there has been so many special staff working for the department in the business office, main office, general chemistry office, and other various locations. I cannot thank Bill Gurley, Gary Wynn, Jim Murphy, and Johnny Jones enough for their technical expertise over the years. Rhonda Wallace, Pam Roach, Darrell Lay, Gail Cox, Rachel Rui, Jill Bodenheimer, Lisa Bonds, Sharron Marshall, Marilyn Ownby, Carol Bartmess, Holley Pickett, Traymond Allen, and Jessica VanBrunt have all been extremely helpful in any logistical issue I needed resolved.

Fellow graduate students have helped provide incalculable amounts of support throughout the years. The friendships of Becky and Jon Horton, Eddy Duranty, and Red Camp continue to be invaluable to me every day and I could not imagine getting through graduate school without their love. I thank group members Eric Barrowclough, Alexis Dale, Amber Moody, Andrew Dykstra, Julia Abbott, Meredith Therrien, and Daniel Brasfield for their advice and friendship. Stefanie Bragg and Belinda Lady provided the necessary support from fellow WKU alumni.

Few people understand the greatness that is Big Red like they do. I'd also like to extend a thank you to those friends and colleagues who helped along the way: Zhenqian Zhu, Kelly Hall, Michael Peretich, Heidi Bostic, David Cho, Adam Imel, Adam Lamb, Sam Rosalina, Jonathan Fong, Sabrina Wells, and Royce Dansby-Sparks.

My past influences include Dr. Kevin Williams, Dr. Les Pesterfield, Dr. Darwin Dahl, Dr. Robert Holman, and Alicia McDaniel from Western Kentucky. They helped ignite my passion for chemistry that continues today.

I thank my friends from high school and college: Chris Fuller, Nathan McClure, Mark Goudie, Jason and Jessica Gibson, Richard Hayes, and Justin Schmitt to provide balance outside of graduate school. Whenever I discussed school, they likely had no idea what I was talking about, but they were unconditionally encouraging throughout.

Last but certainly not least, I must thank my family for their love and understanding as I made it seem like I was inadvertently neglecting them over the past few years. Their words of encouragement and patience with me and my schedule have been incredible. My parents, Barbara and Bob Gibson, allowed me to do whatever I wanted to do as long as I was happy. It's impossible to repay them for their love, so the best I can do is pass it forward to everyone I am able.

## Abstract

Mass spectrometry (MS) is an important tool for chemical analyses. Despite the MS requirement for generation of analyte gas-phase ions, many ion source designs afford little-to-no fragmentation, allowing characterization of intact molecules. However, this does not assure that detected ions are representative of the analytes' natural state. Ionization mechanisms are generally complex and rarely fully understood. Fundamental research into these mechanisms provides greater insight into the relationship between solution chemistry and mass spectra. Work herein addresses aspects of two ambient ionization mechanisms: electrospray ionization (ESI) and Direct Analysis in Real Time (DART).

Ions produced by ESI are dispersed into a fine aerosol to encourage droplet evaporation, ultimately resulting in bare gaseous ions. Evaporation will induce cooling of emitted droplets over time. In this research, ratiometric fluorescence thermometry was used to probe droplet temperature evolution, and to assess whether it is adequate to impact probed equilibria. Under typical ESI conditions, droplet temperatures were observed to decrease ~30 K axially within ~0-5 mm from the emitter, before rewarming ~3 K over ~5 mm. These profiles were fit using diffusion- and surface-controlled evaporation models. Both fit well, ($R \geq 0.994$), but the latter required unrealistic droplet radii for a good fit. In lateral profiles near the emitter tip, temperatures are lower in the periphery than on-axis (by ≤ 10 K), consistent with expected enrichment of the spray periphery with smaller droplets. At longer axial distances, lateral profiles were relatively flat. At lower flow rates,

droplet temperature was observed to fall more rapidly, possibly attributable to changes in droplet size and/or velocity with flow rate.

DART studies of selected compounds in a range of solvents were performed to assess gas-phase ion chemical effects on the relationship between detected ion abundances and bulk solution composition. When the DART gas stream contacts a sample solution, desorption/ionization of the matrix can inhibit analyte ionization, suppressing analyte signal. The effect depends on the components' relative proton affinity and ionization energy. This effect was determined to be present with quantities ≥ 10 nL liquid or 10 μg [microgram] solid and at analyte-to-matrix ratios less than 1:100.

# Table of Contents

# List of Tables

# List of Figures

# List of Schemes

# Chapter 1. Introduction

## 1.1 Motivation

Mass spectrometry (MS) is an analytical technique used to rapidly and selectively detect and determine the abundance and mass-to-charge ratio (m/z) of ions in the gas phase.[1] It can provide detailed structural information[2] by detecting fragments of the molecule that correspond to discrete groups of atoms that compose a molecule. MS has successfully been coupled to a variety of analytical techniques, most notably capillary electrophoresis,[3] gas chromatography,[4] and liquid chromatography,[5] in order to reduce sample complexity and to ease interpretation. Most recently, the robust nature of MS has provided solutions to biochemical problems, namely in the biochemical fields of proteomics,[6] metabolomics,[7] and lipidomics.[8] MS is also heavily used in the analysis of natural products,[9] polymeric systems,[10] and inorganic chemicals.[11] Using MS for high throughput drug discovery[12] reduces method development times when compared with traditional methods that require incorporation of fluorescent labels, radiolabels, or coupling assays. Process monitoring[13] relies heavily on mass spectrometry for on-line measurements of trace components in medical and food applications as well as analysis and control of industrial processes. Mass spectrometry is also heavily used in forensic science[14] for molecules such as drugs and poisons in addition to sequencing deoxyribonucleic acid (DNA). The ion-molecule reactions[15] of gas phase biochemical transformations and metal-centered catalytic species are easily probed using common MS ion sources in order to enhance fundamental understanding of

organic and inorganic reactions. This is by no means an exhaustive list of the applications of this type of analytical instrumentation.

A typical mass spectrometer typically consists[1] of three components:

1) An ionization source, which ionizes analytes and assists in transferring created ions into the gas phase;
2) A mass analyzer, a device that separates ions based on their m/z value by using an electric field;
3) A detector, which records charge induced or current produced when an ion passes by or hits a surface.

The ion source fulfills the fundamental need of mass spectrometry that the ions exist in the gas phase before they can be separated according to their individual mass-to-charge ratio (*m/z*). Prior to 1970, the primary ion sources were electron ionization (EI) and chemical ionization (CI). These sources[1], while still widely used today, are restricted to only volatile, non-thermally labile molecules. However, EI imparts high quantities of residual energy into the analyte molecule, invoking large degrees of fragmentation (the systematic rupturing of bonds in an attempt to remove excess energy in order to restore stability to the resulting ion), which might not always be desired. The shattering of molecules through this sort of technique is called "hard ionization." In contrast, "soft ionization" sources are lower energy processes which typically do not fragment a molecule and result in easily identifiable intact molecular species.[1] CI is a softer ionization technique and has several variations

such as atmospheric pressure chemical ionization[16,17] (APCI) and direct analysis in real time (DART).[18]

In 1968, Dole coupled a soft ionization method, electrospray, to a mass spectrometer to analyze a dilute polymer solution,[19] though this technique did not become popular until the late 1980s. Field ionization[20] and field desorption[21] were first reported by Becky in 1969 and developed into some of the first widely available techniques for ionization and desorption. However, these techniques were very demanding and require very experienced operators.[22] They were soon replaced by techniques such as secondary ion mass spectrometry (SIMS), where a focused primary ion beam ionizes and causes the ejection of secondary ions from a surface, and fast atom bombardment (FAB; also called liquid SIMS),[23] where the analyte is dissolved in a matrix and bombarded with an atom or ion beam. By the end of the 1980s, ambient ionization was ushered in by the ground-breaking paper by John Fenn describing the use of electrospray ionization in the analysis of biological macromolecules.[24] In 2002, the Nobel Prize in Chemistry was awarded to three scientists for contributions to developing new methods for protein analysis: Fenn for electrospray, Koichi Tanaka for matrix-assisted laser desorption[25] (MALDI), and Kurt Wuthrich for nuclear magnetic resonance[26] (NMR).

ESI introduced many new features[1] to the field of mass spectrometry, including:

a) A means of producing ions from nonvolatile, thermally labile compounds;

b) An easy method to produce multiply-charged ions, which allows molecules/proteins with molecular weights up to thousands of Daltons to fall within the range of commonly used mass spectrometers;
c) The ability to act as an extremely efficient interface for LC/MS;
d) Permitting the investigation of non-covalent associations of molecules, such as proteins;
e) A relatively soft ionization mechanism, allowing analysis of intact molecules; and
f) The ability to directly analyze inorganic cations and anions, which provides information on valance state and molecular formulation.

The robustness of ESI helped usher in the use of numerous atmospheric pressure ionization (API) methods that easily coupled with liquid chromatography (LC) such as atmospheric pressure chemical ionization (APCI)[16] and atmospheric pressure photoionization (APPI).[27,28] Recently, the other API methods that do not require LC, such as desorption electrospray ionization (DESI[29]; Cooks in late 2004) and direct analysis in real time (DART[18]; Cody in early 2005), further moved the ionization process for MS from vacuum into the open-air environment where more samples are present in native forms. Since then, there has been an explosive emergence of these types of ionization techniques including atmospheric solid analysis probe (ASAP)[30], electrospray laser desorption ionization (ELDI)[31], desorption atmospheric pressure chemical ionization (DAPCI)[32], desorption sonic spray ionization (DeSSI)[33], MALDI (matrix assisted laser desorption ionization)

assisted electrospray ionization (MALDESI)[34], neutral desorption extractive electrospray ionization (ND-EESI)[35], desorption atmospheric pressure photoionization (DAPPI)[36], dielectric barrier discharge ionization (DBDI)[37], laser ablation electrospray ionization (LAESI)[38], plasma-assisted desorption ionization (PADI)[39], and flowing afterglow atmospheric pressure glow discharge (APGD) ionization[17], all of which established a new subfield of MS, i.e. open-air desorption/ionization mass spectrometry (OADI-MS).[40,41,42]

Most of the OADI techniques can be related to an API technique by an ionization process, *i.e*. ESI, APCI and APPI, and as such they generate similar mass spectra for the same compounds. ESI-related OADI techniques include DESI[29], ELDI[31], DeSSI[33], MALDESI[34], ND-EESI[35], and LAESI.[38] APCI-related OADI techniques include ASAP[30] and DAPCI[32]. Although DART[18], DBDI[37], PADI[39], and flowing afterglow APGD[17] may have a substantially different source design from APCI, they are still related because their ionization is initiated by electrical discharge in a gas. An APPI-related OADI technique is DAPPI.[36] OADI has the ability to interrogate samples in their native state, which has been proven to be extremely useful in many areas such as homeland security, counterfeit tablet detection, food quality monitoring, art conservation, tissue imaging, forensic analysis, and drug discovery.

The work presented in this dissertation was motivated by the need to improve the understanding of chemistry taking place in ambient ionization sources, namely electrospray ionization (ESI) and direct analysis in real time (DART). This

chapter provides an introduction to ESI and DART with respect to the ionization process, current understanding, and future challenges.

## 1.2 Fundamentals of Electrospray Ionization

Analytes ionized by ESI undergo three major processes at atmospheric pressure: 1) production of charged droplets at the ESI capillary tip[43]; 2) shrinkage of the charged droplets by solvent evaporation and various droplet disintegrations[44,45]; and 3) eventual production of gas-phase ions from very small, charged droplets.[19,46]

### 1.2.1 Mechanism of Electrospray Ionization

ESI is produced by applying a strong electric field (see Section 1.2.2 for discussion on the electrochemistry of electrospray), under atmospheric pressure, to a liquid passing through a conductive capillary (see Figure 1.1). The electric field ($E_c$) produced is approximately given by the following relationship:

$$E_c = \frac{2 \cdot V_c}{r_c \cdot \ln\left(\frac{4 \cdot d}{r_c}\right)} \qquad \text{(Equation 1.1)}$$

where $V_c$ is the applied potential, $r_c$ is the capillary outer radius, and $d$ is the distance from the capillary tip to the counterelectrode. The electric field will penetrate the solution near the capillary tip and cause polarization of the solvent near the meniscus of the liquid. If a polar solvent is used, solvent molecules will align corresponding to their induced dipoles. In the positive-ion mode (ES emitter is operated at a positive voltage; the anode), cations will migrate towards the liquid meniscus while anions move away.

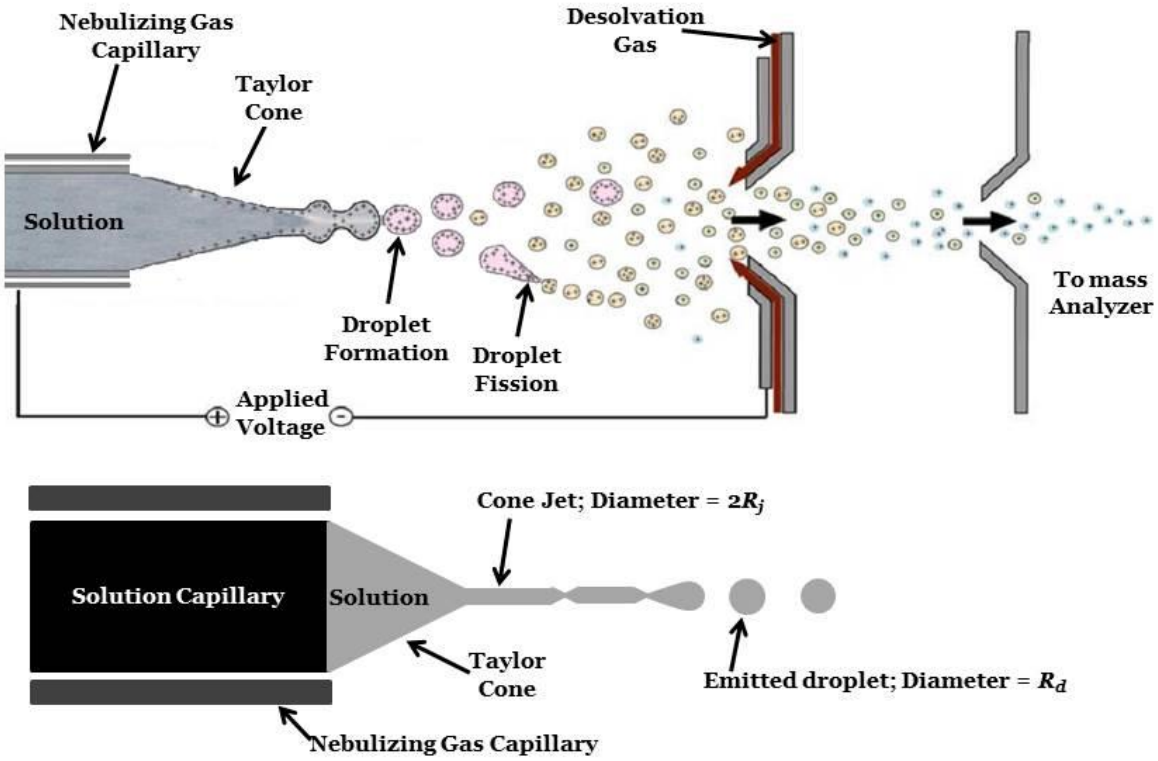


**Figure 1.1:** Top: Schematic of the major processes occurring in electrospray ionization. Adapted from Ref **47**. Bottom: Zoomed in schematic of Taylor cone, cone jet, and droplet formation.

The high density of cations congregated at the meniscus and their attraction to the counterelectrode will overcome the liquid's surface tension and will cause a distortion in the meniscus which will elongate into a cone pointing downfield (*i.e.*, the Taylor cone[48]) in the direction of the counterelectrode. A fine jet of droplets will emerge from the tip of the Taylor cone (producing a so-called "cone jet"). Droplets created are enriched at the surface by excess of positive ions.

The radius of droplets ($R_d$; see Figure 1.1 bottom) emitted from the Taylor cone[45,49] is dependent on the jet diameter, $2R_j$ (twice the radius of the jet), and is approximately monodisperse[50]: $R_d/R_j \approx 1.9$. The size of droplets emitted is typically on the order of micrometers (μm). Droplets travel downfield through the ambient air to the counterelectrode while undergoing numerous desolvation processes (see Section 1.2.4). Typically, an inert nebulizing gas (*e.g.*, nitrogen) is heated and emitted from a capillary placed concentrically to the liquid capillary (see Figure 1.1). A heated, inert gas flow perpendicular to the spray direction may also be placed in the source to assist desolvation (a so-called desolvation gas). These source features increase the sensitivity of an instrument since a MS may only detect bare ions- not charged droplets. Droplets may also be prevented from entering the inlet to the MS by orientating the electrospray at an angle relative to the inlet. Smaller droplets and bare ions are more likely to exist in the periphery of the electrospray (see Section 1.2.4 and 1.2.5). Orientating the spray at an angle relative to the inet orifice of the MS will increase sensitivity and prevent contamination from liquid and neutral molecules.[1]

Vertes[51] provides details on the evolution of the Taylor cone into a cone jet and pulsations of the jet using fast time-lapse imaging. Jet pulsations lead to spray current oscillations, easily measured with an oscilloscope. Droplet diameter and velocity measurements were taken with a phase Doppler anemometer (PDA). At emitter potentials of 2750, 2950, and 4050 V, they identified three different modes of spray: axial I, II, and III, respectively. In axial I (2750 - 2950 V), fast imaging revealed an unstable meniscus forms and initially produces a trimodal droplet diameter distribution: components centered on 10.4 ± 2.2 μm, 17.9 ± 1.8 μm, and 35.7 ±1.2 μm with size distribution widths of 5.4, 4.2, and 2.8 μm, respectively. Droplet velocities ranged from 0.5 – 6.0 m/s. The $R_d/R_j$ for two trials[51] displayed in Axial I are 1.74 ± 0.18 μm and 1.81 ± 0.15 μm, values lower than the previous theoretical and experimental results discussed below.

Increasing voltage to a slightly higher value than that of axial II (3100 V) reduced the modality to a monodisperse distribution with a diameter distribution of 9.1 ± 1.8 μm with a size width distribution of 3.4 μm and droplet velocity distribution of 0.5 – 3 m/s. $R_d/R_j$ = 1.72 ± 0.32 μm . Increasing voltage even higher (3400 V) resulted in the reappearance of a bimodal droplet size distribution, which may be due to the end of the jet breaking into two separate jets.[51] One jet resulted in droplets of diameter 5 ± 1 μm; the second resulted in 31 ± 2 μm. This might be an indication of excessive charge present on and carried away from the jet filament.[49,51]

When voltage was increased to Axial III (4050 V), the Taylor cone and jet became stable and produced monodisperse droplets of diameter < 3 μm.[51] Droplets

that reached the probe volume of the PDA were undetectable (cutoff ~ 1 μm due to the limit of diffraction) and did not yield a usable signal.

Ion yields were collected by a mass spectrometer and peaked in Axial III (the so-called cone-jet mode), consistent with the smaller droplet production in that mode. Ion yields were three times higher in the cone jet mode compared with modes created at lower potentials, which demonstrates the improved analytical sensitivity achievable by producing smaller droplets due to operating in the cone-jet mode.[51] Additional discussion concerning droplet size and velocities occurs in Section 1.2.4.

### 1.2.2 Electrochemistry in the ESI Capillary

The ion source is composed of two electrodes: the (usually stainless steel) metal ES capillary (in positive mode, the anode; working electrode) and the atmospheric pressure sampling aperture plate of the mass spectrometer (the cathode in positive mode; counterelectode). These are connected together via a high voltage power supply up to approximately ± 6 kV. In the positive ion mode, oxidation reactions occur at the liquid-metal interface of the capillary, *e.g.*, $M(s) \longrightarrow M^{n+}_{(aq)} + ne^-$. In the negative mode, reduction predominates at the capillary.

Under typical ESI operating conditions, the analyte of interest (normally ionic), is pumped through the ES capillary, held at a high voltage, and sprayed towards the aperture plate. While under the influence of the applied electrical field, ions of the same polarity as the voltage applied to the ESI capillary migrate from the

bulk liquid toward capillary tip. A buildup of excess charge occurs at the tip to a critical point where Coulombic forces are sufficient to overcome the liquid's surface tension.[48] Droplets enriched in a certain polarity (depending on the electrical bias) are emitted (by a Taylor cone, see Section 1.2.3) from the capillary and travel towards the counterelectrode, creating a continuous steady-state current at the counterelectrode.[52,53] The addition of any ionic species tends to suppress the formation of gas phase ions from analytes of interest.[50,54,55,56] Exceptions include ES-friendly acids, bases, or buffers to assist in analyte ionization; formic acid, acetic acid, ammonium acetate and ammonium hydroxide are common.

For continuous production of an excess of positive ions in the charged droplets to be maintained, anions in solution must be neutralized or positive ions must be created. Kebarle's group[57] chose to demonstrate the electrochemical nature of the ES by allowing the metal comprising the ES capillary to oxidize in the hope that the metal ions produced would be observed in the ES mass spectrum. This was accomplished by selecting zinc as the metal comprising the ES capillary. The zinc capillary, which is extremely easy to oxidize ($E^0$ = -0.76 vs. SHE), released $Zn^{2+}$ ions to the solution via oxidation, which were observed in mass spectra. Van Berkel observed[58,59] molecular radical cations of easily oxidized species from bulk solution, such as aromatic amines, in the mass spectra under certain conditions. This suggested that compounds in the solution can also be involved in oxidation reactions inside the capillary.

The interfacial potential at the working potential ultimately determines what electrochemical reactions occur in the system as well as the rates at which they occur. This potential is affected by two factors. First, the effective length (i.e., the length of capillary where electrochemical reactions take place) and the applied current determine the current intensity inside the capillary. The effective length is usually far less than the physical length due to the limited electric field, which can penetrate through to the liquid inside the capillary. This was estimated to be ~1 cm by Van Berkel.[60] Cole[61] obtained spatial measurements of current using a grounded ESI capillary. The second parameter affecting the interfacial potential is the composition of the capillary. Interfacial potential varies with different materials unless the current density inside the capillary is high enough where solvent oxidation/reduction mainly supplies the majority of the current.[62]

Van Berkel[63] undertook computational simulations to estimate the interfacial potential inside the capillary. Cole[61,64] have measured it by floating the capillary system. Computation and experimental methods both determined that the interfacial potential had the highest value at the tip of the capillary (≤ 2.5 V vs. SHE) and decreased rapidly towards the inside of the capillary. Thus, the majority of electrochemical reactions occur at the tip.

Oxidation of water may take place in the capillary ($2H_2O = O_2 + 4H^+ + 4e^-$). This oxidation forms protons, which can decrease the pH of the solution when compared with the pH of the original, bulk solution. A pH decrease of 4 units was observed optically by Van Berkel using a diode array detector[65]- a dramatic change

of pH that could alter the ion intensity of weakly basic analytes or the molecular conformation of proteins. Konermann induced this effect[66] while spraying a solution containing cytochrome C and observed higher charge state distributions for the protein when the emitter was grounded. This is believed to denature cytochrome C as a result of a pH decrease.

Metal cations produced by oxidation of the metal capillary could potentially influence mass spectra by causing extra background signals. For example, Ijames reported[67] observation of peaks at m/z 538 and 662 which corresponded to $Fe_3O(O_2CR)_6(L)_{0\text{-}3}$, where ($O_2CR$) was the acid additive in the solution and L is the ligand (*i.e.*, the solvent). The iron cation was generated by oxidation of the stainless steel emitter. This effect may be reduced by reducing capillary current or replacing the stainless steel emitter with a platinum emitter. If the current density is too high, however, reactive species such as $H_2O_2$ (via $2OH^- = H_2O_2 + 2e^-$), may form and react with other solution components to produce unanticipated adducts.

### 1.2.3 Formation of the Taylor cone

The critical strength of the electric field ($E_{c,crit}$) needed to lead to the onset of the meniscus' instability is approximated by the following equation[68]:

$$E_{c,crit} \approx \left(\frac{2 \cdot \gamma \cdot cos\theta}{r_c \cdot \varepsilon_0}\right)^{\frac{1}{2}} \quad \text{(Equation 1.2)}$$

where γ is the solvent surface tension, $\theta$ is the half-angle of the Taylor cone, $r_c$ is the radius of the capillary, and $\varepsilon_0$ is the permittivity of vacuum. Equation 1.2 may be

combined with Equation 1.1 to approximate the required voltage ($V_{c,crit}$) for the onset of an electrospray:

$$V_{c,crit} \approx \ln\left(\frac{4 \cdot d}{r_c}\right) \cdot \left(\frac{r_c \cdot \gamma \cdot cos\theta}{2 \cdot \varepsilon_0}\right)^{\frac{1}{2}} \text{ (Equation 1.3)}$$

Operation at a few hundred volts higher than $V_{c,crit}$ is recommended for stable spray operation.[60] Thus, the solvents with higher surface tension values will require higher voltages to create an ES. Higher volatility solvents (i.e., possessing lower surface tension) are preferable due to the lower voltage required and their higher evaporation rate (*e.g.*, methanol or methanol/water over pure water). Increasing the electrical conductivity with an additive such as HCl was found to increase ion signal, thus overcoming at least some effects of higher surface tension.[69]

Formation of a stable Taylor cone is essential for producing a stable ion signal. A cone-jet,[49,70,71,72] believed to be the most stable form of electrospray, is typically achieved by applying a high capillary voltage (~2 – 4 kV).

### 1.2.4 Droplet Fission Processes

During a droplet's flight time, evaporation occurs naturally (and is also aided by a nebulizing and/or desolvating gas), which desolvates the droplet due to the thermal energy in the ambient air; the droplet experiences a volume decrease, as a result. Charge density increases as charge remains constant inside the shrinking droplet and intradroplet repulsion overcomes the cohesive force of surface tension.[43] This repulsion causes the droplet to subdivide, releasing a jet of small, charged, relatively monodisperse progeny droplets.[73,74,75,76,77] The charge necessary

for this event (Rayleigh limit; $Q_R$), called a Coulombic explosion, is given by the Rayleigh equation[78]:

$$Q_R = 8 \cdot \pi \cdot (\varepsilon_s \cdot \gamma \cdot R^3)^{\frac{1}{2}} \qquad \text{(Equation 1.4)}$$

where $\varepsilon_s$ is the permittivity of the solvent and $R$ is the radius of the droplet. At a critical percentage of $Q_R$, a Coulombic explosion occurs, expelling small droplets (so-called progeny droplets) from the parent droplet. This event results in a small volume decrease to the parent droplet but results in a large decrease in charge[50] (*vide infra*). Progeny droplets created by these fission events are believed to be directly responsible for the production of gas-phase ions.[50,79] The transition between these small, highly charged progeny droplets and gas-phase ions may be explained by two mechanisms: the charged residue model[19] (CRM) and the ion evaporation model (IEM)[46,80] (Figure 1.2). The nature of the analyte and solvent influence which mode of desorption dominates, as described below.

In the IEM, Iribarne and Thomson[46,80] predict that, after radii decrease to a certain size (radii ≤ 10nm), ions will be emitted directly from highly charged, small droplets. The rate ($k_1$) at which ion emission occurs is given by:

$$k_1 = \frac{k_B \cdot T}{h} e^{\left(-\frac{\Delta G^{\ddagger}}{k \cdot T}\right)} \qquad \text{(Equation 1.5)}$$

where $k_B$ is Boltzmann's constant, $T$ is droplet temperature, $h$ is Planck's constant, and $\Delta G^{\ddagger}$ is the free energy of activation. Highly surface active compounds have a greater chance to form gas-phase ions due to their predilection to congregate at the droplet's surface.

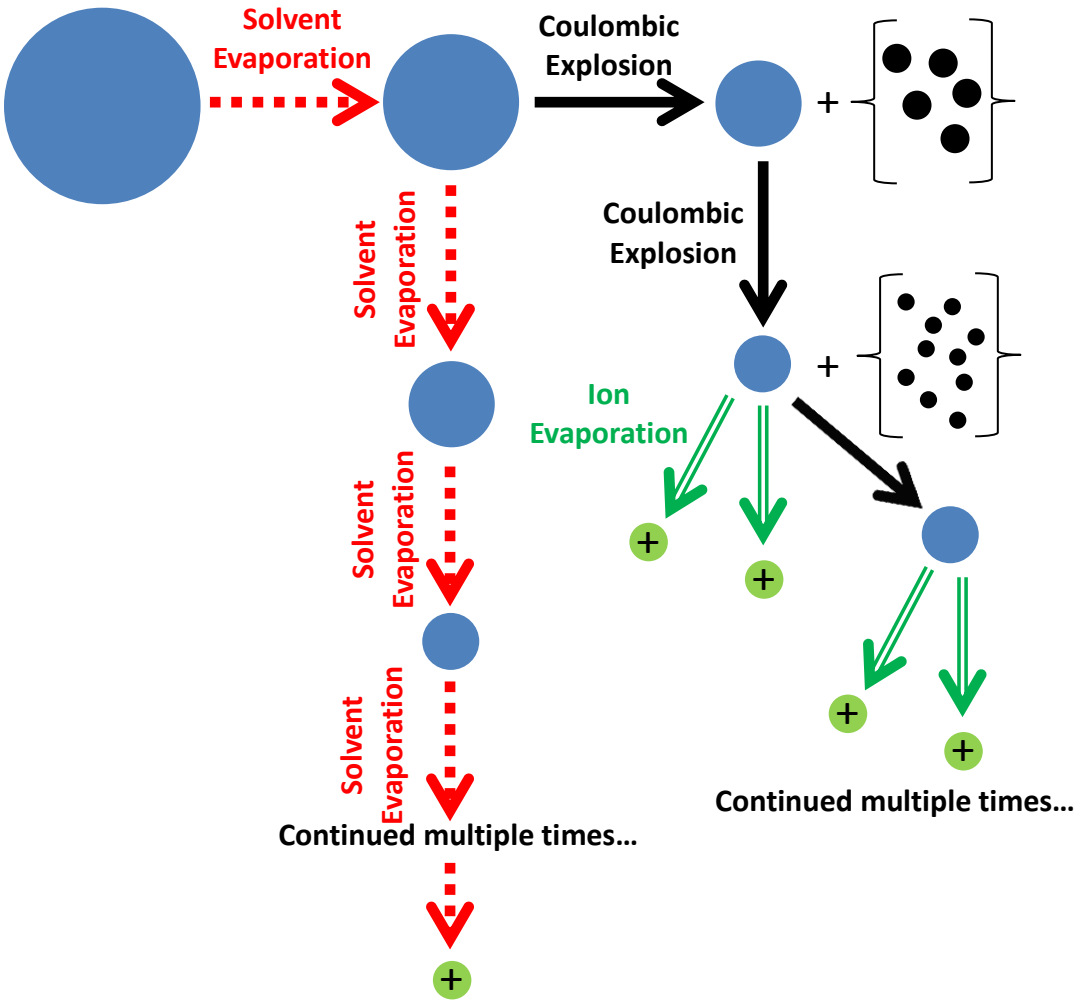


**Figure 1.2:** Diagram of ion desorption processes in ESI. Red/dashed arrows represent solvent evaporation, black/solid arrows represent Coulombic explosions, and dark green/hollow arrows represent ion evaporation. Light green circles containing a + sign represent solventless, gas-phase ions.

Kebarle and Tang[50] used the surface-controlled[81] evaporation model (see Section 1.2.6 and 3.2.4) to calculate evaporative loss as well as to investigate the validity of Iribarne and Thomson's ion evaporation model.

In order to assess Iribarne and Thomson's IEM model, Kebarle chose to begin with a droplet of "typical values": a radius of 1.5 μm and a droplet charge of 8 fC (~40% of the charge limit; Equation 1.4). These initial droplets are too large and too dilute for ion evaporation, and thus droplets shrink due to solvent evaporation while $Q$ remains constant. Fission occurs when the radius shrinks to a value where the charge in the droplet ($Q$) reaches $0.8Q_R$ for water[76,77] and methanol[50,74] (see Equation 1.4). At this point, the residue droplet undergoes a Coulombic explosion and loses 15% of its charge and 2% of its mass.[50] This process repeats itself with a succession of droplet emissions occurring from the gradually shrinking droplet. The rate of mass loss due to ion evaporation is negligible compared with the losses associated with Coulombic explosions.[50] When Iribarne's ion-emission radius is achieved, the droplet loses approximately half its charge in ~1 μs- a rate significantly slower than that due to Coulombic explosions.[50]

Several groups have provided arguments for and against the IEM. Fenn[82,83] provided some evidence for the IEM by measuring the effect of increasing the local vapor pressure of solvents on the evaporation process. Samples (amino acids and peptides) were delivered with a nebulizing gas doped with solvent vapor. Normally, this increase in ambient solvent vapor pressure would inhibit solvent evaporation, resulting in lower signal intensity. However, the addition of the solvent to the

nebulizing gas increased analyte signal. Fenn concluded this process would inhibit an evaporation-based ion formation model (see below- charge residue model) and that IEM should be the gas-phase mechanism. The Vertes group[84] simulated evaporation processes of $H_3O^+$ from nano-sized water droplets. Droplets exhibited shape and surface deformations, which serve as steps preceding ion ejection. Ions were then ejected from a droplet with a solvation shell of approximately 10 solvent molecules per ion. This data was consistent with the solvated ion evaporation model for droplets close to the Rayleigh limit.[80,84] Fernandez de la Mora[79] provided evidence for the IEM by studying the size and charge of solid residues formed after evaporation of the solvent. They presumed that since solid residues had existed as charged droplets moments before, their sizes and charges represent a reasonable approximation of the sizes and charges of evolving charged droplets. By employing low flow rates and a highly conductive solution, they were able to create very small initial droplets which would reach the Iribarne ion emission radius before experiencing Coulombic fission. By assuming the density of the residue droplets was the same as that of the solid salt, radii were determined using a hypersonic impactor. In combination with mobility measurements, charge was deduced. The charges determined were considerably lower than $Q_R$, Equation 1.4. Thus, Fernandez de la Mora concluded ion evaporation had to occur before the Coulombic explosion. Additional studies[85,86] reinforced the assumption that the residue density is the same as the solid salt density.

The IEM was questioned by Röllgen[87] arguing that the Coulombic fissions require a field strength lower than that required for ion evaporation. However, due to the difficulty of observing droplets smaller than the diffraction limit, it is difficult to clearly distinguish Coulombic explosions and ion evaporations in later stages of the ES process.

The CRM[19] suggested Coulombic explosions will occur continuously and will lead to the production of very small droplets containing a sole analyte ion and several solvent molecules. Soon after, the remaining solvent molecules evaporate, leaving a bare gas-phase ion. Smith[88] provided evidence for the CRM for the ion formation of larger molecules such as proteins. They hypothesized that when small charged droplets evaporate, there is not only one protein, but possibly multiple proteins in each droplet. By contrast, ion-evaporation is difficult for more than one protein at a time due to the high energy barrier of larger molecules. Therefore, the observation of not only monomers but higher level multimers should be expected. Higher order multimers were observed. Thus, they concluded the CRM dominates for larger molecules.

Fernandez de la Mora[89] asserted that when all the solvent had evaporated from a droplet, all solvent charges would necessarily transfer to the protein. Analysis of previous dendrimer data collected in a study by Smith[90] displayed this relationship and provided evidence for the CRM. Thus, more volatile solvents that possess less surface tension should lead to proteins with $m/z$ values located at lower charge states. Iavarone and Williams[91] also showed that the average charge

state of the DAB 64 dendrimer in 2-propanol was lower than the same dendrimer in water.

Based on the large body of literature, the IEM seems to dominate for smaller analytes, while larger ions form by the CRM.

### 1.2.5 Droplet Size and Velocity

The initial radius ($R_0$) and charge ($Q$) of droplets generated at the moment of detachment from the Taylor cone can be estimated by the following empirical equations[92]:

$$R_0 \approx \left(\frac{V_f \cdot \varepsilon}{K}\right)^{\frac{1}{3}} \quad \text{(Equation 1.6)}$$

$$Q \approx 0.7\left[8 \cdot \pi(\varepsilon \cdot \gamma \cdot R^3)^{\frac{1}{2}}\right] \quad \text{(Equation 1.7)}$$

where $V_f$ is the flow rate, $\varepsilon$ is the permittivity of the solvent, $K$ is the conductivity of the solvent, $\gamma$ is the surface tension of the solvent, and $R$ is the radius of droplets produced at the capillary tip. The initial radius, as well as velocity, may be measured *in situ* by phase Doppler interferometry. In addition, electrode configuration (electrode size, shape, and distance) and voltage differential between electrodes impact droplet size and velocity, as seen in the variety of studies compiled in Table 1.1 and discussed below.

In two studies by Gomez and Tang,[45,76] size distributions were observed to be very monodisperse at every axial distance interrogated in the plume. In their first study[76], heptane was sprayed from a stainless steel capillary (inner diameter = 0.12 mm; outer diameter 0.45 mm) with an electrode ~3 cm away.

**Table 1.1:** Reported distributions of droplet size for various solvents.

| Solvent | Droplet Diameter Range | Reference |
|---|---|---|
| Acetonitrile | 10-40 | 93 |
| Ethylene glycol | 20-30 | 94 |
| Heptane | 2-100 | 45,76 |
| *n*-Heptane | 35-45 | 73 |
| Low-vapor pressure oils | 4-20 | 77 |
| Methanol | 10-40 | 93 |
| Methanol/Water | 1.5-7 | 95 |
| Methanol/Water | 1-3 | 96 |
| n-Octanol | 15-40 | 97 |
| Water w/ surfactant | 10-40 | 75 |

Heptane droplets were measured to have decreasing diameters of ~37, 35, 32, and 31 μm at increasing distances from the spray emitter of 7.6, 25.8, 33.6, and 43.6 mm, respectively. The size distribution widened as distance increased, eventually becoming bimodal at 33.6 mm downspray with the primary distribution centered at 32 μm and the secondary centered at 2 – 3 μm. The abundance of droplets with radius 2 – 3 increased by two orders of magnitude by the time droplets reached a distance of 43.6 mm from the emitter. These 2 – 3 μm droplets were confirmed to be offspring droplets by PDA correlation between velocity and diameter. Since larger droplets possess greater inertia, they decelerate at a slower rate in comparison with smaller droplets. At 43.6 mm, droplets larger than 4 μm were observed to possess little to no radial acceleration vectors (*i.e.*, vectors not parallel to the direction of the majority of droplets emitted). Droplets at size 2 – 3 μm possessed both positive and negative velocity values. Since PDA may only measure the velocity of droplets with a vector in a single direction, the evidence of lost momentum of these smaller droplets indicates a radial component to their velocity. Droplets possessing a radial velocity component indicates they were not traveling at velocities governed by emission from the electrospray tip, but were governed by fission phenomena.[76]

In a second study,[45] Gomez and Tang found at a distance of 4.14 mm away from the emitter, heptane droplets displayed a diameter of 32.3 μm with a narrow size distribution with a velocity of 12 m/s. Farther downspray, droplets are smaller, with diameters of ~18 and ~10 μm at ~5.5 and 7.0 mm, respectively. These

measurements were taken on the axis of the spray and do not reflect the periphery of the spray, which tends to contain smaller droplets which have migrated rapidly away from the axis due to space charge effects and inertial separation.[51,95] Velocity was approximately constant at ~12 m/s in the first 3 – 4 mm from the emitter and decreases to 6 m/s at a distance of 25 mm due to a competition between electrostatic and drag forces.[45] In order to determine the drag on the droplet, the nebulizing gas was doped with $Al_2O_3$ molecules, allowing a comparison between the droplet flow rate and that of the gas velocity. The velocity of the $Al_2O_3$ molecules was assumed to be representative of gas velocity and ranged from 4.2 to 0.85 m/s toward the end of the probed region, which is non-negligible in the analysis of droplet motion. Velocities measured radially away from the spray axis monotonically decrease as a function of radial coordinate. For instance, on-axis at 5.5 mm away from the emitter, the velocity of droplets decreases from ~12 m/s on the spray axis to ~ 9 m/s at a radial distance of ~2.5 mm. At larger axial distances such as 20 mm, droplet velocity decreases from 6.5 m/s on-axis to ~4 m/s at a radial distance of 5.5 mm. This decrease is directly attributable to two effects. First, droplet motion is primarily driven by the electrostatic field which should be most intense along the spray centerline. Second, smaller droplets will possess some portion of their velocity vector not perpendicular to the axial spray. The PDA in this setup was configured to only measure the axial component of velocity. Thus, some velocity information was lost.

Vertes[95] also use a PDA system to analyze the effect on a salt dopant on droplet size and velocity. Methanol/water (90:10) solutions with and without KCl were sprayed from a stainless steel capillary (inner diameter = 150 μm; outer diameter = 510 μm) at 24 μL/min under 3.0 – 4.8 kV. The addition of the salt resulted in much smaller average droplet diameters: from 6.9 to 1.5 μm, 4.8 to 1.9 μm, and 4.7 to 3.9 μm at axial distances of 4, 10, and 22 mm, respectively (see below for possible causes of droplet size increases for highly conductive solutions). The addition of a salt also resulted in a significantly narrower droplet size distribution at small distances from the emitter due to the increase in conductivity. Salt dopant concentrations over four decades were analyzed and resulted in differing trends between low-conductivity and high-conductivity solutions. In solutions with lower concentrations of KCl (none, 5.0 μM and 50 μM), a decrease in droplet size was seen at increased measurement distance from the capillary. However, for high conductivity (0.5 mM and 5 mM), droplets were seen to *increase* in size (1.5 to 3.9 μm) as distance from the emitter increased. The authors suggest two possible reasons for this droplet size increase. First, as the spray diverges along its axis, smaller droplets are electrostatically segregated to the periphery of the spray; larger residue droplets remain on-axis. This leads to an enrichment of larger droplets on-axis downstream, compared to a relatively broad size distribution on axis upstream. This effect may be increased due to increasing the conductivity, thereby enhancing space charge repulsion. Second, the growing droplet size might occur due to increased coalescence at higher conductivities (*i.e.* higher ionic

strengths). Given the substantial amount of charges associated with the droplets, their collision and coalescence are considered unlikely even at large particle densities. However, when two droplets of similar charge approach each other, they undergo deformation and charge rearrangement. As the droplets approach each other, their shape will elongate and excess charges will move to opposite ends of the elongated sphere. This will modify the original Coulomb potential into a shielded Coulomb potential with a shielding length inversely proportional to the square root of the ionic strength.[95] At a sufficiently high conductivity, repulsion between two approaching droplets may be eliminated, causing droplets to coalesce.

In the same study,[95] velocity distributions as a function of distance from the emitter decreased from 34.5 to 9.6 m/s at distances of 4.0 to 22 mm, respectively. Velocity distributions also narrowed as distance from the emitter increased. These data indicate homogenization of droplets, which has beneficial implications for ESI sampling efficiency. Additionally, solutions containing the KCl dopant were found to be slower (4 m/s) than pure solvent (37 m/s) at the same axial position. The authors suggest this effect is due to morphological changes of the cone-jet structure and differences in field penetration due to shielding.[95]

In a second study, Vertes[51] analyzed the effect of the spray mode on droplet formation (previously discussed in Section 1.2.1). Droplet size distributions again narrow as voltage increases: from diameters of 10 ± 5 μm to 7 ± 1.5 μm between 2500 to 3400 V, respectively. Velocity distributions tighten up as well, from a wide 1 to 6 m/s distribution at 2500 V to <1 to 1.5 m/s at 3400 V. Vertes suggests[51] the

average size and velocity of droplets in the most favorable conditions are 11 μm and 2 m/s, respectively.

In general, it is advantageous to produce small initial droplets to maximize the chance that bare, gaseous ions are formed before reaching the inlet to the mass spectrometer. It is advantageous to use volatile solvents with larger applied electric fields (limited by corona discharges[98]). Generally, if the source is spraying in a favorable mode, droplets are typically monodisperse. High conductivity, through the use of low concentrations of salt dopants, is also advantageous for reliable operation. Smaller droplets and bare gas-phase ions are more likely to exist in the periphery of the electrospray plume. These findings support use of electrospray sources whose axis is not pointed directly at the MS orifice, but at an angle in order to capture a higher amount of desolvated ions and to reduce contamination introduced by solvated droplets.

### 1.2.6 Ramifications of Solvent Evaporation and Droplet Shrinkage

Due to solvent evaporation, droplet volume decreases. As a consequence, concentration increases. This has the potential to induce chemical changes such as changes in pH, solvent composition, analyte concentration, and charge state. In many cases, the distribution of gas-phase ions observed in ES-MS is dramatically different than that known to exist in solution prior to spraying.[99,100,101,102,103,104,105,106,107,108] Probing these inherent ES processes can provide useful insights into the ionization and sampling mechanism.

The effect of solvent evaporation on droplet pH was interrogated using laser-induced fluorescence spectroscopy by Cook.[109,110] By directly probing the ES plume, whose droplets contained the pH indicator carboxyseminaphthorhodafluor-1 (C.SNARF-1), they were able to assess and spatially profile plume pH. In the positive-ion mode, droplets emitted from the Taylor cone are positively charged, and thus are enriched with $H^+$. Due to evaporative losses, the volume of droplets will decrease, which will in turn increase $[H^+]$ and decrease pH. The pH of the unbuffered bulk solution, measured by a pH meter, was 6.89 ± 0.05 and 7.00 ± 0.05 for the positive and negative mode, respectively. As expected, in the positive-ion mode, a pH decrease of 0.24 to 0.90 pH units as a function of increasing emitter voltage was detected. The negative-ion mode displayed correspondingly similar results with a maximum initial pH increase of between 0.10 - 0.56 units as voltage increased. In a subsequent study,[109] laser power was increased in order to probe longer distances from the emitter. When the spray was interrogated at 8 mm downspray in the positive mode using a solution with an initial bulk solution pH = 6.90 ± 0.05, pH dropped 1.23 units. Since the droplets were interrogated at a longer distance from the emitter, the larger pH decrease is consistent. However, in the negative mode, after an initial increase in measured pH of ~ 0.43 units at 1 mm away from the spray tip, pH values begin to decrease, contrary to intuition. The authors ascribe the estimated ~7 fold increase in proton concentration to how the dye partitions in the droplet. Dye may congregate at or near the surface, which would enrich offspring droplets in dye. This partitioning would aid in depleting the

residue droplet's dye concentration more quickly than if the offspring droplets were comprised of a more representative dye concentration.

Solvent fractionation was analyzed[111] via a similar laser-induced fluorescence method. Nile red, a solvochromatic dye, was used in various combinations of acetone, acetonitrile, ethylene glycol, and water. For acetone/water mixtures, the wavelength of maximum emission red shifted as the distance from the emitter increased, which indicated depletion of acetone- the component possessing a lower boiling point and less polarity, according to polarity calibration curves. Over the first 8 mm of the spray, acetone depleted approximately 35% in both positive- and negative-ion modes. Solvent combinations with large disparities in vapor pressure displayed the largest fractionation since the droplet becomes enriched in the less volatile solvent, in agreement with previous studies.[112] At higher voltages, smaller droplets are generated (see previous section), which resulted in higher degrees of fractionation since smaller droplets evaporate more quickly (see Sections 1.2.7 and 3.2.4 for more in-depth discussion of droplet evaporation processes).

The addition of a nebulizing gas reduced fractionation, though it did not entirely prevent the effect. The nebulizing gas was believed to reduce fractionation by playing the dominant role in determining droplet size, as opposed to the applied field (which was presumed to only affect droplet velocity and transit time). By adding 0.1% formic acid to the bulk solution, the droplet evaporation rate was

enhanced due to the production of smaller initial droplets (due to increase in solution conductivity; see Section 1.2.2) and, therefore, fractionation increased.

An increase in the sample flow rate is generally accompanied less than a proportional increase in emission current.[111] A reduction in charge density results, thus generating larger droplets.[79] Large droplets possess a slower rate of evaporation relative to their volume when compared to smaller droplets. Thus, the slower rate of evaporation should impede solvent fractionation. More fractionation was evident at the edges of the plume due to the propensity for smaller droplets to migrate away from the dense plume center.

Zenobi and Wang[113] followed up Cook's solvent fractionation study by investigating whether changes in solvent polarity are the reason for variations in fluorescence emission behavior exhibited in the ES plume and to explore changes in solvent polarity. They used solvochrome dyes Nile red and 4-(Dicyanomethylele)-2-methyl-6-(4-dimethylaminostyryl-4H-pyran) (DCM), with Rhodamine 6G (R6G) as an internal standard. A single solvent, ethanol, was used instead of a solvent mixture to simplify the system. The quantum yield of Nile red decreases and red shifts as solvent polarity increases; DCM also red shifts, but the quantum yield increases. Ratios of the emission maxima for mixtures of Nile red/R6G and DCM/R6G were analyzed, which are directly related to the quantum yield.[114] When probing the plume down the axis, the emission intensity ratio of a Nile red/R6G solution decreases by up to 50% as axial distance from emitter increased, while the intensity ratio of the DCM/R6G mixture increased by 20% during that same

distance. Thus, the quantum yield of Nile red decreases in the spray direction as DCM increases, implying that solvent polarity increases significantly as the droplet diameters in the plume decrease. Radially (*i.e.*, laterally, perpendicular to the emitter axis), the two mixtures exhibit the same behavior, whereby solvent polarity was observed to increase as distance from the emitter increased. These observations imply solvent polarity increases significantly as droplet diameters decrease. These increases in polarity[113] were suggested to be influenced by solvent evaporation, water entrainment from surrounding air, and solvent volatility. The addition of electrolytes (acetic acid and sodium fluoride) was not found to affect solvent polarity, though this is contradictory to previous work.[79,95,111] Zenobi and Wang report fluorescent shifts similar in magnitude between their two chosen analytes, which is curious considering the large difference in electrical conductivity between acetic acid and sodium fluoride.

The protein cytochrome C was used to probe correlations between solvent fractionation and charge state by combining *in situ* fluorescence measurements with mass spectrometry.[96] Nile red (without a standard) was also used in this experiment to probe solvent polarity of a MeOH/water mixture and corroborated trends discussed above (downstream droplets were enriched with water due to methanol preferentially evaporating). The addition of MeOH to a cytochrome C/water mixture will induce an increase in charge state of the protein, which corresponds to the unfolding of the protein. As noted above, the droplets will be enriched with water downstream. The increase in relative water percentage will

assist in the refolding of cytochrome C. When droplet evaporation rate was increased (i.e. higher nebulizing gas rate/temperature and capillary voltage), charge state is decreased, resulting in a shift to higher *m/z* values. These results complement previous studies monitoring cytochrome C protein denaturation in the electrospray.[115,116]

In addition to the above ramifications, droplet evaporation is inherently an endothermic process. Thus, heat is removed from the residue droplet in order to produce the emitted gas-phase solvent molecules. This phenomenon is introduced in Section 1.2.7 and investigated in Chapter 3.

### 1.2.7 Evaporation-Induced Temperature Changes within a Droplet

Temperature is another parameter that can affect solute chemistry either directly (*e.g.*, affecting the conformation of biopolymers[117]) or indirectly (*e.g.*, by affecting solvent evaporation and fractionation processes). Droplet cooling is recognized to have an effect on the kinetics and equilibria of reactants in the spray.[118] Temperature is also an integral parameter governing the rate at which IEM[46,80] occurs (see Equation 1.5).

Kebarle and Tang[50] were the first to quantify the cooling of droplets in an electrospray plume. At equilibrium, heat gained from ambient gas (left side of Equation 1.8) is equal to the heat lost by evaporation (right side of Equation 1.8):

$$P_g \cdot c_p(air) \cdot \Delta T = \alpha \cdot p^o \cdot \Delta H_{vap}(MeOH) \quad \text{(Equation 1.8)}$$

where $P_g$ is the ambient gas pressure, $c_p$ is heat capacity of air, $\Delta T$ is the temperature difference between the evaporating droplet and ambient gas, $\alpha$ is the condensation coefficient, $p^o$ is solvent vapor pressure, and $\Delta H_{vap}(MeOH)$ is the enthalpy of vaporization for methanol. Kebarle and Tang rearranged Equation 1.8 to solve for $\Delta T$. The rearrangement and the values they used for the parameters are shown in Equation 1.9:

$$\Delta T = \frac{\alpha \cdot p^o \cdot \Delta H_{vap}(MeOH)}{P_g \cdot c_p} = \frac{(0.04)\cdot(120\ torr)\cdot\left(9000\ \frac{cal}{mol}\right)}{(760\ torr)\cdot\left(7\ \frac{cal}{K\cdot mol}\right)} \cong 8\ K \qquad \text{(Equation 1.9)}$$

Kebarle and Tang conclude that, for methanol, a droplet's temperature decreases to 8 K below that of the ambient gas temperature.. Kebarle and Tang assume, due to the size of the droplet chosen, that the droplet is undergoing surface-controlled evaporation (see next paragraph) and use this model to calculate changes in droplet radius due to evaporation (See Section 3.2.4). To this point, there have been no experimental or theoretical determinations of the temperature of electrospray droplets in non-equilibrium conditions.

Davies[81] describes two models for droplet evaporation, which may be used to model droplet cooling. For large droplets (definition below) which possess large surface areas, solvent vapor molecules form a saturated vapor layer around the droplet (see Figure 1.3- top). Vapor molecules will escape from this layer (though recondensation may occur), allowing more vapor molecules to exist in the saturated layer, shrinking the droplet. This evaporation model (so-called diffusion-controlled evaporation) continues until the droplet reaches a solvent-specific critical radius, $r_c$.

Below this radius, so-called surface-controlled evaporation occurs. The surface area of droplets in this model is lower and thus is not able to populate a saturated vapor layer. Thus, the rate of evaporation is controlled by the rate of solvent escape from the droplet surface (Figure 1.3 - bottom). These models are explained in considerably more depth in Section 3.2.4.

### 1.2.8 Method for Analysis of Droplet Temperature

Temperature can be measured using fluorophores with temperature-dependent emission wavelengths and/or intensities. For ES measurements, there is some advantage to relying on temperature-dependent changes in emission wavelengths[119,120,121] because intensity changes also reflect changes in concentration as droplets evaporate and disperse. However, temperature-induced shifts in emission wavelengths are usually small. For example, Rhodamine B (RhB; molecular structure presented in Appendix Figure A-1) displays only a 1.5 nm red shift in the emission maximum when heated from 283 K to 319 K. In contrast, the emission intensity of RhB decreases by 2.3% per degree in the same temperature range.[122] This temperature sensitivity can best be exploited by using a temperature-insensitive internal standard and a ratiometric, two-color LIF thermometry approach.[123] Rhodamine 110 (Rh110; molecular structure presented in Appendix Figure A-2) is relatively temperature insensitive (0.13% per K).[123,124]

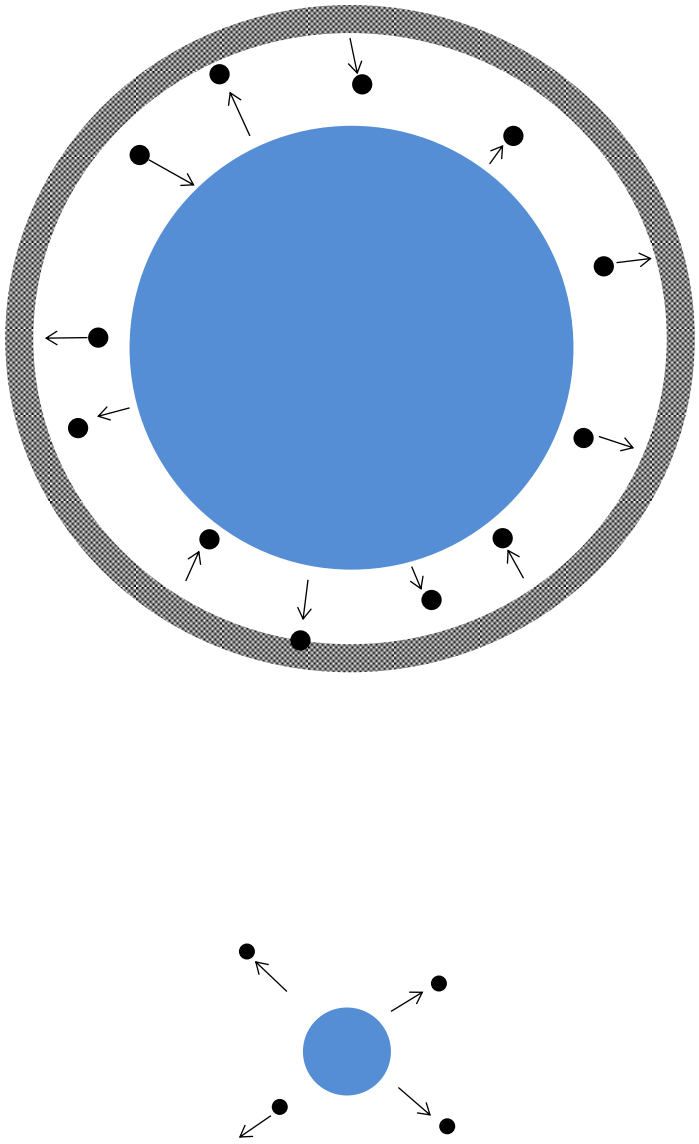

**Figure 1.3:** Visual representation of a droplet undergoing diffusion-controlled evaporation (top) and surface-controlled evaporation (bottom).

It has been employed as a standard in the analysis of solution thermal gradients[123] and in spatially-resolved temperature measurements at the micrometer scale.[125]

## 1.3 Fundamentals of Direct Analysis in Real Time

A direct analysis in real time (DART) source is comprised of two main components.[1] First, an enclosed ionization source excites and heats an inert gas, typically helium. The gas exits the source into the reaction zone, where the excited (metastable) inert gas induces a Penning ionization reaction with ambient water vapor. Typical DART analysis requires the analyte be absorbed onto any surface, typically without the need for pretreatment, which allows this source to be extremely versatile.

### 1.3.1 Source Design

An inert source gas, typically helium (He) or nitrogen, is guided through an axially segmented tube[18,126] (see Figure 1.4). First, a direct-current (DC) corona discharge[126] is initiated by applying a kilovolt potential between a needle electrode and a grounded counter electrode and reacts with the source gas to produce[18] electrons, ions, and metastable species. This ~328 K discharge[126] operates at currents on the order of 2 mA. The electrons, ions, and metastable species pass through the perforated ground electrode. Electrode 1 filters out electrons and ions, leaving metastable species to pass through a heated gas zone, which is typically heated to 573 K.

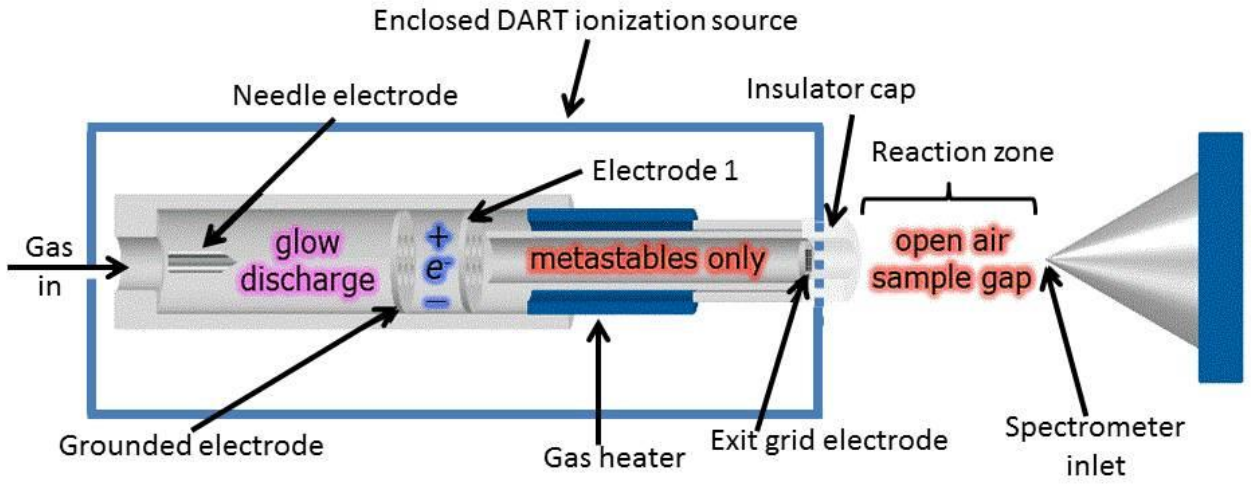


**Figure 1.4:** Schematic of the DART ion source. Adapted and used with permission from Dr. Robert Cody (JEOL).

Gas will then enter the grid electrode which acts as an ion repeller, perhaps to propel reagent ions and analyte ions towards the MS orifice,[127] and also serves to remove ions of the opposite polarity, thereby preventing signal loss by ion-ion recombination.[18] The insulator cap serves to protect the user and sample from high voltage discharges.

Metastable gas ($He^*$) emitted from the source unit immediately ionizes the ambient, surrounding gas in the laboratory. The sample is introduced in the open air sample gap: an area approximately 5 – 25 mm downstream of the DART source and before the orifice of the mass spectrometer. Although the primary ionization species is the metastable gas, the ionization of analyte molecules mostly occurs via secondary ions created from the surrounding air.[18]

Samples are subjected to gas-phase ionization processes closely related to those in APCI[16,126] and APPI. [27,128,129] Since gas-phase reactions are occurring, a gas-phase analyte is a prerequisite, which is affected by evaporation or thermal desorption.[130] Even compounds with very low vapor pressure[131], such as low-mass polymers or fullerene, may be analyzed by DART. Consequently, the upper mass limit is defined by the ability for the analyte to evaporate from the sample surface since thermal desorption alone may not be sufficient to vaporize larger molecules.[18]

### 1.3.2 DART Ionization Mechanism

DART may generate positive or negative ions , depending on the polarity of the electrode 1 and the grid electrode.[18,128] Polar analytes usually form molecular ion

adducts with protons $[M + H]^+$, oxygen and hydrogen $[M + O + H]^+$, or ammonium $[M + NH_4]^+$ in the positive mode and lose hydrogen $[M - H]^-$, lose hydroxide $[M – OH]^-$, gain chloride $[M + Cl]^-$, or lose cyanide $[M - CN]^-$ in the negative mode.[127] Other adducts are possible when additional dopants are present.[18] Non-polar molecules typically produce[127] positive-ion adducts with hydrogen $[M + H]^+$ and oxygen and hydrogen $[M + O + H]^+$ in addition to creating molecular ions, $M^{+\bullet}$ ($^\bullet$ = radical ion). Negative-ion mode adducts similarly include $M^{-\bullet}$, a loss of hydrogen $[M - H]^-$, a loss of hydrogen and a net gain of molecular oxygen $[M – H + O_2]^-$, a gain of a molecular oxygen radical anion $[M + O_2]^{-\bullet}$, or a gain of a chloride $[M + Cl]^-$. These formations are strongly dependent on analyte properties such as gas-phase acidity or basicity, ionization energy (IE), or electron affinity (EA).

As stated above, the three primary gas sources used in DART are helium (He), argon, and nitrogen. Currently, He is the most studied[18,128,132] and used source gas in order to provide more selective and softer ionization due to its high metastable energy of 19.8 eV, which is much greater than the ionization energy of any potential relevant analyte molecule.[18,126,128,133,134] Argon possesses lower energy metastable states (11.55 and 11.72 eV), which results in poor sensitivity in ambient air mainly because it cannot ionize water (IE = 12.65 eV). However, studies investigating nitrogen as a source gas are underway.[135] Electronically excited noble gas atoms are not a recent development. In the 1920s, Penning proved[136] that noble gas atoms can be effectively energized in electrical corona or glow discharges to enter an electronically excited state below the ionization energy of the gas:

$$\text{(noble gas)} + \text{energy} \longrightarrow \text{(noble gas)}^* \qquad \text{(Equation 1.10)}$$

After exiting the source into the atmosphere, (noble gas)* can interact with anything present in the atmosphere – typically water, nitrogen, and oxygen – to induce so-called Penning ionization. For example,

$$\text{(noble gas)}^* + M \longrightarrow \text{(noble gas)} + M^{+\bullet} + e^- \qquad \text{(Equation 1.11)}$$

where M is the analyte molecule (or reactive intermediate) resulting in the formation of a molecular ion $M^{+\bullet}$ plus an electron $e^-$. This reaction will occur if the analyte's ionization energy is lower than that of the excited-state reactant metastable ion. The energy stored in metastable noble gases increases in the order He* > Ne* > Ar* > Kr*.[137] This excited state primarily reacts with atmospheric water rapidly with extremely high efficiency. In typical DART source setups, He* [*i.e.* $He(2^3S)$] reacts with water to form ionized water clusters:

$$He(2^3S) + nH_2O \longrightarrow He(1^1S) + [(H_2O)_{n-1} + H]^+ + OH^{\bullet} + e^- \quad \text{(Equation 1.12)}$$

The most likely water cluster to form is $H_5O_2^+$.[128] Proton transfer to produce the protonated analyte molecule $[M + H]^+$ will occur with high efficiency[128] if the analyte molecule M has a higher proton affinity than the ionized water clusters. Thus, the following reaction occurs:

$$[(H_2O)_{n-1} + H]^+ + M \longrightarrow [M+ H]^+ + nH_2O \quad \text{(Equation 1.13)}$$

Analyte fragmentation may occur if the difference in proton affinity between the sample and water clusters is large.[128] Additionally, fragmentation or pyrolysis may be induced if the DART gas is set to a sufficiently high temperature.[138]

Direct charge transfer from the ionized molecular gases may occur,[128,130] resulting in a charge transfer mechanism:

$$N_4^{+\bullet} + M \longrightarrow 2N_2 + M^{+\bullet} \qquad \text{(Equation 1.14)}$$

$$O_2^{+\bullet} + M \longrightarrow O_2 + M^{+\bullet} \qquad \text{(Equation 1.15)}$$

$$NO^{+} + M \longrightarrow NO + M^{+\bullet} \qquad \text{(Equation 1.16)}$$

Thus, analyte ions may be formed by Penning ionization with He* or a charge transfer mechanism taking place between He*, water clusters, and the analyte ion. Analytes with lower IE will favor $M^{+\bullet}$ ion production, while high gas basicity will yield $[M+ H]^{+}$.

Ammonium adducts $[M + NH_4]^{+}$ may also be formed for polar analytes, typically peroxides[139] and carbonyl functional groups[128] such as acids, esters, ketones:

$$M + NH_4^{+} \longrightarrow [M + NH_4]^{+} \qquad \text{(Equation 1.17)}$$

Ammonium ions may be generated by sample impurities or from traces in the local atmosphere. Deliberate $[M + NH_4]^{+}$ ion production has been achieved by placing a small vial of 10-25% aqueous ammonia in the proximity of the ionization zone.[140]

In negative-mode DART, the ionization mechanism seems to be similar to APPI.[129] Metastable helium [$He(2^3S)$; Equation 1.11] reacts with ambient nitrogen gas ($N_{2\,(g)}$):

$$He(2^3S) + N_2 \longrightarrow He(1^1S) + N_2^{+\bullet} + e^{-} \qquad \text{(Equation 1.18)}$$

Atmospheric oxygen is the most likely species to undergo electron capture to form $O_2$ reagent ions ($IE_{O2}$ = 12.07 eV)[128]:

$$O_2 + e^- \longrightarrow O_2^{-\bullet} \qquad \text{(Equation 1.19)}$$

which may form an adduct with analyte M (Equation 1.20), then continue to react by dissociating to form a radical anion (Equation 1.21):

$$O_2^{-\bullet} + M \longrightarrow [M + O_2]^{-\bullet} \qquad \text{(Equation 1.20)}$$

$$[M + O_2]^{-\bullet} \longrightarrow M^{-\bullet} + O_2 \qquad \text{(Equation 1.21)}$$

Previously, all models of the DART ionization mechanism assume water cluster and/or molecular oxygen directly reacts with the analyte molecules, M, to produce analyte ions. However, this does not explain why ion suppression occurs when analytes are dissolved in select solvents. For instance, dimethyl sulfoxide was determined to be an unfavorable solvent to DART ionization.[141] A more careful study that addresses matrix effects of solvents is needed to elucidate the interaction between DART source ions, solvent matrices, and analyte ions.

## 1.4 Objectives

The motivation for the research presented in this dissertation is to explore the complex interactions that occur in and result from ambient ionization sources used in mass spectrometry. The ionization mechanisms of electrospray ionization (ESI), now considered a cornerstone ion source of the field, and Direct Analysis in Real Time (DART), a relatively new but highly utilized ion source, are investigated.

To understand the relationship between ions formed in ESI mass spectrometry and those present in bulk solution, it is necessary to consider spray-induced physical and chemical changes.[82,112,142,143,144] Changes in droplet

temperature, due to endothermic solvent evaporation, may affect this relationship if analyte kinetics are faster than the timescale of the decrease in droplet temperature. This effect is probed using a laser-induced fluorescence method (first used to probe electrospray plumes by Cook[110,109,111,145] and subsequently used by Zenobi[113] and Antoine[96]) to profile the electrospray plume for temperature changes using a fluorescence thermometry dye system. To validate experimental measurements, two evaporation models – diffusion-controlled and surface-controlled - were fit to experimental data. This provided further insight into the fundamental parameters affecting droplet temperature. This work is presented in Chapter 3 and was published[146] in *Analytical Chemistry* in 2014.

Direct Analysis in Real Time (DART) is a relatively new technique[18] that has become widely used in the the analysis of many samples in their native forms: e.g. perfumery raw materials deposited on smelling strips,[147] counterfeit Cialis tablets,[148] strobilurin fungicides in the ethyl acetate extract of wheat,[149] fatty acid methyl esters from bacterial whole cells,[150] self-assembled monolayers of dodecanethiol on gold surfaces[151], taxoids from cell cultures of *Taxus wallichiana*,[152] alkaloids from the intact hairy roots of *Atropa acuminate*,[153] and cuticular hydrocarbons from an awake-behaving fly.[154] The DART mechanism offered by Cody[18],[128] does not account for ion suppression effects created by the use of "unfavorable" DART solvents, such as dimethyl sulfoxide.[141] To explore these effects, analytes with low proton affinity were selected to assess their ion abundances in a selection of 25 different solvents that include proton acceptors,

benzene derivatives, alkanes, and chlorinated methanes. Solid analytes, which may be desorbed by the DART gas stream, were also analyzed to compare with their solvated forms. This work is presented in Chapter 4 and was published[155] in *Analytical Chemistry* in 2009.

# Chapter 2. Experimental

## 2.1 Chemicals

Chemicals, sources, and purities are listed in Table 2.1. The chemicals were used as received from the indicated manufacturers.

## 2.2 Temperature Study

### 2.2.1 Instrumentation

The method used in studies of the electrospray (ES) plume was based on laser-induced fluorescence spectroscopy (LIF). Information about the droplets was acquired through the measurement of fluorescence spectra of indicating dyes added to the solution to be sprayed. A schematic of the ES-optical spectrometer configuration used to probe the ES plume and the coordinate system employed is shown in Figure 2.1 and 2.2.

### 2.2.2 Optical System

The 488 nanometer (nm) line of a Coherent Innova (Palo Alto, CA) 200 argon ion laser was used for excitation orthogonal to the spray axis (along the X axis). The laser was set to a current of about 18 amperes (A), which resulted in a laser with power between 0.8 and 1.0 Watts (W). The laser power was attenuated to ~25 milliwatts (mW) at the spray, which was assessed with a power meter (New Focus, Santa Clara, CA; model 3803), due to three reasons: 1) losses associated with

**Table 2.1:** List of chemicals used in this work.

| Reagent | Supplier | Purity |
|---|---|---|
| 1,2,4,5-tetramethylbenzene | Aldrich Chemical | 98% |
| 1,3-dimethoxybenzene | Aldrich Chemical | 98% |
| 12-crown-4 | Aldrich Chemical | 98% |
| 1-naphthol | Aldrich Chemical | 99% |
| 2-propanol | Aldrich Chemical | ACS Grade |
| 9-methylanthracene | Aldrich Chemical | 98% |
| acetone | Aldrich Chemical | ACS Grade |
| acetonitrile | Fisher Scientific | HPLC Grade |
| anisole | Aldrich Chemical | ACS Grade |
| anthracene | Aldrich Chemical | 99% |
| benzene | Aldrich Chemical | ACS Grade |
| chlorobenzene | Fisher Scientific | HPLC Grade |
| chloroform | Fisher Scientific | HPLC Grade |
| cyclohexane | Aldrich Chemical | ACS Grade |
| decanoic acid | Aldrich Chemical | 98% |
| dimethyl sulfoxide | Aldrich Chemical | ACS Grade |
| ethanol | AAPER Alcohol and Chem. Co. | ACS Grade |
| ethyl acetate | Aldrich Chemical | ACS Grade |
| ethylbenzene | Aldrich Chemical | ACS Grade |
| fluorobenzene | Aldrich Chemical | ACS Grade |
| heptane | Fisher Scientific | HPLC Grade |
| hexafluorobenzene | Lancaster Synthesis | 99% |
| hexanes | Fisher Scientific | HPLC Grade |
| iso-octane | Fisher Scientific | HPLC Grade |
| methanol | Fisher Scientific | HPLC Grade |
| methylene chloride | Fisher Scientific | HPLC Grade |
| *N*,*N*-dimethylaniline | Aldrich Chemical | 99.5% |
| *N*,*N*-dimethylformamide | Aldrich Chemical | ACS Grade |
| naphthalene | Aldrich Chemical | 99% |
| *o*-xylene | Aldrich Chemical | ACS Grade |
| polyethylene glycol 200 | Aldrich Chemical | |
| polyethylene glycol 600 | Aldrich Chemical | |
| *p*-xylene | Aldrich Chemical | ACS Grade |
| reserpine | Aldrich Chemical | 99% |
| rhodamine 110 | Eastman Kodak Co. (item 4453) | |
| rhodamine B | Eastman Kodak Co. (item 11927) | |
| tetrahydrofuran | Fisher Scientific | HPLC Grade |
| toluene | Fisher Scientific | HPLC Grade |
| tributylamine | Aldrich Chemical | 99% |

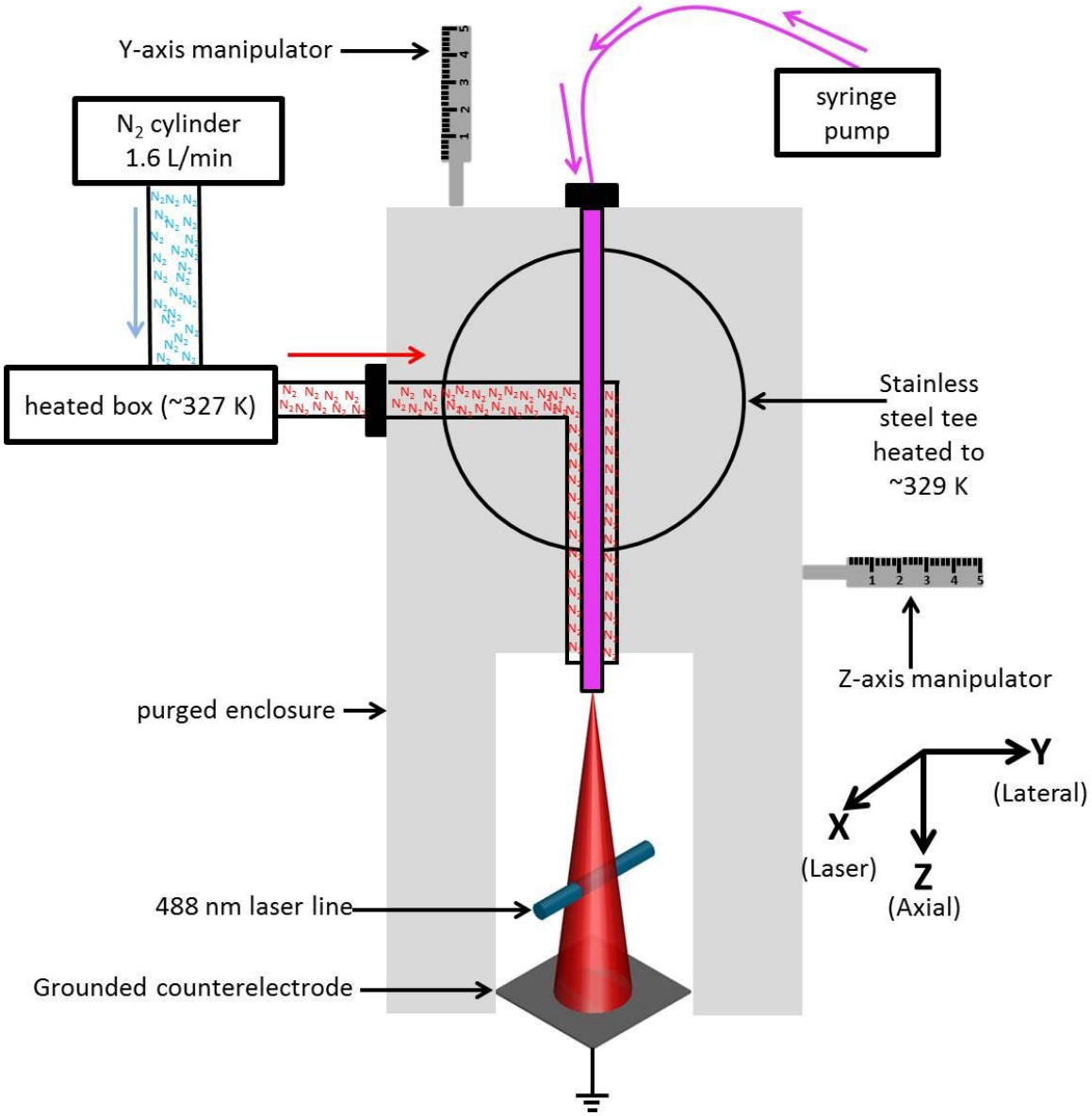


**Figure 2.1**: Schematic of the purged enclosure.

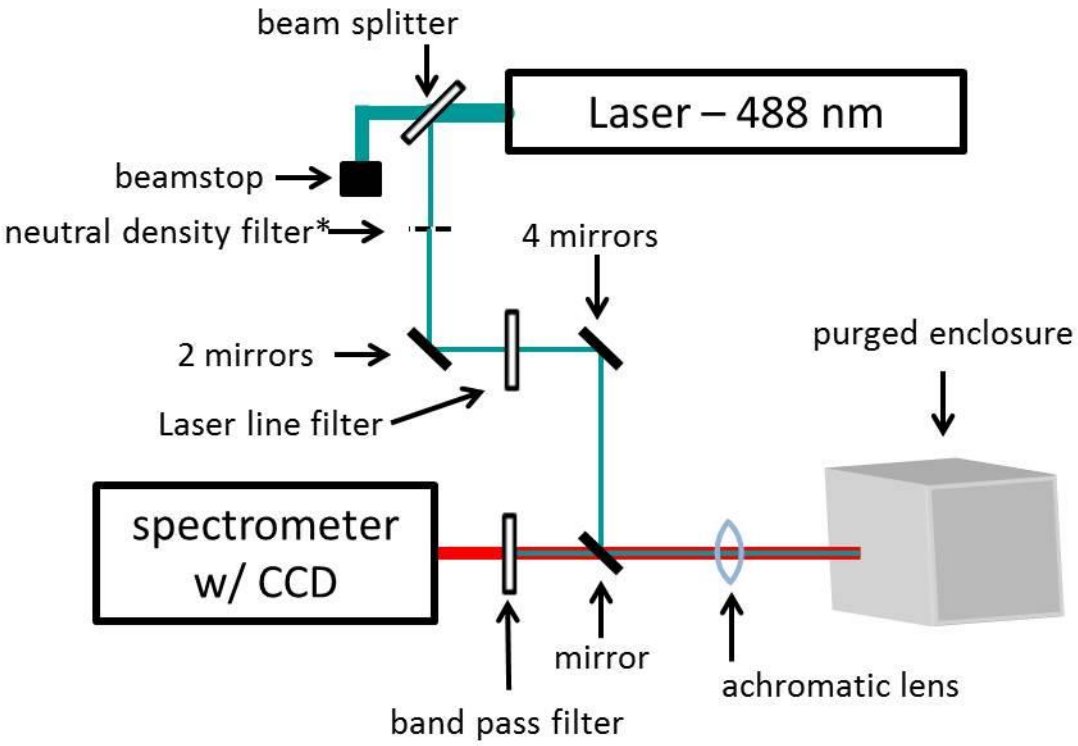


**Figure 2.2**: Schematic of the optical system used in the temperature experiments. * = the neutral density filter was in the beam path only during temperature calibration of the fluorescent mixture.

passing through a beam splitter, 2) losses due to scattering, and 3) losses due to passing through a laser line filter. While probing analytes contained in a cuvette, a neutral density filter (optical density = 2) was placed in the laser beam path to avoid detector saturation, further attenuating the laser power. The laser cross section at the focal point was ~0.2 millimeter (mm). The depth of field was measured by translating a cuvette (path length = 1 mm) containing RhB along the laser path in ~0.125 mm increments. A distance of 1.3 ± 0.2 mm was calculated by examining the range of distance observed at half the maximum intensity (full-width half maximum; FWHM). Fluorescence spectra were acquired in the backscattering mode on the macrostage of a spectrometer (Horiba Jobin Yvon, Edison, NJ; model T64000). The spectrometer was equipped with a 488-nm long-pass edge filter to remove elastically scattered laser radiation (the Rayleigh line) and protect the 1024 x 256 open electrode charge-coupled device (CCD) array detector (Horiba Jobin Yvon; model 354308). Data were acquired in the single spectrograph mode over the wavelength range 510-580 nm (unless otherwise noted). The macrostage uses confocal optics, whereby both excitation and emission radiation pass through a single lens positioned near the sample. A 600 groove/mm grating was used to collect the full spectral range (at the cost of lower resolution) required to view a majority of both dyes' emission wavelengths in a single acquisition (see below).

### 2.2.3 Electrospray Source

A home-made ES source (see Figure 2.1) was used in these experiments. The emitter consisted of a standard 1/8 inch (in) stainless steel tee (Valco, Houston, TX; product number ZT2) with graphite ferrules holding a stainless steel capillary [250 micrometer (μm) internal diameter (i.d.) x 500 μm outer diameter (o.d.)] used for liquid sample introduction. A second stainless steel capillary (690 μm i.d. x 3.33 mm o.d.) placed concentrically around the spray capillary was used to introduce a coaxial flow of $N_2$ nebulizing gas (Airgas Co., Knoxville TN; industrial grade, 99.95%) at a flow rate of 1.6 liters per minute (L/min). The gas flow rate was measured with a gas flow meter (Brooks Rotameter Co., Lansdale, PA; model 4-15-2).

The emitter tip on the inner capillary was routinely maintained using a diamond-coated file (Diamond Machining Technology, Marlborough, MA) and lathe (American Edelstaal UNIMAT-SL, New York, NY; model DB200) in order to prevent electrical discharge.[98] The inner capillary tip was extended ~ 1.5 mm beyond the outer capillary tip. A square [2.54 x 2.54 centimeter (cm)], stainless steel counter-electrode (Kimball Physics, Wilton, NH; SS-PL-C7X7-B) was oriented orthogonally to the spray axis and was placed ~15 mm downstream from the ES tip. Both the tee and counter-electrode were electrically isolated from their supports by Delrin™ holders.

The ES source was housed in a 18.5 x 16.0 x 7.5 cm purged enclosure made of transparent 2-mm thick poly(methyl methacrylate) to enhance thermal insulation

and to reduce the impact of changes in ambient conditions. One side of the purged enclosure consisted of a hinged door to allow access to the ES source. A 5.0 x 5.0 cm hole was cut at the bottom of the door to allow the laser and resulting fluorescence emission to pass. The purged enclosure containing the ES source was mounted on two manipulators oriented orthogonally to each other. These afforded the ability to translate the source and purged enclosure relative to the optical path (i.e., the X-axis) (Y-axis manipulator: Mitufoyo, Aurora, IL; Z-axis: L.S. Starrett Co., Athol, MA, model number 63). The purged enclosure and both manipulators were mounted on a single vertical manipulator that was used for gross adjustments to the entire apparatus. The spray was operated at least 30 min prior to data collection, providing methanol vapor and nitrogen gas sufficient to flush the purged enclosure ~20 times while displacing ambient air.

The spray was operated in positive ion mode. The emitter was held at +4.0 kV, supplied by a high-voltage power supply (Gamma High Voltage Research, Ormand Beach, Fl; model RR50-1.2SR/DDPM), and served as the anode. The counter-electrode was held at Earth ground and served as the cathode. The current at the counterelectrode was measured with a digital multimeter/scanner (Keithley, Cleveland, OH; model 199). Sample solution was introduced into the inner capillary by way of a ~68 cm long 0.100 μm i.d. Connex deactivated fused silica capillary (J&W Scientific, Folsom, CA; product number 160-2635) via a syringe pump (Harvard Apparatus, Holliston, MA; model 11).

$N_2$ gas used by the ES source first passed through a ~3 m plastic tube (i.d. 0.5 cm) before being heated. The plastic tubing was connected to ~3.5 m of copper tubing (i.d. 0.2 cm). A portion of the copper tubing (~3.0 m) was coiled inside a ceramic box (23 x 39 x 7 cm), which was stuffed with glass wool to provide thermal insulation. The coiled copper tube was placed on a heating pad and heated to ~329 K, as measured by a thermocouple (Omega, Stamford, CT) and thermometer (Omega, model HH-51). The remaining ~0.5 m of copper tubing extended from the ceramic box to the ES source and was wrapped in glass wool held with aluminum foil. A thermocouple (Omega, Stamford, CT) and thermometer (Omega, model HH-51) measured gas delivered into the ES source tee at ~327 K.

### 2.2.4 Sample Preparation

A solution containing 5.0 micromolar (μM) Rhodamine B (RhB) and 0.50 μM Rhodamine 110 (Rh110) in methanol was prepared from separate ~0.5 millimolar (mM) dye stock solutions that were prepared fresh every 3-4 days to avoid degradation artifacts. The 10:1 mixture ratio was used in order to obtain similar emission intensities for the two dyes. The concentrations above were used to obtain 90% detector saturation at a 10-s acquisition time at the Z = 0.25 mm, Y = 0 mm position in the spray.

### 2.2.5 Temperature Calibration of Dye Solution

The fluorescence emission intensity ratio of RhB (567 nm) to Rh110 (523 nm) was used as a measure of spray temperature. Calibration was performed by

placing an aliquot of the mixed dye solution in a thermostated 1.0 x 1.0 cm glass cuvette (Starna, Atascadero, CA) positioned on the macrostage of the spectrometer along the laser path (X-axis) in such a way as to maximize the Rh110 fluorescence signal (see Section 3.3.1 for further information). This resulted in a laser focus near the front face of the cuvette. Temperature was maintained with a circulating water bath (Haake, Berlin, Germany; model F 4391). The temperature of the solution in the cuvette was monitored using a linear thermistor probe (Omega, Stamford, CT; OL-700 series) and a digital multimeter (DMM)/scanner (Keithley, Cleveland, OH; model 199). The probe was calibrated in a water bath cooled and heated to 273 and 373 K, respectively, and adjusted with barometric pressure.

The linear thermistor probe was inserted through a hole drilled through a circular cuvette cap to provide support to the thermistor. The probe was wrapped with Teflon tape ~ 2 cm from the tip to seal it to the cap and thereby prevent solvent evaporation (which would affect analyte concentration), and to ensure it would remain stationary. The cuvette was filled with ~3 mL analyte, sufficient to cover the 0.5-cm long probe tip entirely. Careful attention was given to the proximity of the probe to the laser beam path through the cuvette. The probe must be close enough to the sampled area to give a representative temperature, but far enough away to avoid significant interaction between the probe and laser. The tip of the probe was positioned 2-mm above the laser beam path through the cuvette.

Due to the high fluorophore density in the cuvette, an optical density (OD) = 2 neutral density filter was placed in the laser beam path before the sample to avoid

detector saturation and sample photodegradation. Ten 1-s acquisitions were signal-averaged to improve the signal-to-noise ratio. Between each set of acquisitions, the laser shutter was closed to minimize sample photodegradation.

### 2.2.6 Electrospray Mass Spectrometry

Electrospray mass spectra of the dye mixture solution were acquired with a JEOL model JMS-T100LC (AccuTOF) orthogonal time-of-flight mass spectrometer (Peabody, MA). The needle, orifice 1, and ion guide peak voltages were 2500, 30, and 800 V, respectively. The desolvation chamber temperature was 573 K. A 10 μL aliquot of the sample was delivered via flow injection from a syringe loading injector (Rheodyne, Rohnert, CA; model 7125) at 50 μL/min by use of a syringe pump (Harvard Apparatus, Holliston, MA; model 55-2222).

### 2.2.7 Absorption Studies

Absorption spectra were obtained at ambient temperature using a Thermo UV-1 scanning double-beam spectrophotometer. Glass cuvettes (see above) were used with a methanol blank. The wavelength range was 400 – 600 nm. The scan rate was 0.5 nm/s.

## 2.3 Procedures

### 2.3.1 Acquiring Spectra from ES Plume

To generate profiles of the spray plume, the electrospray apparatus was translated parallel (Z-axis; axial profiles) or orthogonal (Y-axis; lateral profiles) to

the (vertical, downward) spray axis while the laser remained fixed along the X-axis (see Figure 3.3). Ten 10-s acquisitions were averaged for each data point by the spectrometer software. Each data point was taken in triplicate.

Spectra for axial profiles at Y = 0 were acquired in random sequence at 15 specific Z-axis positions between 0.25 and 12 mm from the emitter tip: 0.25, 0.50, 0.75, 1.0, 2.0, 3.0, 4.0, 5.0, 6.0, 7.0, 8.0, 9.0, 10.0, 11.0, and 12.0 mm. At Z > 12 mm, the signal intensities became erratic, probably due to the interaction between the laser and deposited solid and/or liquid on the counterelectrode. Temperatures are therefore reported only for distances ≤ 12 mm. Hysteresis was mitigated by consistently approaching the intended position from the low value side.

Lateral profiles were obtained at four different Z-axis positions, with each profile including up to seven different Y values taken in random sequence. Due to the conical nature of the spray, the number of lateral points increased as axial distance increased. Distances were chosen to capture all spray features. Lateral profiles at axial position Z = 0.25 mm: -0.1, -0.05, 0.00, 0.05, and 0.1 mm. Lateral profiles at axial position Z = 1 mm: -0.2, -0.1, 0.0, 0.1, and 0.2 mm. Lateral profiles at axial position Z = 4 mm: -0.6, -0.4, -0.2, 0.0, 0.2, 0.4, and 0.6 mm. Lateral profiles at axial position Z = 7 mm: -1.4, -1.2, -1.0, -0.8, -0.6, -0.4, -0.2, 0.0, 0.2, 0.4, 0.6, 0.8, 1.0, 1.2, and 1.4 mm. In each lateral profile, the maximum |Y| value was that for which the signal-to-noise ratio fell to ≤ 10.

### 2.3.2 Modeling

Calculations were performed with Microsoft Excel 2010 (Redmond, WA). Least-squares fits were created via successive approximations by optimizing one parameter at a time. Although the pitfalls of this approach were recognized, arriving at the same optimized parameter values even when parameters were optimized in different sequences increased confidence of discovering the global minimum. Uncertainties for fitting parameters representing 1 standard deviation (sigma; σ) were determined from the experimental pooled standard deviation and the sum squared error (i.e., the squared difference between experimental data and model predictions), as described in ref 27. Pearson correlation coefficients (R) were generated via Origin-Pro 8.1 (OriginLab, Northampton, MA).

## 2.4 DART Mechanism Study

### 2.4.1 Instrumentation

Schematics of the DART-TOF configuration and sampling technique are shown in Figure 1.4 and 2.4.

### 2.4.2 Mass Spectrometer

Experiments were performed using a JEOL model JMS-T100LC (AccuTOF) orthogonal time-of-flight mass spectrometer (Peabody, MA), which was fit with either an electrospray source (JEOL) or an IonSense (Danvers, MA) DART source. The following DART source and AccuTOF settings were chosen to minimize in-source fragmentation for the selected analytes.

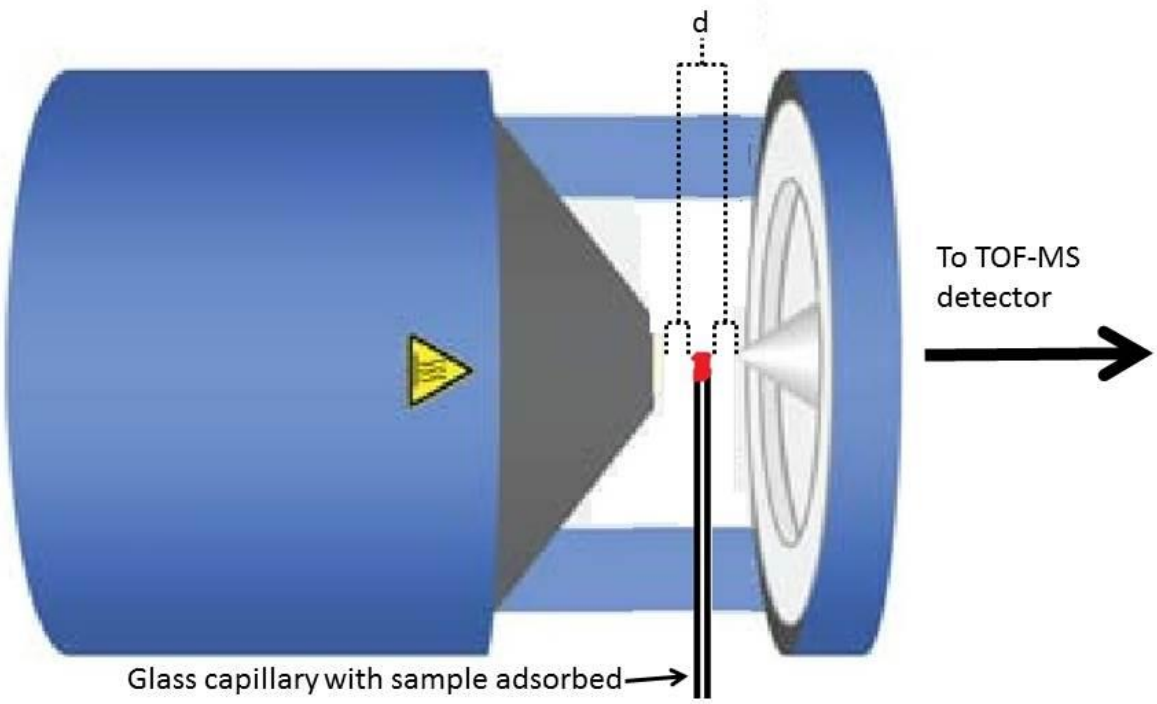


**Figure 2.3**: Visual Representation of DART (from above). The capillary is positioned equidistant (distance 'd') between the source outlet and entrance orifice to the TOF. Adapted from Ref. 156.

The DART source used helium gas at a flow rate of 4 L/min. The flow factor, a software setting implemented to mimic a flow controller by controlling the size of the gas flow valve opening based on the gas identity, was set to 0.3. The gas heater, needle voltage, grid electrode voltage, and discharge electrode voltage settings of the DART source were 573 K, 3000 V, 250 V, and 150 V, respectively. The general controlling parameters for the AccuTOF were as follows: temperature at orifice 1, 80 °C; voltage at orifice 1, 20 V; voltage at orifice 2, 3 V; ring lens voltage, 3 V; and peak voltage, 200 V. The distance between the DART source gas outlet and orifice 1 of the AccuTOF, ~1cm, was set by maximizing the $(H_2O)_2^{+\bullet}$ abundance.

### 2.4.3 Calibration

The AccuTOF system was tuned to a resolving power of over 6000 at FWHM using the electrospray ion source with 1 microgram per milliliter (μg/mL) reserpine in methanol. Calibration of the mass axis was performed twice a week using DART with a mixture solution of 5 μL/mL PEG 200 and 10 μL/mL PEG 600 in a solvent of 1:1 methanol:methylene chloride using the $[M + H]^+$ ion series, according to vendor-recommended operating procedures.

### 2.4.4 Sampling Method

Sample introduction was performed by depositing liquid or solid samples onto the closed end of a Pyrex 90 mm long closed end melting point capillary (Corning Life Sciences, Corning, NY; product number 9530-3) by dipping directly into the pure ("neat") or dissolved analyte. Data acquisition began before the

sample was introduced to the source due to software limitations. Sample introduction was accomplished by orientating a glass melting point capillary perpendicular to the ground below the helium gas stream. The closed end of the capillary was passed through the helium gas stream by hand toward the ceiling, in a slow and consistent motion. Effort was made to pass in an equidistant fashion between the DART source outlet and orifice 1 of the AccuTOF (see Figure 2.4). Sample ionization was instantaneous after the DART gas stream contacted the sample. Sample introduction was repeated six times to generate six reconstructed total ion current (RTIC) peaks in each analysis. Spectra were recorded at a 0.5 s interval. The mass acquisition range was 10-300 *m/z* for solvents and 120-200 *m/z* for analyte solutions (to prevent intense solvent ion peaks from overshadowing analyte ions). Spectra shown in Chapter 4 represent the mass spectra corresponding to the maximum RTIC profile peak.

# Chapter 3. Fluorescent Measurement and Modeling of Droplet Temperature Changes in an Electrospray Plume

## 3.1 Introduction

### 3.1.1 Motivation

The relationship between analyte ions formed in an electrospray (ES) and those present in bulk solution may be elucidated by considering spray-induced physical and chemical changes.[82,112,142,143,144] For example, noncovalent interactions may be affected by pH and polarity changes that occur in ES droplets.[107,108,157,118] Zhao and Cook[109,111] investigated these interactions by pioneering a method to interrogate the ES plume using laser-induced fluorescence (LIF) with polarity- and pH-sensitive fluorophores. Others, such as Zenobi[113], Antoine[96], and Parks[116] implemented this technique to develop a relationship between pH changes and charge state distributions of peptide anions, and to study spray-induced conformational changes of cytochrome c, respectively.

Temperature is another parameter that can affect solute chemistry either directly (*e.g.*, by affecting the conformation of biopolymers[117]) or indirectly (e.g., by affecting solvent evaporation and fractionation processes). Droplet cooling is recognized[118] to have an effect on the kinetics and equilibria of reactants in the spray, but has not been thoroughly examined. Tang and Kebarle[50] estimated the evaporative cooling process of 10-nm methanol droplets and estimated a temperature decrease of ~306 to 298 K for such a droplet. However, droplets of such a small size are generally remnants from Rayleigh subdivisions or nearly fully desolvated parent droplets; for a conventional ES setup, initial droplet radii

range[51,60,95,158,159] from 4 – 40 μm. Temperature behavior of larger, generally younger droplets is unknown and has not been experimentally or theoretically determined.

To probe the temperature of ES droplets, the fluorophore rhodamine B (RhB) was chosen due to its temperature-dependent emission intensity. Intensity variations not due to temperature (e.g., laser power fluctuations and concentration) will be minimized with the use of a temperature-insensitive fluorophore standard-rhodamine 110. The dye pair allows a ratiometric determination of droplet temperatures at various positions in the ES plume. RhB and Rh110 serve well as a dye pair since their absorbance wavelengths are close enough so that they may be excited by a lone conventional visible laser. Conveniently, their emission wavelengths are ~45 nm apart, making them easily differentiable, but are still able to fit into the same spectral window. Temperature points are gathered along the spray axis (an axial profile) and at various positions perpendicular to the spray axis (lateral profiles).

Evaporative modeling was also performed to provide insight into droplet characteristics and dynamics. Kebarle and Tang[50] were the first to relate one of two evaporation models (the surface-controlled evaporation model; an evaporation model for droplets below a solvent-specific critical droplet radius) to ES. Further, they further predicted 10-nm droplets cool ~8 K in ~8 μs. Each model, the surface-controlled and the diffusion-controlled (for droplets above a critical radius), is

assessed with respect to experimental electrospray temperature data for the first time.

### 3.1.2 Consideration of Potential Artifacts

It is important to consider a number of artifacts that might affect the temperature extracted from fluorescence thermometry measurements. Evaporation of droplets will reduce their radii and volume, causing the concentration of their contents to increase. This creates a discrepancy between the dye concentration of a solution used in calibration and that of any droplet which has undergone evaporation. Evaporative losses will also induce pH changes[109]. Cross absorption of dye emission light may occur, and preferential ion emission of one dye over another (due to larger surface activity of one dye compared to another) in droplets may skew dye fluorescent intensities. Concentration and pH changes require knowledge of droplet size. The proceeding axial temperature profile data (Section 3.2.2) will be supported by modelling (Section 3.2.4), whereby estimates of reasonable droplet size throughout the interrogated area will be provided. A reduction in droplet size may be estimated off which concentration studies may be based.

Chamarthy[160] reported the effect of concentration on RhB and Rh110 fluorescent emission in deionized water in a study of heat flow in microchannel heat sinks. Calibration experiments were conducted using a 400-μm square glass microchannel submerged in a well of deionized water; the well was machined into an aluminum block. The microchannel containing the dyes were probed from 293

to 343 K in 2 K intervals. The dyes were analyzed individually and together in the microchannel at concentrations of 1, 5, and 10 mg/L. The intensity ratio of the dyes [$I_{max}$(RhB)/$I_{max}$(Rh110)] was plotted versus temperature as a function of dye concentration. This study displays a 20-25 K difference in temperature between concentration curves at the same ratio. Concentrations in the present study are significantly lower than those used by Chamarthy. Lower concentration implies any effect of concentration on calibration would be much smaller, but it remains to be seen whether or not the effect is negligible. Effects of concentration are described in Section 3.2.6.

The convenient proximity of the absorbance and emission wavelengths of the two dyes may introduce another artifact, namely cross-absorption, [an inner filter effect[161]: the absorbance of Rh110 fluorescence (emission $\lambda_{max,\ Rh110}$ = 523 nm) by RhB (absorption $\lambda_{max,\ RhB}$ = 554 nm] followed by reemission by RhB. This could decrease the fluorescence intensity of Rh110 and increase that for RhB. In the following experiment, the ratio $I_{max}$(RhB)/$I_{max}$(Rh110) is taken to provide a temperature-dependent ratio of the dye solution (see Section 3.2.1). Thus, cross-absorption effects discussed above would cause a temperature-independent increase in the measured fluorescence intensity ratio, skewing measured temperatures downward (see Section 3.2.1 for more detail). These kinds of effects can be probed by the cell-shift experiment[162] will be used to study the effect and is described in Section 3.2.6.

### 3.1.3 Experimental Description

In the following study, the temperature of droplets in the electrospray plume will be measured by optical fluorescence spectroscopy. This temperature will be ascertained from collecting emission intensity from the ratio of Rhodamine B, a temperature sensitive dye, to Rhodamine 110, a relatively temperature-insensitive dye that serves as a normalization factor. A custom-built electrospray source will be rastered in the beam path of an excitation laser in order to collect emission light from the dye pair. From this emission data, profiles will be created to illustrate droplet temperature evolution parallel to the emitter (*i.e.* axially, down the length of the spray plume) as well as at four positions perpendicular to the emitter (*i.e.* laterally; across the breadth of the spray plume). Two evaporation models will be assessed based on their applicability to the present system and used to support and expand upon experimental data. The models will be fit to axial experimental data in order to provide values for three parameters this lab was unable to measure: evaporative droplet size changes, solvent partial pressure, and droplet velocity. The reasonableness of these parameters is assessed and their contribution to droplet temperature is expanded upon. Three possible artifacts that might potentially interfere with temperature measurements (cross-absorption between dyes, preferential ion emission from droplets, and pH/concentration effects due to droplet evaporation) are explored.

## 3.2 Results and Discussion

### 3.2.1 Calibration of the Temperature Ratio

Calibration method and parameters are described in Section 2.2.5. Figure 3.1 displays representative spectra of the calibration solution in a cuvette at temperatures between the 274 and 303 K. A calibration curve (Figure 3.2) was constructed from these data by plotting the ratio of the maximum intensity from each dye at each individual temperature [$I_{max}$(RhB)/$I_{max}$(Rh110)]. The $R^2$, slope, and y-intercept are 0.9996, -0.01240 ± 0.0001, 1.453 ± 0.001, respectively.

### 3.2.2 Axial Temperature Profiles of the Electrospray Plume

Fluorescence spectra taken at various positions along the Z-axis (axially) at 15 positions are displayed in Figure 3.3. Spectral features in Figure 3.3 at ~528 and 550 nm are caused by cemented optics used in the macrostage of the spectrometer. The origin (Z = 0) is the tip of the electrospray emitter (Section 2.2.3). Intensity of both dyes decreases naturally due to the natural conical expansion of a spray as distance from the origin increases. Additionally, the ratio of the dye changes as a function of temperature. Referencing this ratio back to the calibration curve seen in Figure 3.2 allows temperature determination at any spray position. Ratios, ergo temperatures, are collected axially and laterally (at four axial positions) to create profiles of the temperature behavior of droplets.

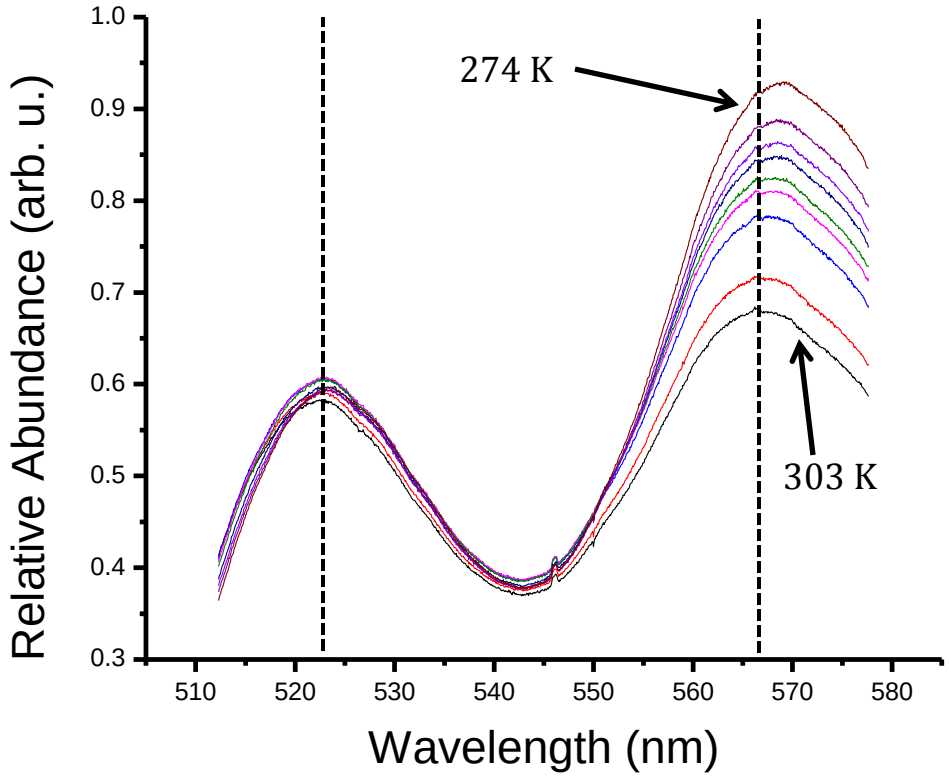


**Figure 3.1**: Representative fluorescence spectra of a mixture of Rhodamine 110 (left peak) and Rhodamine B (right peak) between 274 K and 303 K. The dotted line is placed at the apex intensity of each dye peak at 303 K as a reference to illustrate shifts in wavelength.

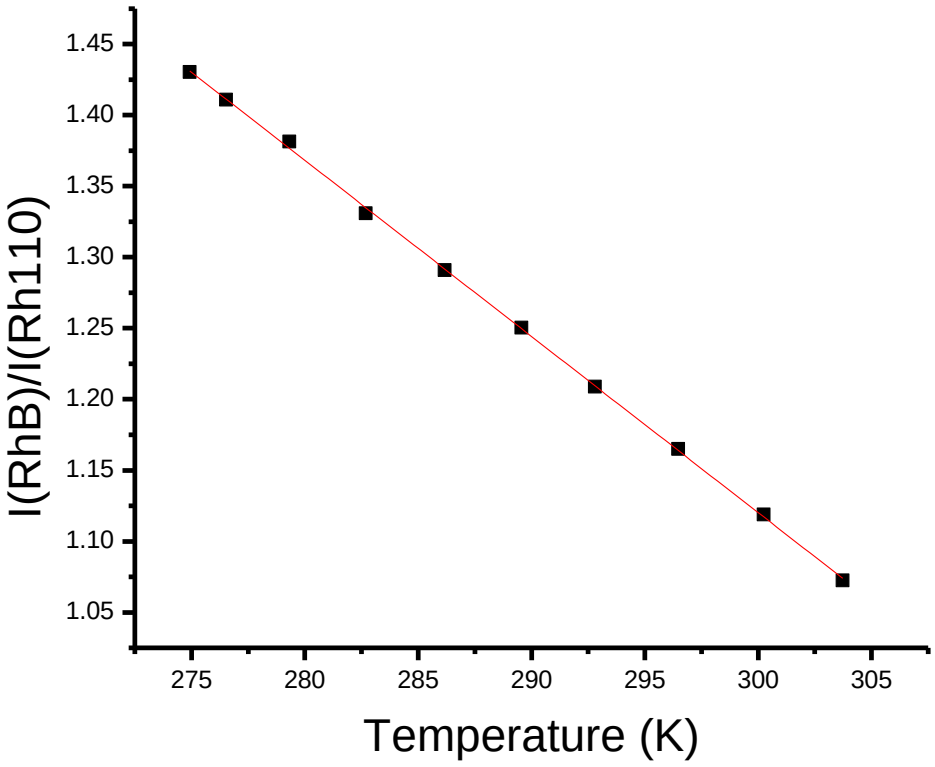


**Figure 3.2:** Temperature calibration curve derived from data presented in Figure 3.1.

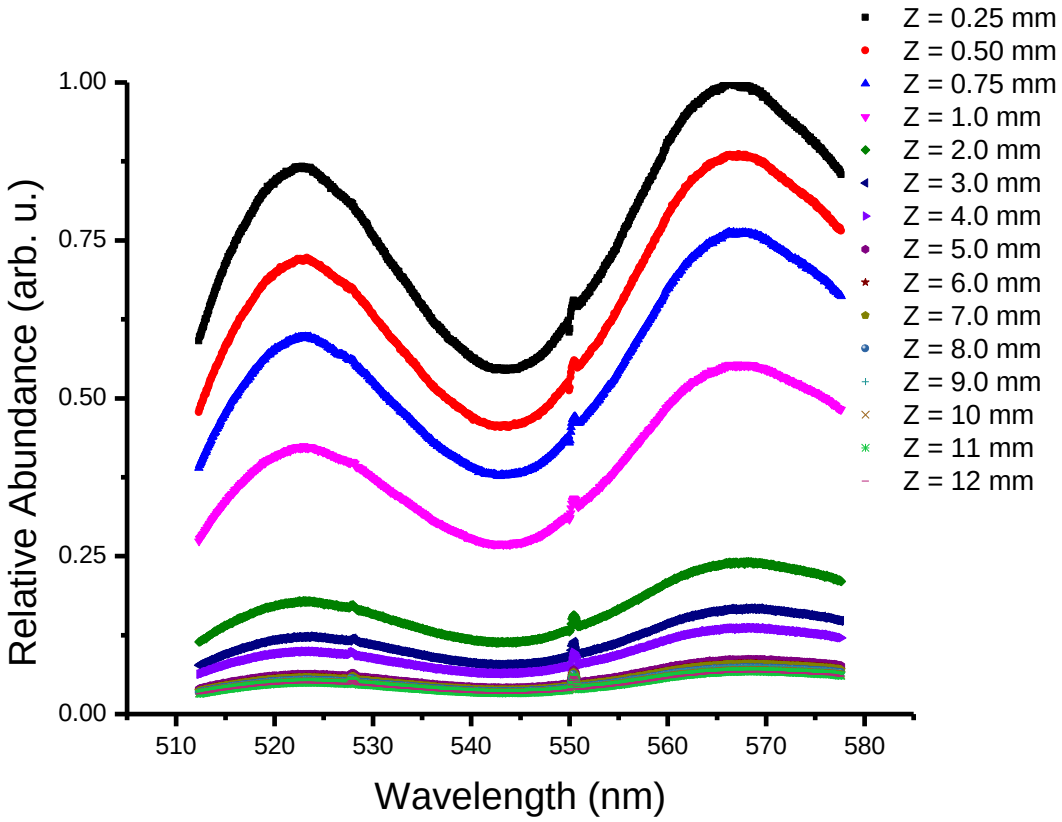


**Figure 3.3:** Axial profile spectra taken at 25 uL/min at the listed Z positions.

Axial temperature profiles of ES plumes created using various solvent flow rates ($F$ = 12.5, 25, and 50 μL/min) are shown in Figure. 3.4 (see Figure 3.3 for spectra used to construct the profile at $F$ = 25 μL/min). There is a significant decrease in temperature from the spray tip to approximately Z = 3 - 5 mm followed by slight reheating. The initial cooling qualitatively resembles that predicted by Kebarle[50] and is attributable to endothermic solvent evaporation. Reheating at larger Z may be attributed to a thermal competition whereby the evaporative cooling process (slower at lower temperatures) is overtaken by collisional warming by ambient background and/or heated nebulizing gas. At larger Z, the droplets are expected to be smaller, with correspondingly higher surface-to-volume ratio and lower heat capacity, potentially enhancing the warming effect of collisions. Collisional frequency may also be enhanced at larger Z by turbulence from gas reflection off the counterelectrode; this may contribute to droplet reheating. Further study (outside the scope of this work) is required to understand the mechanism of rewarming.

Two differences are evident at lower $F$ (Figure 3.4): a slightly steeper initial temperature drop followed by greater reheating (see Figure 3.4b for detail between Z = 0.25 and 4 mm). Several factors likely contribute, relating to droplet size, velocity, and environment. Among the factors affecting the rate of solvent evaporation is the partial pressure of solvent vapor in the surrounding environment, designated $P_\infty$.

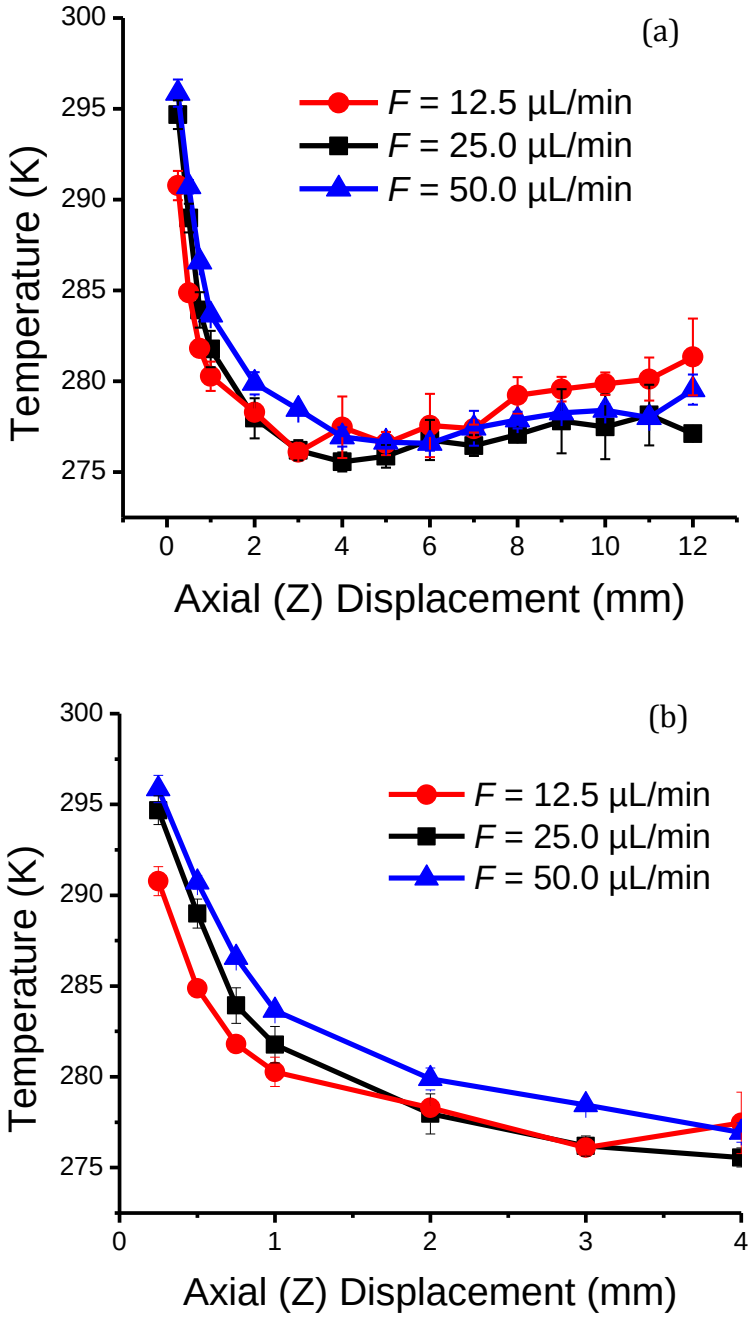


**Figure 3.4**: Axial temperature profiles through the center of the spray (Y = 0) at indicated flow rates. Figure (a) displays the full profile; Figure (b) displays Z = 0.25 mm to 4.0 mm, illustrating rates of temperature decrease among various flow rates.

Employment of the purged enclosure to contain the spray apparatus allows estimation of $P_\infty$ from the assumptions that 1) the total ambient pressure is roughly 760 Torr; 2) the mole ratio of carrier gas to solvent is approximately the same as the mole ratio of their flow rates; and 3) ambient air is swept from the box during the 30-minute pre-measurement equilibration period. $P_\infty$ calculated from these assumptions is approximately 4, 8, and 16 Torr at $F$ = 12.5, 25 and 50 μL/min, respectively, considerably less than the saturated methanol vapor pressure of ~100 Torr at room temperature. Based solely on this trend, evaporation should be enhanced at lower $F$, consistent with the observed enhancement of initial cooling.

Complex effects of $F$ on droplet velocity and size[92] may also contribute to the trends evident in Figure 3.4. The liquid flow velocity ($v_F$; calculated from $F$ and the capillary i.d.) decreases from 1.7 to 0.42 cm/s as $F$ decreases from 50.0 to 12.5 μL/min. These values are small compared with droplet velocities measured elsewhere by Doppler phase anemometry[51] (~2-3 m/s), suggesting at most a small contribution, albeit in a direction consistent with the trends of Figure 3.4.

A more significant effect may derive from the interplay between $F$ and the measured spray current ($I$). From the data in Table 3.1, charge density within the droplets (proportional to $I/F$) would appear to increase slightly from $F$ = 12.5 to 25 μL/min, then fall as $F$ is increased to 50 μL/min. The initial increase is unexpected and may result from the uncertainty in measuring small $I$; the decrease from 25 to 50 μL/min is consistent with predictions of Fernandez de la Mora[92]

**Table 3.1**: Measured experimental parameters for axial profiles taken at three flow rates.

| Experimental Parameter | | | |
|---|---|---|---|
| Solvent Flow Rate ($F$; µL/min) | 12.5 | 25.0 | 50.0 |
| Emission Current ($I$; µA) | 0.055 | 0.12 | 0.19 |
| Droplet Temperature ($T_{d,0}$; K) at Z = 0.25 | 290.8 ± 0.8 | 294.7 ± 0.8 | 295.9 ± 0.8 |

Charge density would be expected to affect both the size of the droplets (smaller at higher *I/F*) and their acceleration by the extracting field and by collisions with the nebulizing gas[92,164] (more acceleration for smaller and more highly charged droplets). There may be offsetting effects: smaller droplets evaporate more quickly, but their higher velocity gives them less time to evaporate before reaching a given position.

Further study, including direct experimental measurement of droplet sizes and velocities (again, beyond the scope of this study), is necessary to unambiguously resolve these contributions, although some insight may be derived from modeling the cooling process (see Section 3.2.4).

### 3.2.3 Lateral Temperature Profiles of the Electrospray Plume

Lateral profiles obtained at various axial positions (Z = 0.25, 1.0, 4.0, and 7.0 mm) at three solvent flow rates (*F* = 12.5, 25, and 50 μL/min) are displayed in Figure 3.5. On-axis (Y = 0 mm) temperatures in these profiles generally follow trends presented in Figure 3.4. At Z = 0.25 and 1 mm, temperatures decrease sharply as the distance from the Z-axis increases. Smaller droplets have a higher surface-to-volume ratio, which promotes faster cooling- consistent with lower temperatures off-axis. Also, smaller droplets are preferentially driven to the periphery of the electrospray due to space charge[51,95] and simple dispersion effects. Downstream lateral profiles (Z = 4 and 7 mm) are relatively flat on-axis, suggesting that thermal equilibration and/or reduced polydispersity has occurred by this point.

**Figure 3.5:** Lateral temperature profiles at indicated axial (Z) positions each at 25 μL/min.

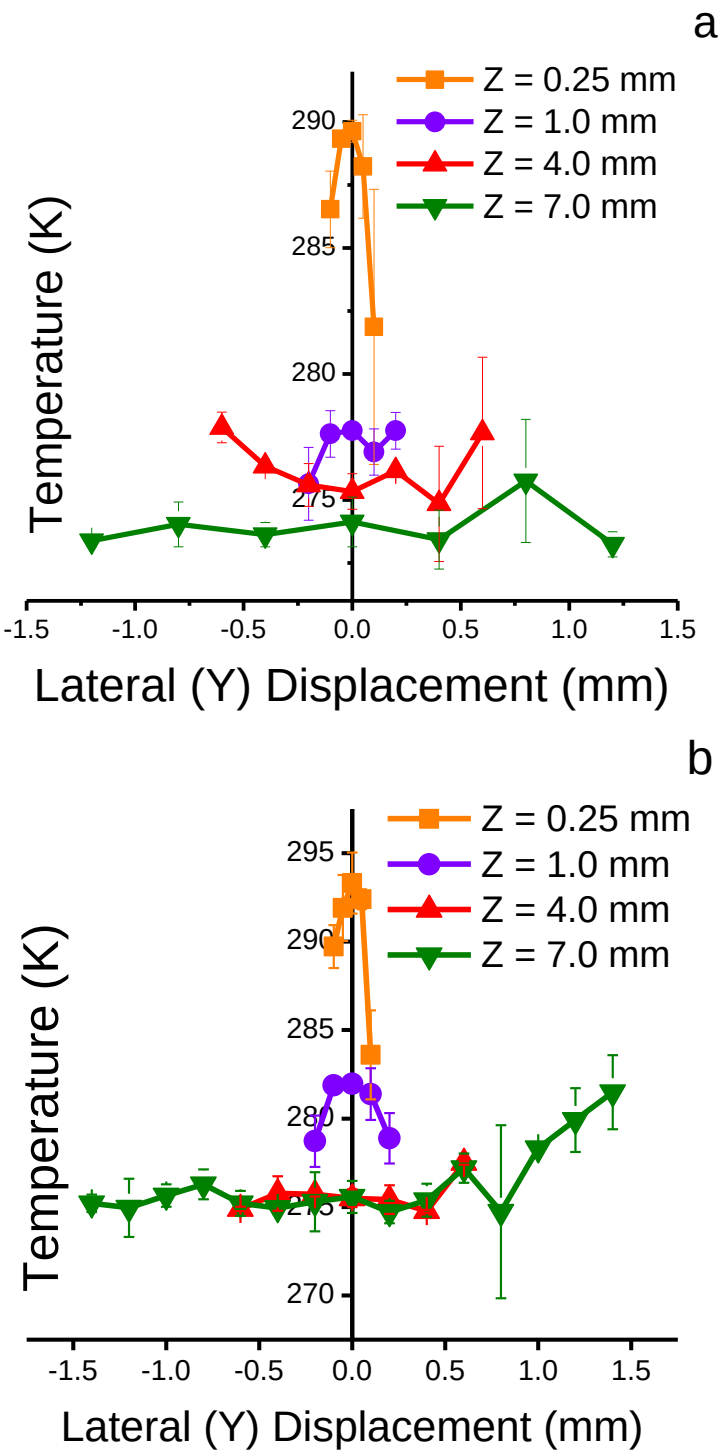


**Figure 3.5 Continued:** Lateral temperature profiles at indicated axial (Z) positions each at a) 12.5 µL/min, b)25 µL/min, and c) 50 µL/min.

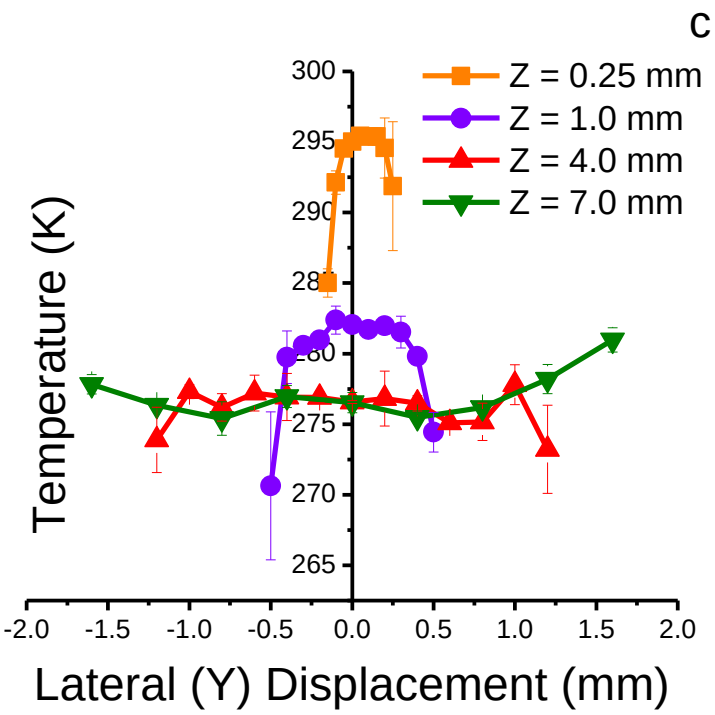


**Figure 3.5 Continued:** Lateral temperature profiles at indicated axial (Z) positions each at a) 12.5 µL/min, b)25 µL/min, and c) 50 µL/min.

At the periphery of the spray, these smaller droplets show some evidence of rewarming, possibly due to collisions with sheath gas or ambient air. Profiles at higher Z extend to higher Y values than those nearer to the emitter; the dispersion of the spray plume provides measurable signals farther into the periphery at higher Z, although the error bars in Figure 3.5 can become large at high Z and Y.

Figure 3.6 illustrates the impact of *F* on lateral profiles. These data are consistent with axial profile comparisons where higher *F* generally yields warmer temperatures at a given Z position. Data at Z = 4 and 7 mm heavily overlap, further suggesting thermal equilibrium and/or reduced polydispersity has occurred by this point.. Lateral profiles displayed in Figure 3.6 also reflect a physically broader spray plume at higher *F* (*i.e.*, S/N > 10 at larger |Y|), consistent with the greater amount of material present in the plume.

Lateral temperature profiles collected before the implementation of the emitter polishing procedure described in Section 2.2.3 show temperatures rising as |Y| increases. This temperature behavior, displayed in Figure 3.7, may be caused by electrical discharge, heating up periphery droplets. The inability to reproduce this behavior, despite multiple polishing events performed on multiple emitter capillaries, add confidence the assertion that lateral profile seen in Figure 3.5 are lateral profile results under normal (non-discharge) conditions.

**Figure 3.6:** Lateral temperature profiles at indicated flow rates at axial distances a) Z = 0.25 mm, b) Z = 1.0 mm, c) Z = 4.0 mm, and d) Z = 7.0 mm.

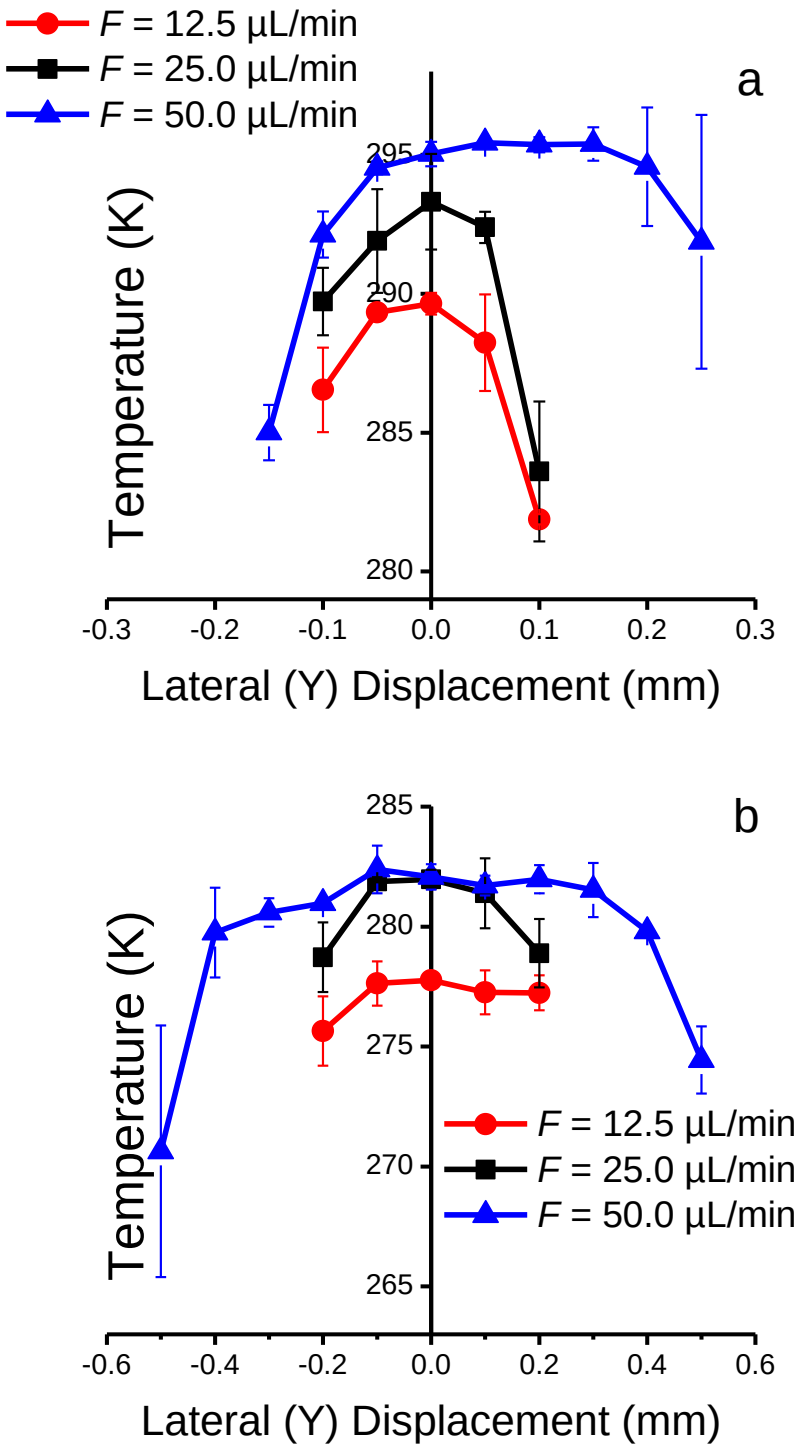


**Figure 3.6 Continued:** Lateral temperature profiles at indicated flow rates at axial distances a) Z = 0.25 mm, b) Z = 1.0 mm, c) Z = 4.0 mm, and d) Z = 7.0 mm.

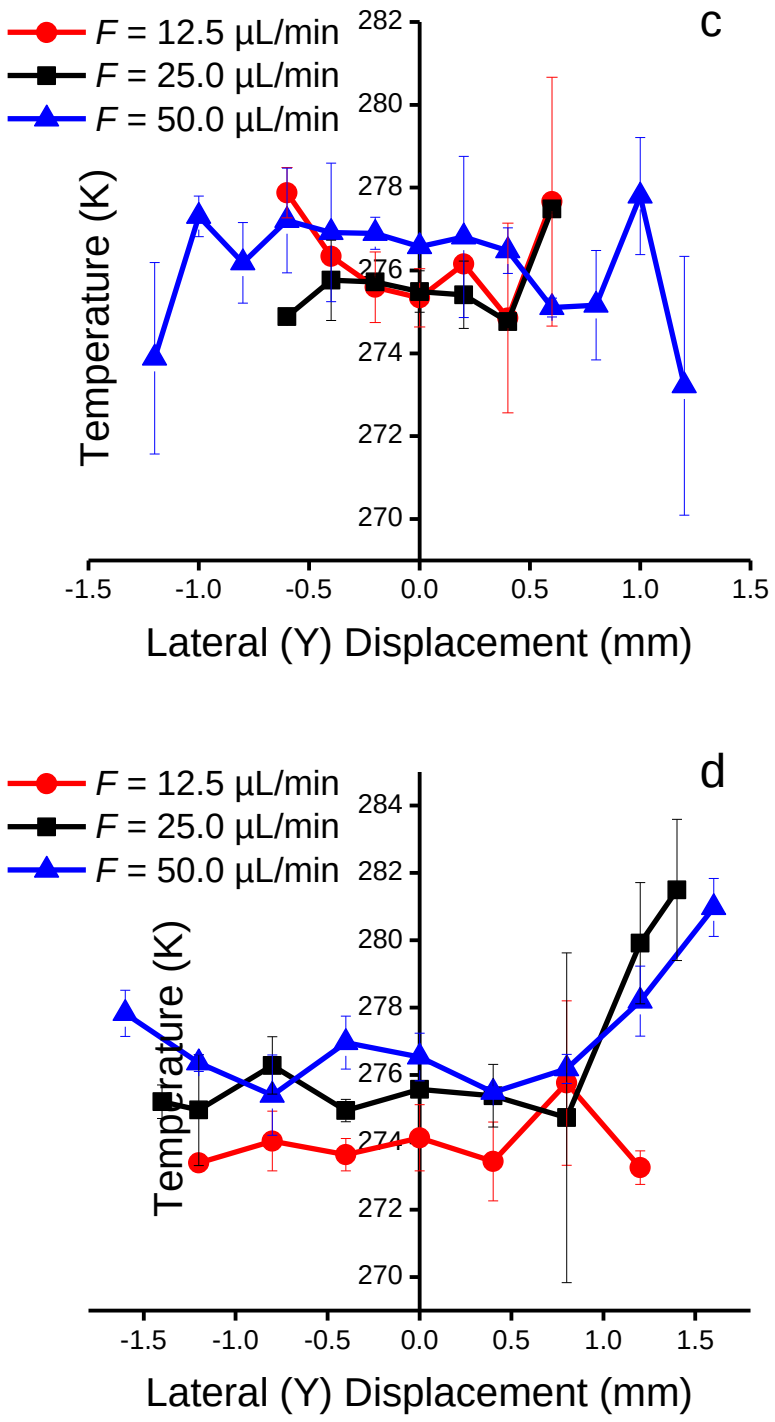


**Figure 3.6 Continued:** Lateral temperature profiles at indicated flow rates at axial distances a) Z = 0.25 mm, b) Z = 1.0 mm, c) Z = 4.0 mm, and d)_Z = 7.0 mm.

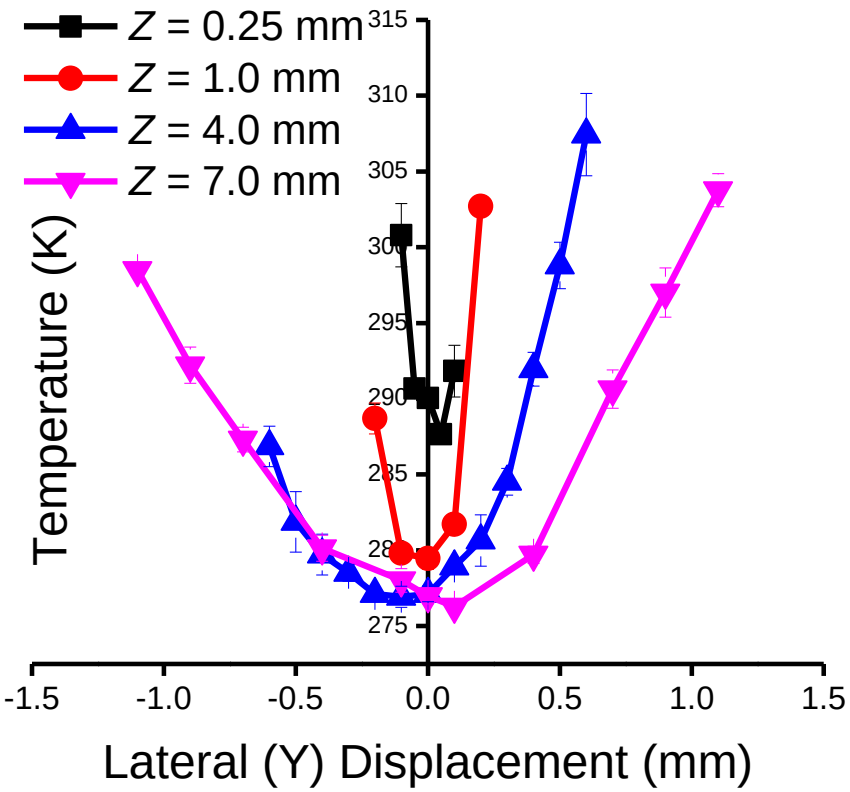


**Figure 3.7:** Lateral temperature profiles believed to be affected by electrical discharge at the indicated axial (Z) positions each at 25 μL/min.

### 3.2.4 Modeling

Evaporation of airborne droplets may be either diffusion-controlled (when the rate-limiting process is diffusion of vapor away from the droplet in the gas phase) or surface-controlled (for droplets too small to saturate the droplet's surface vapor layer).[81] The critical radius ($r_c$) for transition between these modes is defined as:

$$r_c = \frac{4 \cdot \lambda}{3 \cdot \alpha} \qquad \text{(Equation 3.1)}$$

where λ is the mean free path of vapor molecules in the gas around the droplet (~68 nm at 298.15 K and 760 Torr, using a 36.9-nm hard sphere diameter[165] for methanol)and α is the condensation coefficient (temperature-dependent probability of a solvent molecule reabsorbing upon collision with the droplet; α ~ 0.9 at 300 K for methanol[166]). The critical radius for methanol is thus about 0.10 μm under conditions used here. By contrast, droplet size measurements[51,60,95,158,159] indicate that the initial droplet radius $r_0$ should be on the order of 4.0 to 40 μm for conventional electrospray. From this simple consideration, evaporation should initially be diffusion-controlled, possibly transitioning to surface control later in the spray or for offspring droplets

Tang and Kebarle[50] were the first to estimate cooling during droplet evaporation in an electrospray. They suggested droplets of $r_0$ = 10.0 nm would undergo surface-controlled evaporation of, and estimated that such a droplet would cool to a temperature 8 K below that of its surroundings (306 K to 298 K) in about 8 μs. This small radius would apply to the final stages of residue or offspring droplet

evolution, nearing complete evaporation. Observation times corresponding to the distances presented in Figure 3.4 occur much earlier in the droplet lifetime and cover timespans much longer than those investigated by Kebarle. For example, assuming a constant droplet velocity of 2 m/s (as in Reference 51), the Z-axis (0-12 mm) of Figure 3.4 may be estimated to correspond to a timespan of 6 ms. Hence, it is of interest to ascertain whether the present data can be adequately described by the models discussed by Kebarle. Specifically, modeling of the evaporation process was undertaken to gain further insight into the cooling portion of the spray (Z = 0.25 to 5.00 mm in Figure 3.4). As noted above, the re-warming at Z > 5.0 mm cannot be ascribed to simple evaporation and thus is beyond the scope of simple evaporation models.

Droplet cooling was calculated using models adapted from Reference. 81 for both diffusion-controlled (DCM; Equation 3.2) and surface-controlled (SCM; Equation 3.3) evaporation:

$$\delta T_{d,diffusion} = -\frac{3}{r_d^2(Z)\cdot\rho'\cdot s'}\cdot\frac{\delta Z}{v_d}\left\{\frac{\overline{\nabla}\cdot M\cdot\bar{l}}{R_g}\cdot\left(\frac{P_d(Z)}{T_d}-\frac{P_\infty}{T_\infty}\right)-\bar{k}(T_\infty-T_d(Z))\right\}$$

(Equation 3.2)

$$\delta T_{d,surface} = -\frac{3}{r_d(Z)\cdot\rho'\cdot s'}\cdot\frac{\delta Z}{v_d}\left\{\frac{\alpha\cdot\bar{v}\cdot M\cdot\bar{l}}{4\cdot R_g}\cdot\left(\frac{P_d(Z)}{T_d}-\frac{P_\infty}{T_\infty}\right)-\frac{\bar{k}}{r_d(Z)}(T_\infty-T_d(Z))\right\}$$

(Equation 3.3)

where $\delta T_d$ is the change in a droplet's temperature over an incremental axial distance $\delta Z$ for a droplet moving at velocity $v_d$ ($\delta Z/v_d = \delta t$, the time increment used in Davies' model[81]); the other terms are defined in Table 3.2. Both Equation 3.2 and

Equation 3.3 may be broken down into components that individually account for evaporative cooling ($\frac{P_d(Z)}{T_d}$), solvent recondensation ($\frac{P_\infty}{T_\infty}$), and collisional warming ($T_\infty - T_d(Z)$) events a droplet experiences. For ease of discussion and to highlight the pertinent equation portions for each discussion, the common, multiplicative terms $-\frac{3}{r_d^2(Z)\cdot\rho'\cdot s'}\cdot\frac{\delta Z}{v_d}$ (from the DCM) and $-\frac{3}{r_d(Z)\cdot\rho'\cdot s'}\cdot\frac{\delta Z}{v_d}$ (from the SCM) are referred together as $D$; $\frac{\bar{\nabla}\cdot M\cdot\bar{l}}{R_g}$ (DCM) and $\frac{\alpha\cdot\bar{v}\cdot M\cdot\bar{l}}{4\cdot R_g}$ (SCM) are referred as $E$. The evaporative cooling term, $D\cdot E\cdot\frac{P_d(Z)}{T_d}$, always results in a decrease in droplet temperature due to $D$ term's negative sign. Higher vapor pressure of volatile solvents (*e.g.*, methanol compared to water; calculated from the Antoine equation- see Table 3.2) yield a faster cooling rate as well as a cooler initial droplet ($T_d$). Solvent recondensation ($D\cdot E\cdot\frac{P_\infty}{T_\infty}$) always results in an increase in droplet temperature due to the inherent negative in the D term multiplied by the minus symbol preceding $\frac{P_\infty}{T_\infty}$ in Equation 3.2 and 3.3. At higher values, the vapor pressure of the solvent in the surrounding gas, $P_\infty$, will inhibit the evaporation of the droplet solvent, resulting in warmer droplet temperatures; cooler ambient temperatures ($T_\infty$), also inhibits droplet cooling. Collisional warming ($D\cdot(T_\infty - T_d(Z))$) is the effect caused by energy transfer between gas molecules colliding with the droplet and is governed by the magnitude of temperature difference between the temperature of the droplet and ambient temperature of surrounding gas molecules.

**Table 3.2**: Parameters used in Chapter 3, in rough order of appearance

| Parameter | Definition | Value | Comments |
|---|---|---|---|
| $F$ | Liquid flow rate | | |
| $P_\infty$ | Partial vapor pressure of solvent in the surrounding gas | | Fitting parameter |
| $v_F$ | Liquid flow velocity | | |
| $I$ | Spray current | | Experimentally measured. |
| $r_c$ | Critical radius | | Radius at which transition between diffusion- and surface-controlled models occurs. |
| $\lambda$ | Gas mean free path | | |
| $\alpha$ | Condensation coefficient | 0.90 | For methanol at 300 K (Ref. 166). |
| $r_0$ | Droplet radius at $Z$ = 0.25 mm | | Fitting parameter; Expected values range from 4 - 40 μm (Refs. 51,60,95,158,159). |
| $\delta T_d$ | Change in droplet temperature $T_d$ in incremental distance $\delta Z$ | | Calculated using Equation 3.2 or 3.3 |
| $\delta Z$ | Incremental distance | 0.25 μm | Optimized to prevent round-off error while preserving sensitivity of parameters. |
| $v_d$ | Droplet velocity | | Fitting parameter |
| $\delta t$ | Evaporation time increment | $\delta Z/v_d$ | |
| $r_d(Z)$ | Droplet radius at axial position Z | | Calculated using Equation. 3.4 or 3.5. |
| $\rho'$ | Solvent density | 0.7914 g/mL | (Ref. 167) |
| $s'$ | Solvent specific heat | 2.531 J/g·K | (Ref. 167) |
| $\overline{\nabla}$ | Diffusion coefficient of solvent vapor in air | $\sqrt{\nabla_{T_\infty} \cdot \nabla_{T_d}}$ | $\nabla_{T_\infty}$ and $\nabla_{T_d}$ are calculated using Equation 3.6 (Ref. 168). |
| $M$ | Solvent molar mass | 32.04 g/mol | |
| $\bar{l}$ | Latent heat of solvent vaporization | $\sqrt{l_{T_\infty} \cdot l_{T_d}}$ | $l_{T_\infty}$ and $l_{T_d}$ are calculated via Equation 3.7. For methanol, A = 45.3, α = -0.3100 , β = 0.4241 (Ref. 169). The reduced temperature $T_r = T/T_c$, where the critical temperature $T_c$ of methanol = 512.6 K. |
| $R_g$ | Gas constant | 8.314 J/mol·K | |
| $\bar{v}$ | Mean speed of gaseous solvent | 445.2 m/s | For methanol at 300 K; calculated from Ref. 167. |

**Table 3.2 Continued** : Parameters used in Chapter 3, in rough order of appearance.

| Parameter | Definition | Value | Comments |
|---|---|---|---|
| $P_d(Z)$ | Solvent vapor pressure at the droplet surface | $\log P_d = A - (B/(C + T_d))$ | Calculated via the Antoine equation. For methanol in °C, A = 8.08097, B = 1582.27, and C = 239.7.[170] |
| $\bar{k}$ | Thermal conductivity of air | $\sqrt{k_{T_\infty} \cdot k_{T_d}}$ | $k_{T_\infty}$ and $k_{T_d}$ are calculated using interpolation from Ref. 171. |
| $k'$ | Thermal conductivity of liquid methanol | 0.203 W/m·K | For methanol at 300 K; Calculated by interpolation from Ref. 171. |
| $T_\infty$ | Ambient temperature | 303 ± 1 K | Average temperature and standard deviation from measurements at six positions inside the purged enclosure. |
| $T_d$ | Droplet surface temperature | | $T_{d,0}$ = measured temperature at Z = 0.25, Y = 0 mm at each flow rate (See Table 3.3); Subsequent values calculated by adding $\delta T_d$ from Equation 3.2 or 3.3 to the preceding value. |
| $T_f$ | Final droplet temperature | | Model-derived temperature at Z = 12 mm. |
| $t_{eq}$ | Time for temperature equilibration in a droplet | | Calculated using Equation 3.8. |
| $\lambda_{max}$ | Wavelength of maximum intensity or absorbance | | |

This term is influenced by droplet size to larger extent in the SCM when compared to the DCM due to the squared radius term (see Equation 3.3): the larger the droplet, the smaller the effect of collisional warming on the droplet. These three contributors are displayed for clarity over the interrogated axial distance in Figure 3.8.

When applying these equations, $\delta Z$ was selected to provide 1000 calculated points between the most closely spaced experimental data points ($\delta Z$ = 0.25 μm). Equations 3.2 and 3.3 apply to pure liquids, but since solute concentrations used were on the order of micromolar, colligative effects were assumed to be negligible. If substantial colligative effects were present, the rate of evaporation, ergo the rate of cooling, would be impeded due to the inherent stabilization occurring when solute is added to solvent. The first measured experimental temperature at Z = 0.25 mm, Y = 0 mm was presumed accurate and provided the initial value of droplet temperature ($T_{d,0}$), one boundary condition. If the droplet radius at this position is designated $r_0$, then $r_d$ at a given position (Z) (*i.e.* $r_d(Z)$) maybe calculated from Equation 3.4 for DCM evaporation[81] or Equation 3.5 for SCM evaporation:[50]

$$r_d(Z)_{diffusion} = \sqrt{r_0^2 - \left[\frac{2\cdot\bar{\nabla}\cdot M}{\rho'\cdot R}\cdot\left(\frac{P_d(Z)}{T_d} - \frac{P_\infty}{T_\infty}\right)\cdot\frac{\delta Z}{v_d}\right]} \qquad \text{(Equation 3.4)}$$

$$r_d(Z)_{surface} = r_0 - \frac{\alpha\cdot\bar{v}\cdot P_d(Z)\cdot M}{4\cdot\rho'\cdot R\cdot T}\cdot\frac{\delta Z}{v_d} \qquad \text{(Equation 3.5)}$$

where $r_0$ = radius at Z = 0.25 mm, and other terms are defined in Table 3.2. For the temperature-dependent parameters $\nabla$, $l$, and $k$, Davies[81] recommends using the geometric mean of values at the surface and at ambient temperature.

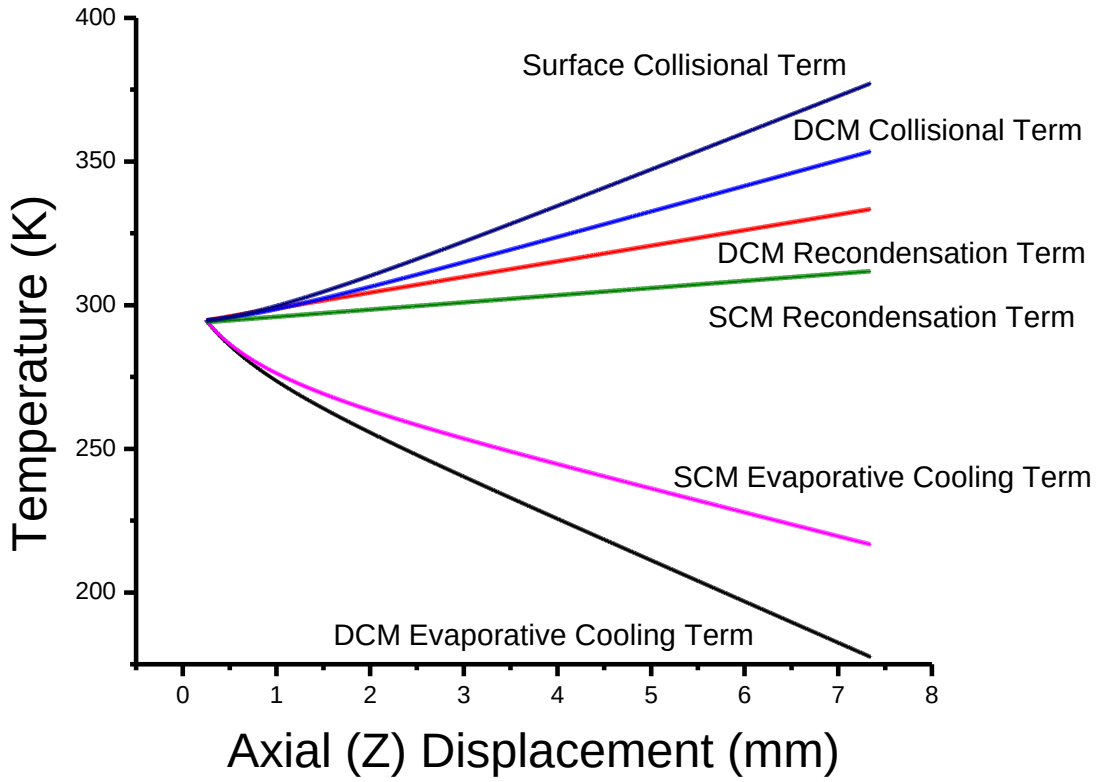


**Figure 3.8**: Comparison of the contributions of evaporative cooling, solvent recondensation, and collisional rewarming for the DCM and SCM**.**

For the diffusion coefficient,$\nabla(T)$, the needed values can be estimated from Equation 3.6:[168]

$$\nabla(T) = \nabla(T_k) \cdot \left[\frac{T}{T_k}\right]^{1.81} \qquad \text{(Equation 3.6)}$$

where $\nabla(T)$ is the diffusion coefficient at temperature $T$, $\nabla(T_k)$ is a known value for $\nabla$ at a specific temperature $T_k$ (0.155 ± 0.012 $cm^2/s$ at 298.15 K for methanol[172]) and 1.81 is an empirical coefficient.[173] Latent heat values can be estimated from Equation 3.7:[169]

$$l(T) = A \cdot \exp(-\alpha \cdot T_r) \cdot (1 - T_r)^{\beta} \qquad \text{(Equation 3.7)}$$

where $l(T)$ is the latent heat at temperature $T$; $A$, $\alpha$, and $\beta$ are unitless solvent-specific empirical coefficients; and $T_r$ is the reduced temperature relative to the critical temperature $T_c$ ($T_r = T/T_c$). For methanol, $T_c$, $A$, $\alpha$, and $\beta$ are 512.6 K, 45.3, -0.3100, and 0.4241, respectively.[169] In the absence of an explicit temperature dependence for the thermal conductivity ($k$), interpolation from tabulations of experimental values[171] was used to estimate the value at a given temperature.

The use of Equation 3.2 and 3.3 requires uniform droplet temperature at any given time. The time required for the surface and interior temperatures of an evaporating droplet to approximately equilibrate (less than a 4% temperature difference between the surface and core of a droplet) can be estimated[81] using Equation 3.8:

$$t_{eq} = \frac{3.9 \cdot r_d^2(Z) \cdot \rho' \cdot s'}{\pi^2 \cdot k'} \qquad \text{(Equation 3.8)}$$

where $k'$ is the (temperature dependent) thermal conductivity of the liquid, and other terms are as defined for Equations 3.2 - 3.5. For methanol at 300 K, k' ~ 0.203 W/m·K and is only weakly temperature dependent.[171] The empirical coefficient 3.9 is calculated from a plot of theory of heat conduction.[81,i] Thus, for methanol droplets of radius between 4 and 40 μm near 300 K, $t_{eq}$ would range from 0.06 to 6 ms, corresponding to flight distances of 0.12 to 12 mm (assuming $v_d$ = 2.0 m/s), similar to the distances in Figure 3.4. This model is limited if droplets do not fully equilibrate since it only takes into account droplet surface temperature. If $t_{eq}$ is not reached, these models will overpredict the overall droplet cooling as the temperature of the droplet core would be warmer.

An iterative solution rather than analytical integration of Equation 3.2 and 3.3 is necessary[81] because of the need to interpolate $k$. For a given set of initial conditions, Equation 3.4 or 3.5 was used to calculate a new $r_d(Z)$ after evaporation over distance $\delta Z$. The new $r_d(Z)$ was used in Equation 3.2 or Equation 3.3 to calculate an incremental change in droplet temperature $\delta T_d$ occurring over the same distance. $\delta T_d$ was then added to $T_{d,0}$ to calculate a new droplet temperature $T_d$. Values for $l$, $k$, $P_d$, and $\nabla$ were updated with respect to the new droplet temperature and the calculation was repeated. Well-defined values (experimentally measured or approximations) exist for all terms in Equation 3.2 - 3.5 except droplet velocity ($v_d$),

---

[i] A typographical error is present in the citation. Equation (19) on page 140 of Reference 81 should read as follows: $\frac{T-T_a}{T_\infty-T_a} = \frac{2a}{\pi r}\sum_{n=1}^{\infty}\left[-\frac{\cos(n\pi)}{n}\cdot\exp(-\frac{n^2\pi^2K't}{a^2})\cdot\sin\left(\frac{n\pi r}{a}\right)\right]$. Note that the variable assignments in this reference may be different from those assigned in this dissertation.

initial droplet radius ($r_0$), and $P_\infty$. In the DCM, $v_d$ and $r_d(Z)$ appear only as a product, and thus are considered inseparable, reducing the number of potential fitting parameters from three ($r_0$, $v_d$, and $P_\infty$) for the SCM to two ($r_0^2 \cdot v_d$ and $P_\infty$) for the DCM.

To test the models with no fitting parameters, the following initial values were used to model the temperature evolution at $F$ = 25 μL/min: $r_0 = r_c$ = 0.10 μm; $v_d$ = 2.0 m/s; $T_{d,0}$ = 294.7 K (*i.e.* the initial experimental temperature measured at 0.25 mm); and $P_\infty$ fixed at the value calculated from the mole ratio of gas and liquid flow rates (*e.g.*, 8 Torr at $F$ = 25.0 μL/min; see Section 3.2.2). These parameters resulted in a prediction (Figure 3.9) of cooling by ~20 K in ~0.6 μm in the DCM and heating by ~8 K in ~2 μm in the SCM, regardless of flow rate. For either model, there was no further change in temperature after 2 μm (~1 μs assuming $v_d$ = 2 m/s). Pearson correlation coefficients ($R$) were -0.7 and 0.7 for the SCM and DCM, respectively ($R$ =1 is a total positive correlation; -1 is a total negative correlation). The models using these initial parameter values clearly do not resemble any data displayed in Figure 3.3.

In contrast, Figure 3.10 shows the fits obtained at each flow rate when the parameters are allowed to vary. Both models fit the data well ($R$ = 0.998; Table 3.3), and the two model curves are in fact indistinguishable. For DCM fits, $P_\infty$ was observed to be the sole fitting parameter affecting final $T_d$ (*i.e.* $T_f$ in Table 3.2), whereas the product $r_0^2 \cdot v_d$ determined the initial cooling rate.

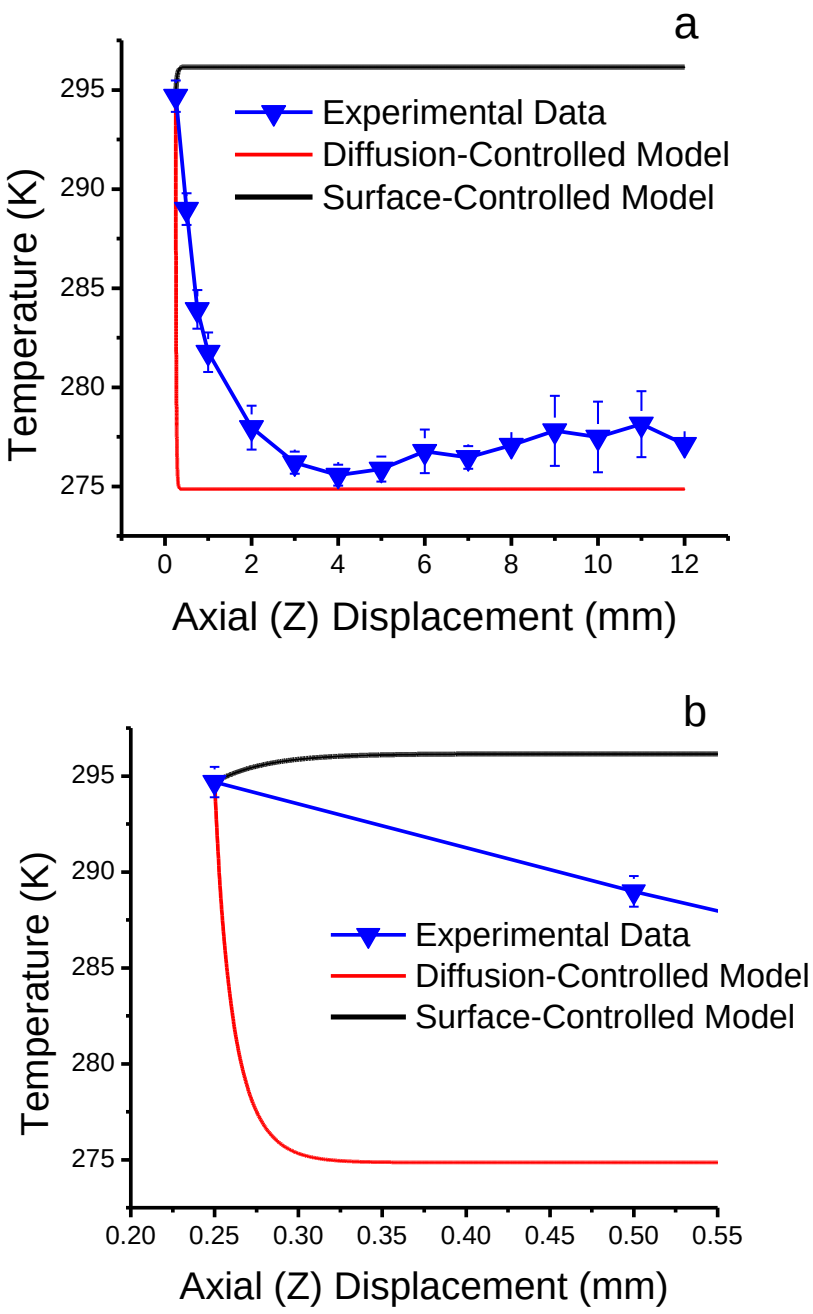


**Figure 3.9:** Comparison of $F$ = 25 µL/min experimental data to model with fixed parameters. Figure 3.11b is zoomed in to display initial temperature detail.

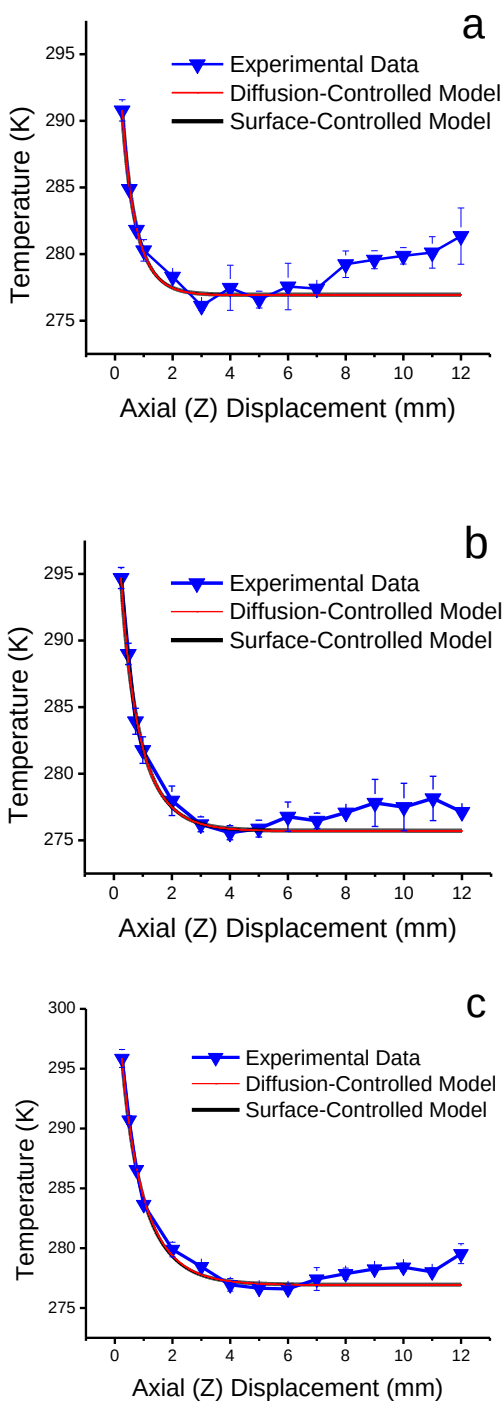


**Figure 3.10:** Comparison of experimental data and optimized model at a) $F$ = 12.5 µL/min, b) $F$ = 25 µL/min, and c) $F$ = 50 µL/min. Curves for the diffusion-controlled and surface-controlled models are indistinguishable for all flow rates.

**Table 3.3**: Experimental and calculated parameter values for surface-controlled and diffusion-controlled models of droplet cooling.

| Parameter | Surface-Controlled Model (SCM) | | | Diffusion-Controlled Model (DCM) | | |
|---|---|---|---|---|---|---|
| Solvent Flow Rate ($F$; µL/min)[1] | 12.5 | 25.0 | 50.0 | 12.5 | 25.0 | 50.0 |
| Emission Current ($I$; µA)[1] | 0.055 | 0.12 | 0.19 | 0.055 | 0.12 | 0.19 |
| Methanol Partial Pressure ($P_\infty$; Torr)[2] | 12.9 ± 1.3 | 12.6 ± 0.9 | 20.0 ± 0.6 | 19.5 ± 1.2 | 15.7 ± 1.3 | 19.5 ± 0.6 |
| Droplet Velocity ($v_d$; m/s)[3] | 0.52 ± 0.05 | 0.60 ± 0.05 | 0.63 ± 0.03 | 2.0 | 2.0 | 2.0 |
| Droplet Radius ($r_d(Z)$; µm) at Z = 0[4] | 11.9 ± 0.6 | 13.5 ± 0.8 | 15.5 ± 0.4 | 6.7 ± 0.3 | 7.9 ± 0.3 | 8.8 ± 0.1 |
| Droplet Radius ($r_0$; µm) at Z = 0.25[2] | 11.7 ± 0.6 | 13.4 ± 0.8 | 15.4 ± 0.5 | 6.7 ± 0.3 | 7.8 ± 0.3 | 8.7 ± 0.1 |
| Droplet Radius ($r_d(Z)$; µm) at Z = 5[4] | 10.9 ± 0.6 | 12.6 ± 0.8 | 14.5 ± 0.4 | 6.4 ± 0.3 | 7.5 ± 0.3 | 8. 5 ± 0.1 |
| Droplet Radius ($r_d(Z)$; µm) at Z = 12[4] | 9.7 ± 0.6 | 11.6 ± 0.8 | 13.5 ± 0.4 | 6.0 ± 0.3 | 7.1 ± 0.3 | 8.2 ± 0.1 |
| Droplet Temperature ($T_d$; K) at Z = 0[4] | 302.0 ± 0.8 | 306.7 ± 0.8 | 305.3 ± 0.8 | 302.7 ± 0.8 | 306.7 ± 0.8 | 305.1 ± 0.8 |
| Droplet Temperature ($T_{d,0}$; K) at Z = 0.25[1] | 290.8 ± 0.8 | 294.7 ± 0.8 | 295.9 ± 0.8 | 290.8 ± 0.8 | 294.7 ± 0.8 | 295.9 ± 0.8 |
| Droplet Temperature ($T_f$; K) at Z = 12[4] | 276.9 ± 0.8 | 275.7 ± 0.8 | 277.0 ± 0.8 | 276.9 ± 0.8 | 275.7 ± 0.8 | 277.0 ± 0.8 |
| ΔT (K) (Z = 0.25 to 12 mm)[4] | 13.9 | 19.0 | 18.9 | 13.9 | 19.0 | 18.9 |
| ΔT (K) (Z = 0 to 12 mm)[4] | 25 | 31 | 28 | 26 | 31 | 28 |
| Pearson Correlation Coefficient ($R$)[5] | 0.994 | 0.998 | 0.998 | 0.994 | 0.998 | 0.998 |
| Pooled Standard Deviation[5] | 0.76 | 0.83 | 0.35 | 0.76 | 0.83 | 0.35 |

[1]Experimental measurement

[2]Fitting parameter

[3]Fitting parameter for SCM; fixed value for DCM (see text)

[4]Calculated from model

[5]For fit of model to the experimental data between Z = 0.25 and 5.0

In the SCM fits, effects of $P_\infty$, $r_0^2$, and $v_d$ are convoluted, each affecting $T_f$ and the initial rate of cooling. It is instructive to consider in detail the resulting values of the two (DCM) or three (SCM) fitting parameters and their dependence on flow rate.

The results at 25 μL/min were considered first. Fitted $P_\infty$ values (12.6 and 15.7 Torr for SCM and DCM, respectively) are reasonable, but are higher than the 8 Torr value predicted from the flow rate ratio and an assumed total ambient pressure of 760 Torr. The differences are more than can be ascribed to uncertainty in the ambient temperature, ($T_\infty$ = 303 ± 1 K; see Table 3.3). They may be partly ascribable to the fact that the pressure is higher in the purged enclosure due to the constant nebulizing gas flow; other possibilities may include methanol adsorbed or pooled in the purged enclosure.

The SCM fitted value of $v_d$ was 0.60 m/s, somewhat lower than reported values[51] (~2.0 m/s) under similar – though not identical – conditions, but reasonable. However, the SCM fitted value for $r_0$ (13.4 μm), while reasonable for droplets undergoing diffusion-controlled evaporation, is not a reasonable droplet size for surface-controlled evaporation due to the value being two orders of magnitude above $r_c$. In the DCM, $r_d(Z)$ and $v_d$ are inseparable, as noted above; the product $r_0^2 \cdot v_d$ was optimized to $1.2 \times 10^{-10}$ $m^3/s$. If $r_0$ is set to $r_c$ (0.10 μm), $v_d$ = 12 km/s, a value 3-4 orders of magnitude higher than reported droplet velocities.[51] If instead, $v_d$ is set equal to 0.6 m/s (value obtained from the SCM fit), the DCM optimum $r_0$ = 14 μm, which is within the expected range of radii. Using a literature value[51] for $v_d$ (2.0 m/s) gives $r_0$ = 7.8 μm, also a reasonable value.[51,60] In the

absence of a direct measurement of $v_d$, a value of 2.0 m/s was used to derive radius estimates for the DCM fits in Table 3.3.

Radii determined for the optimized fit for both models (see Table 3.3) are reasonable based on literature values,[51,60] but they are each more than two orders of magnitude greater than the critical radius. Radius calculations (Equation 3.4 and 3.5) over the modeling period Z = 0.25 – 12 mm predict that droplets shrink ≤ 18% for the SCM and ≤ 10% (assuming $v_d$ = 2.0 m/s) for the DCM, indicating that droplet sizes do not approach $r_c$. Because the SCM should apply only when $r_d(Z) < r_c$, the DCM better describes these data based on the derived values of $r_d(Z)$. Note that the small offspring droplets[60] formed during this period are not considered. They are expected to comprise a small fraction of the total spray mass, regardless of solvent.[60] Estimates of the parent mass loss due to progeny droplets vary- between 0.3% of a parent droplet's mass lost per 100 progeny droplets[51,94], 2% for 20 progeny droplets[76], and up to 5% in other studies[60,97]), so their contribution to the signal should be small.

Using the optimized $r_0$ values, the hypothesis of uniform droplet temperature (Equation 3.8) can be revisited. For the DCM, $r_d(Z) \leq 8.8$ μm (assuming $v_d$ = 2.0 m/s) so that $t_{eq} \leq 0.30$ ms. By comparison, transit time between experimental points 0.25 mm apart is 0.13 ms at this velocity. This suggests that temperature equilibration is approached but may not be fully realized in the DCM. For the SCM $r_d(Z) \leq 15.5$ μm, requiring $t_{eq} \leq 0.93$ ms; transit time for $\delta Z$ = 0.25 mm is 0.43 ms (based on $v_d$ = 0.58 m/s, the average across all flow rates). Again, the transit time is somewhat shorter

than $t_{eq}$ in the SCM. While this introduces some uncertainty to modeling axial temperatures from 0 to 1 mm, the quality of the fits suggests that the effect is not large.

If the droplet does not have enough time to equilibrate between data points, the center of the droplet would possess a higher temperature than the surface. Experimental measurements would weigh warmer than modeled temperatures as the model only accounts for the temperature at the surface. Evaporation would be slower than the modeled prediction if there were insufficient equilibration time. In the DCM, this would affect $P_\infty$ as it was the only parameter observed to have any effect on the final temperature, $T_f$. Insufficient equilibration time would have a more complicated effect in the SCM, as $P_\infty$, $r_0^2$, and $v_d$ are convoluted, each affecting $T_f$ and the initial rate of cooling. The model does not resemble Figure 3.9 for either model, providing confidence that this effect is not large.

Next, the trends in the fitting parameters at different $F$ can be considered. The increase in fitted droplet size ($r_0$) at higher $F$ (by ~30% from 12.5 to 50 μL/min in either model) is consistent with the charge density arguments[92] discussed above. Although there is a statistically significant increase of $v_d$ with $F$ in the SCM, it is small (from 0.52 ± 0.05 to 0.63 ± 0.03 m/s; see Table 3.1) suggesting that the assumption of constant $v_d$ in the DCM is reasonable. Note that the direct proportionality between $F$ and $v_d$ predicted by the SCM runs counter to the predicted effects of acceleration by the electric field and by the collision gas. Thus, although $v_F$ is a relatively small contributor to $v_d$ (just 0.42 cm/s at $F$ =12.5 μL/min), it is the only factor expected to

increase with $F$; its four-fold increase ($F$ increases from 12.5 to 50.0 μL/min) evidently outweighs acceleration decreases at higher $F$.

Trends in pressure appear to be more complex. Methanol partial pressure ($P_\infty$) in the continuously purged enclosure should increase roughly linearly with $F$. For both models, the fit values of $P_\infty$ increase as $F$ increases from 25 to 50 μL/min, though less than doubling. In both models, the fit value of $P_\infty$ at 12.5 μL/min seems anomalously high. Close inspection of Figure 3.4 reveals a possible cause. The onset of rewarming for $F$ = 12.5 μL/min occurs at smaller Z (~3 mm compared to ~5 mm at other $F$). This may result from the smaller droplet size at lower $F$, the resulting lower heat capacity, and the fact that droplets are cooler at low $F$ for the first few Z positions (i.e. larger thermal gradient at small Z). These effects may be reinforced by a longer interaction time at a given Z (if $v_d$ is smaller, as predicted by the SCM). While rewarming is not considered by the present models, it can affect the fits. As noted above $P_\infty$ strongly impacts the predicted $T_f$, especially in the DCM. Conversely, the rewarming evident at Z = 3 mm in the experimental data for $F$ = 12.5 μL/min can be expected to inflate the value of $P_\infty$ derived from the fit. The effect is greater in the DCM, consistent with the observation that the impact of $P_\infty$ on $T_f$ is moderated in the SCM by the influence of $v_d$ and $r_0$. Hence, the inflated $T_\infty$ at 12.5 μL/min may be an artifact of reheating not accounted for in the models.

Finally, it is interesting to consider the total amount of cooling. The solution passes through the source tee (~329 K) and the capillary before emission. The surface temperature of the outer capillary fell from ~323 K close to the tee to ~318

K near the emitter tip. Back-extrapolation of spray data to Z = 0 mm (the position where droplets form) predicts an initial $T_d$ between 302 and 307 K depending on $F$ (Table 3.2), all reasonable values. The lower extrapolated $T_d$ at $F$ = 12.5 μL/min (Table 3.2) is counterintuitive; there should be more time for thermal equilibration within the capillary at lower flow. This may be offset by the faster cooling (evident from the steeper slope between Z = 0 and ~2 mm; Figure 3.4) and resultant uncertainty in extrapolation, although this is not evident from the uncertainties estimated from propagation of errors (see Table 3.2).

### 3.2.5 Direct Comparison with Kebarle's Model

Kebarle and Tang modeled[50] the change in radius and charge with time (see Section 1.2.4) using the SCM. They estimate a residue droplet decreases in radius from 1.5 to ~0.75 μm (~50%) in ~600 μs (calculated with Equation 3.5) with a reduction in charge from ~8.4 to ~5.0 fC per droplet (calculated via Equation 1.4) due to three Coulombic explosions they predict occur during that timeframe (a ~40% reduction in charge). The slope of the radial decrease over time in Kebarle's model is ~-0.00125 μm/μs.

Radii values calculated in the present study 11.7 to 15.4 μm in the SCM (DCM model is not comparable) - an order of magnitude larger than Kebarle's radii value. Differences in constants between Kebarle's study and the president study include: 1) the use of the condensation coefficient, α, of 0.04 in Kebarle's study versus 0.9 in the present, 2) assumption of constant droplet vapor pressure, 3) assumption of

constant droplet temperature. If α (only present in the SCM) is replaced with Kebarle's 0.04, the fit at $F$ = 25 μL/min yields unrealistic values for the fitting parameters when compared with current studies discussed previously: $v_0$ = 1.0 ***mm/s***, $p_a$ = 8.4 Torr, and $r_0$ = 0.31 ***mm*** (Pearson correlation coefficient = 0.992- an approximately equal fit to those discussed previously). The radius value is extremely unlikely and the conclusion must be made that Kebarle's assumed diffusion coefficient is likely too small. Fixed temperature, (and thus vapor pressure) cannot be a correct conclusion based on experimental data discussed previously.

### 3.2.6 Evaluation of Potential Artifacts

As discussed in Section 3.1.2, there are various sources of error to consider in these experiments: 1) significant change in dye concentration and pH changes due to droplet evaporation, 2) cross-absorption from the overlap of the absorption band of RhB with the emission band of Rh110, and 3) preferential ion emission of one dye over the another due in part to differences in surface activity. These are now each considered.

Possible cross-absorption effects were probed by a cell-shift experiment,[162] whereby the excitation laser was focused at different depths within a conventional cuvette by translating a cuvette about the beam waist of the laser (X-axis; Figure 3.11).

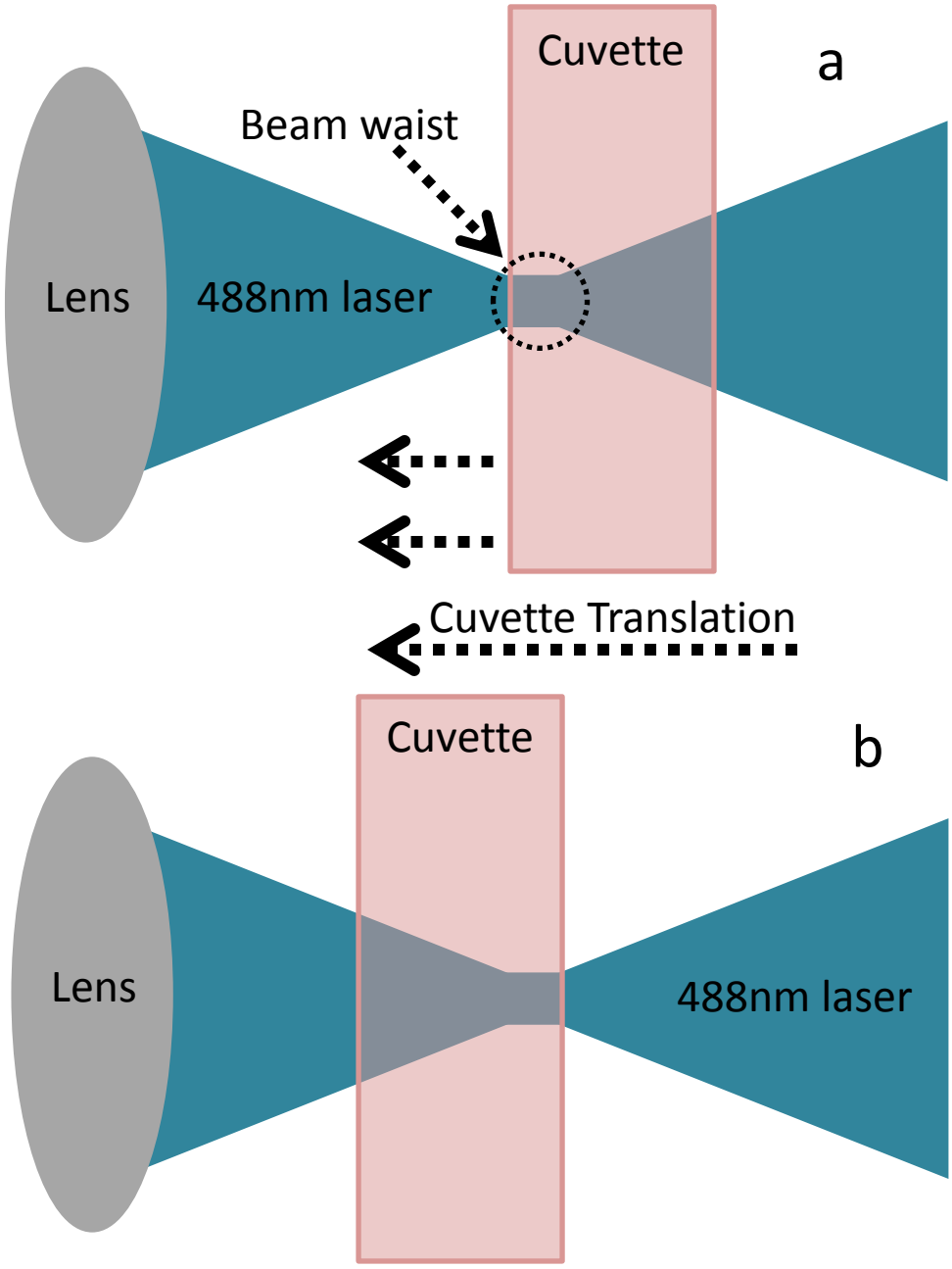


**Figure 3.11:** Diagram displaying a cell-shift experiment: the analysis of a sample at two different depths (a- front face; b- back face) within a cuvette.

In addition to the typical dye concentrations (5.0 μM RhB and 0.50 μM Rh110;), solutions with dye concentrations 10% (5.5 μM RhB/0.55 μM RhB) and 25% (6.25 μM RhB/0.625 μM RhB) higher were also analyzed; results are displayed in Figure 3.12. In order to ascertain the X-axis position where the laser focus first interacts with the front face of the cuvette, the cuvette was placed ~5 to 10 mm away from the laser focus and translated towards the focus in 1 mm increments. The spatial location of the first data point (X = 0) was acquired approximately 2 mm As expected for cross-absorption, the fluorescence ratio (I[RhB]/I[Rh110]) increased as the laser focus moved through the cuvette face into the bulk solution. An accompanying shift in emission ($\lambda_{max,\ RhB}$) increased the separation between the emission maxima of the two dyes ($\Delta\lambda_{max}$) from 45.1 ± 0.5 nm at the front face of the cuvette to 51.5 ± 0.5 nm at the back face (Figure 3.13). The change in $\Delta\lambda_{max}$ is more pronounced at concentrations higher than the 5.0/0.5 μM RhB/Rh110 standard, although there is no discernible concentration effect on $\Delta\lambda_{max}$ at the front face. $\Delta\lambda_{max}$ for the spray plume data (evident in Figure 3.3) is ~45 nm, suggesting a short and roughly fixed equivalent pathlength and validating the use of the short-path (near-front-face) calibration data. It is also expected that an effect such as cross-absorption may be expected to diminish as Z increases due to the diminishing number density of droplets as the spray conically expands – potentially a larger concentration change effect than that due to droplet shrinkage.

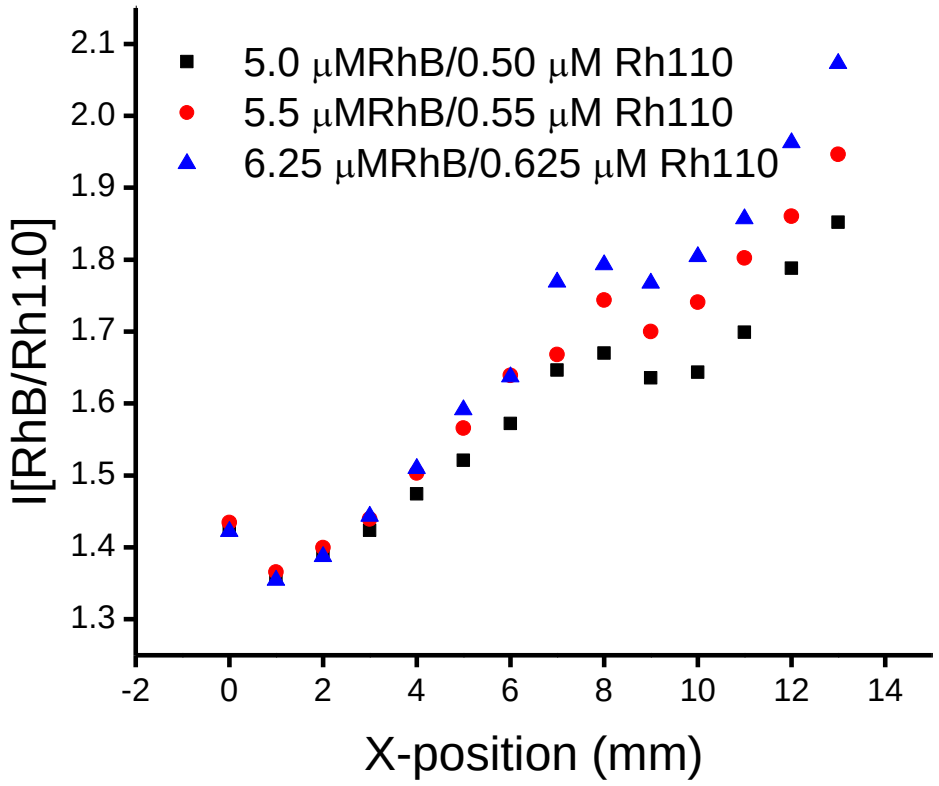


**Figure 3.12**: Cell shift profiles illustrating the change in ratio of the two dyes as a function of laser focus depth at three different solution concentrations.

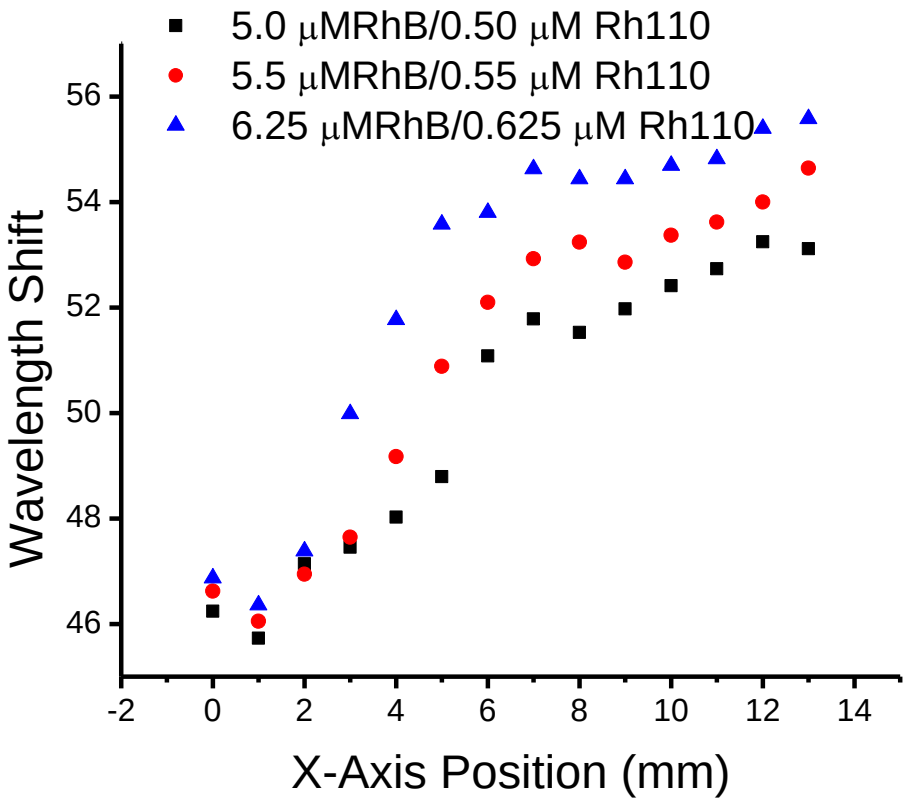


**Figure 3.13:** Cell shift profiles illustrating the separation of emission maxima of the two dyes as a function of cuvette depth at three different solution concentrations.

Chamarthy[160] studied the effect concentration change had on the RhB/Rh110 emission ratio. They subjected a solution of the dye pair ([RhB] ≈ 2.1 to 21 μM; [Rh110] ≈ 2.7 to 27 μM) to temperature changes from ~293 K to ~343 K, resulting in the dye emission ratio increasing as little as 55% and as much as 100%, However, the concentrations used in this study ranged from 10 to up to ~50 times higher than those used herein. In contrast, the modeling described above predicts much more modest concentration increases. A volumetric decrease was calculated by using modelled radii presented in Table 3.3 and results in concentration increases on the order of 10-30% due to droplet shrinkage caused by solvent evaporation in the first (modeled) 5 mm of the spray. Temperature calibration curves obtained from methanolic dye solutions at concentrations up to 25% higher than those of our standard mixture showed changes in fluorescence intensity ratios equivalent to only a ~0.4 K temperature difference, well within the experimental error displayed in Figure 3.4. We conclude that changes in dye concentration due to droplet evaporation have a negligible effect on the temperature calibration over the modeled region.

Another effect of droplet evaporation, changes in pH, occurs in conjunction with the basic electrochemistry associated with the ES process. Based on data from Table 3.1, the effect should be greatest for the lowest flow rate; an increase in $[H^+]$ by about 3.0 μM can be estimated from the current at $F$ = 12.5 μL/min. Based on the evaporative radius change reported in Table 3.3, a further increase in excess $[H^+]$ to approximately 3.5 μM can be ascribed to evaporation. Calibration curves obtained

from a solution acidified to 5 μM formic acid provided temperature estimates within about ± 1.7 K of those obtained without added acid. Acidification effects on the dye ratio are also small compared to the overall temperature change.

Finally, fluorescence intensity ratios may be impacted by the preferential ion emission of one dye over the other due to differences in surface activity. This possibility was probed by comparing ion signals observed in the electrospray mass spectrum of the original 10:1 fluorescent dye spray mixture (5.0 μM RhB to 0.50 μM Rh110). The signal for the molecular cation of RhB (m/z 443) was ~30 times higher than that for Rh110 (m/z 331), three times higher than the concentration ratio in the solution (Figure 3.14). This apparent preferential desorption of RhB is consistent with its methylated structure, resulting in higher surface activity relative to Rh110 and potential enrichment[143] at the droplet surface. Preferential desorption would tend to reduce RhB concentration and thus the dye fluorescence intensity ratio, resulting in overestimation of the spray temperature $T_d$. Ion emission tends to occur later in the spray process[60] (*i.e.*, at higher Z), so overestimation would be greatest at higher Z; droplet cooling may therefore be even more extensive than evident from Figure 3.4. Preferential emission of RhB may also contribute to the apparent rewarming at positions > 5 mm.

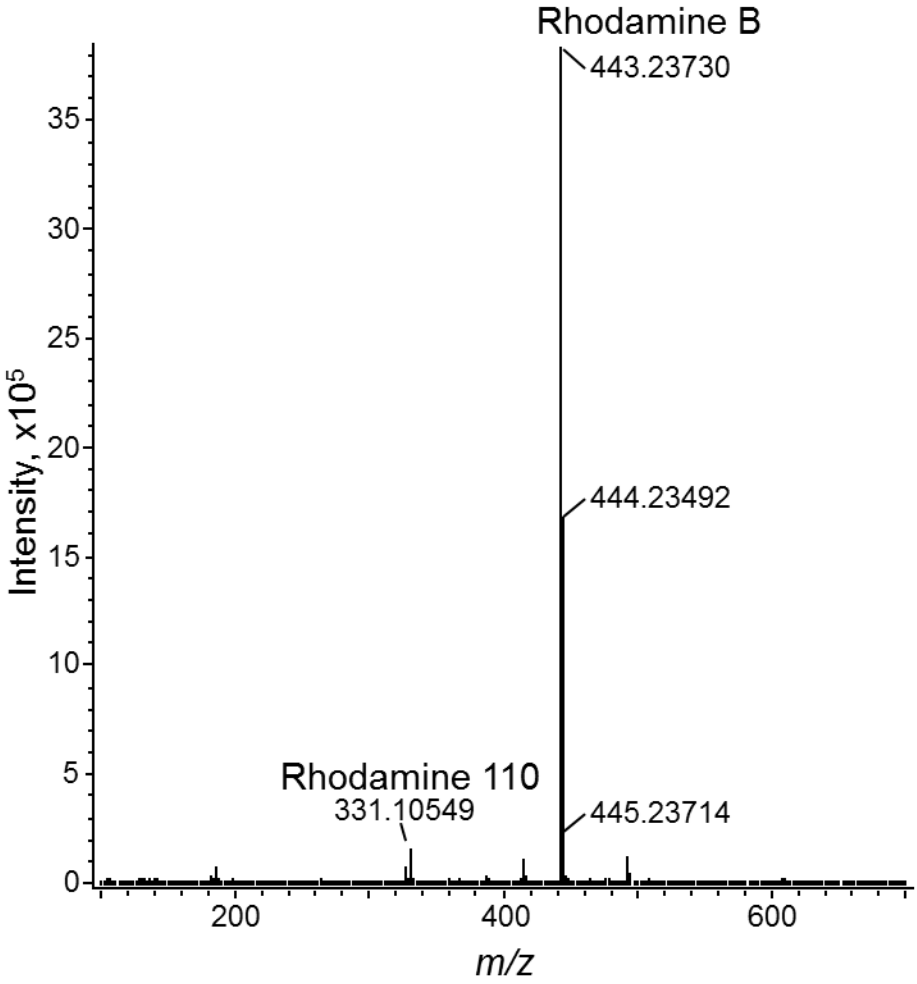


**Figure 3.14:** Spectrum of a 0.5 μM/0.05 μM Rhodamine B/Rhodamine 110 mixture.

Further corroboration of the minimal impact of these artifacts comes from the observation that the measured fluorescence intensity ratios (and the derived temperature) at the plateaus in the axial profiles (Z = 3 – 6 mm in Figure 3.4) are similar for all three flow rates despite differences in modeled droplet sizes and (presumably) dye and proton concentrations. Additionally, the largest measured temperature changes occur over regions (Z = 0.25 – 1.0 mm) where there is a relatively small change in droplet radii, providing additional confidence in calibrations.

### 3.2.7 Conclusions

The total temperature change predicted by these models is up to 30 K. This degree of cooling is not account for solely from the 8 K change calculated by Tang and Kebarle,[50] but should provide a better estimate of the total temperature excursion to which ES solutes may be subjected. Both the SCM and DCM models fit the experimental data very well and yield reasonable values for $P_\infty$ and $v_d$ (or $r_0^2 \cdot v_d$ for the DCM). The value of $r_0$ needed to fit these data with the SCM far exceeds the critical radius, $r_c$, contrary to the conditions for evaporation to be surface-controlled. This suggests that evaporation in the region sampled in this experiment is diffusion-controlled. This conclusion would be further strengthened by independent experimental measurement of droplet velocity and radius – beyond the scope of the current study. Regardless of model, the amplitude of ΔT is clearly large

enough to significantly impact some chemical equilibria if the kinetics are fast enough for changes on the timescale of the droplet lifetime.

# Chapter 4. Ionization Mechanism of Positive-Ion Direct Analysis in Real Time: A Transient Microenvironment Concept

## 4.1 Introduction

The Direct Analysis in Real Time (DART) ion source was introduced in 2005 by Cody[18] and immediately demonstrated success in the analysis of samples in their native forms. Applications such as analyzing perfumery raw materials deposited on smelling strips,[147] counterfeit Cialis tablets,[148] strobilurin fungicides in the ethyl acetate extract of wheat,[149] fatty acid methyl esters from bacterial whole cells[150] self-assembled monolayers of dodecanethiol on gold surfaces[151], taxoids from cell cultures of *Taxus wallichiana*,[152] alkaloids from the intact hairy roots of *Atropa acuminate*,[153] and cuticular hydrocarbons from an awake-behaving fly[154] are demonstrations of the robust and versatile nature of this ion source.

The DART mechanism offered by Cody[18,128] suggests the main pathway for analyte ionization (described in full in Section 1.3.2). Briefly, an in-source corona discharge excites the source gas, typically helium. In the positive-ion mode, the excited source gas exits the source and immediately collides with atmospheric water vapor to form protonated water dimers. Thermal electrons present in the excited source gas are assumed to react with atmospheric oxygen molecules in an electron-capture mechanism to form molecular oxygen anions, $O_2^{-\bullet}$. In the model of Cody, these atmospheric ions then collide directly with gaseous analyte ions, forming cationic and anionic analyte ions, respectively. However, this model does not account for ion suppression effects created by the use of "unfavorable" DART solvents, such as dimethyl sulfoxide.[141] To explore these effects, analytes with low

proton affinity were selected in order to assess their ion abundances in a selection of 25 different solvents that include proton acceptors, benzene derivatives, alkanes, and chlorinated methanes. To contrast, solid analytes were also analyzed to compare with their solvated forms.

## 4.2 Results and Discussion

### 4.2.1 Initial Solvent Characterization

In order to understand the adduct formation patterns of analytes, it would be useful to first analyze the adduct formation patterns for four classes of solvents: proton acceptors, benzene derivatives, alkanes, and chlorinated methanes. All the following solvents are listed in order of increasing PA. The proton acceptor solvents analyzed were methanol (MeOH), ethanol (EtOH), acetonitrile (ACN), 2-propanol, acetone, tetrahydrofuran (THF), ethylacetate (EtAc), *N*,*N*-dimethylformamide (DMF), and dimethylsulfoxide (DMSO). The benzene-derivative solvents analyzed were hexafluorobenzene ($C_6F_6$), benzene, chlorobenzene (PhCl), flourobenzene (PhF), toluene ($PhCl_3$), ethylbenzene ($PhC_2H_5$), *p*-xylene, *o*-xylene, and anisole. The alkane solvents analyzed were hexanes, heptane, iso-octane, and cyclohexane. The chlorinated methanes analyzed were methylene chloride ($CH_2Cl_2$), and chloroform ($CHCl_3$). Approximately 1 μL of each individual solvent was analyzed. The relative intensities of all ions formed as a result are displayed in Table 4.1.

Henceforth, pure solvent and analyte molecules will be denoted as “S” and “M,” respectively.

**Table 4.1**: Observed ion peaks with relative intensity over 5% in the DART mass spectra[a].

| | | Relative Intensity (%) of Ions Formed | | | | Other ions detected (relative intensity) |
|---|---|---|---|---|---|---|
| | **Solvent** | $[S - H]^+$ | $S^{+\bullet}$ | $[S + H]^+$ | $[S_2 + H]^+$ | |
| **Proton Acceptors** | methanol | | | 72 | 100 | $[S_2 + H - H_2O]^+$; 15% |
| | ethanol | | | 74 | 100 | $[S_2 + H - H_2O]^+$; 16% |
| | acetonitrile | | | 100 | 63 | |
| | 2-propanol | | | 14 | 100 | $[S_2 + H - H_2O]^+$; 16% |
| | acetone | | | 90 | 100 | |
| | tetrahydrofuran | | | 46 | 100 | |
| | ethyl acetate | | | 31 | 100 | |
| | N,N-dimethylformamide | | | | 100 | |
| | dimethylsulfoxide | | | | 100 | |
| | **Solvent** | $[S - H]^+$ | $S^{+\cdot}$ | $[S + H]^+$ | $[S_2 + H]^+$ | |
| **Benzene derivatives** | hexafluorobenzene | | 90 | | | $[S - F + OH]^+$; 68% |
| | benzene | | 100 | 30 | | |
| | chlorobenzene | | 100 | 18 | | |
| | fluorobenzene | | 100 | 39 | | $[S - F + OH]^+$; 63%<br>$[S - F + H_2O]$+; 11%<br>$[2S - 2F + H_2O]^+$, 14% |
| | toluene | | 72 | 100 | | |
| | ethyl benzene | | 34 | 100 | | |
| | *p*-xylene | | 26 | 100 | | |
| | *o*-xylene | | 49 | 100 | | |
| | anisole | | 14 | 100 | | |

[a]Contribution from the isotopic peak of [m/z – 1] was subtracted.
[b]15-100 ppm amylene or 40-100 ppm cyclohexane is present as a preservative.
[c]50 ppm pentene is present as a preservative.
[d]0.75% ethanol is present as a preservative.

**Table 4.1 Continued:** Observed ion peaks with relative intensity over 5% in the DART mass spectra[a].

| | | Relative Intensity (%) of Ions Formed | | | | Other ions detected (relative intensity) |
|---|---|---|---|---|---|---|
| | **Solvent** | $[S - H]^+$ | $S^{+\cdot}$ | $[S + H]^+$ | $[S_2 + H]^+$ | |
| **Alkanes** | hexanes | | 100 | | | $C_4H_9^+$, 11% $C_5H_{11}^+$, 10% $[S - 4H]^+$, 11% $[S - 3H]^+$, 62% $[S - 2H]^+$, 15% |
| | heptane | | 11 | | | $C_4H_9^+$, 100% $C_5H_9^+$, 14% $C_5H_{11}^+$, 52% $[S - 3H]^+$, 25% $[S - 2H]^+$, 4% |
| | iso-octane | | | | | $C_4H_9^+$, 100% |
| | cyclohexane | | 100 | | | |
| | **Solvent** | $[S - H]^+$ | $S^{+\cdot}$ | $[S + H]^+$ | $[S_2 + H]^+$ | |
| **Chlorinated methanes** | methylene chloride[b] | | | | | $C_3H_7^+$, 7% $C_4H_7^+$, 6% $C_5H_{11}^+$, 60% $CHCl_2^+$, 9% |
| | chloroform[c] | | | | | $C_3H_7^+$, 11% $C_5H_9^+$, 26% $C_5H_{11}^+$, 100% $CHCl_2^+$, 45% $C_6H_{11}^+$, 12% $CCl_3^+$, 2% $C_6H_{11}Cl^+$, 11% |
| | chloroform[d] | | | | | $[C_2H_5OH + H]^+$, 100% $[(C_2H_5OH)_2 + H]^+$, 46% $CHCl_2^+$, 5% |

[a]Contribution from the isotopic peak of [m/z – 1] was subtracted.
[b]15-100 ppm amylene or 40-100 ppm cyclohexane is present as a preservative.
[c]50 ppm pentene is present as a preservative.
[d]0.75% ethanol is present as a preservative.

The spectra of all studied proton acceptor solvents display protonated dimers ($[S_2 + H]^+$); all display monomers ($[S + H]^+$) except DMF and DMSO (explained below). Since all solvents in this category possess IE values (see Table 4.2) less than the metastable energy of helium (19.8 eV), all S should be ionized via Mechanism 4.1:

$$He^* + S \longrightarrow He + S^{+\bullet} + e^- \text{ , where ME(He) > IE (S)} \quad \text{(Mechanism 4.1)}$$

Note that Mechanism 4.1 is a slight variation of Equation 1.11, specifying S (used heavily in discussion in this Chapter) instead of the more generic M. Since PA values (Table 4.3; see discussion in Appendix Section A-1 for discussion concerning estimation of some PA values) for all [S + H] in this category are greater than that of their $[S - H]^\bullet$ formed in Mechanism 4.1, the radical will react with S to form $[S + H]^+$ ions:

$$S^{+\bullet} + S_n \longrightarrow [S - H]^\bullet + [S_n + H]^+ \text{ , where } PA(S_n) > PA(S - H) \quad \text{(Mechanism 4.2)}$$

These solvents form clusters (mostly dimers), which possess PA values stronger than the corresponding monomers. These probably form via Mechanism 4.1 (creation of an $S^{+\bullet}$ ion), 4.2 (reaction of an $S^{+\bullet}$ ion with $[S_1 + H]^+$), or Mechanism 4.3:

$$[(H_2O)_m + H]^+ + S_n \longrightarrow (H_2O)_m + (S_n + H)^+ \text{ ,}$$

$$\text{where } PA(S_n) > PA(H_2O) \quad \text{(Mechanism 4.3)}$$

since the PA of all S and $S_2$ are greater than $PA(H_2O)$. The general preponderance of solvent dimers over solvent monomers is expected since all $PA(S_2) > PA(S)$. The lack of DMF and DSMO S ions may be accounted for by the extremely high dimer PA value- all $[S + H]^+$ ions are converted to $[S_2 + H]^+$.

**Table 4.2:** Abbreviations, molecular formulae, isotopic masses, boiling points (BP) and ionization energies[a] (IE) for studied solvents.

| Solvent | Common Abbreviation | Formula | Isotopic mass | BP ($^{o}$C) | IE (eV) |
|---|---|---|---|---|---|
| water | water | $H_2O$ | 18.011 | 100 | 12.62 |
| acetonitrile | MeCN | $CH_3CN$ | 41.027 | 82 | 12.2 |
| chloroform | $CHCl_3$ | $CHCl_3$ | 117.914 | 61 | 11.37 |
| methylene chloride | $CH_2Cl_2$ | $CH_2Cl_2$ | 83.953 | 40 | 11.33 |
| methanol | MeOH | $CH_3OH$ | 32.026 | 65 | 10.84 |
| ethanol | EtOH | $C_2H_5OH$ | 46.042 | 78 | 10.5 |
| 2-propanol | *i*-PrOH | $(CH_3)_2CHOH$ | 60.058 | 82 | 10.17 |
| hexanes | Hex | $C_6H_{14}$ | 86.11 | 69 | 10.13 |
| ethylacetate | EtAc | $CH_3COOC_2H_5$ | 88.052 | 77 | 10.01 |
| heptane | Hep | $C_7H_{16}$ | 100.125 | 98 | 9.93 |
| hexafluorobezene | $C_6F_6$ | $C_6F_6$ | 185.99 | 81 | 9.9 |
| iso-octane | IsoOct | $C_8H_{18}$ | 114.141 | 99 | 9.89 |
| cyclohexane | CyHex | $C_6H_{12}$ | 84.094 | 81 | 9.88 |
| acetone | Acetone | $CH_3COCH_3$ | 58.042 | 56 | 9.7 |
| tetrahydrofuran | THF | $C_4H_8O$ | 72.058 | 66 | 9.4 |
| benzene | Benzene | $C_6H_6$ | 78.047 | 80 | 9.24 |
| fluorobenzene | PhF | $C_6H_5F$ | 96.038 | 85 | 9.2 |
| *N*,*N*-dimethylformamide | DMF | $HCON(CH_3)_2$ | 73.053 | 153 | 9.13 |
| dimethylsulfoxide | DMSO | $CH_3SOCH_3$ | 78.014 | 189 | 9.1 |
| chlorobenzene | PhCl | $C_6H_5Cl$ | 112.008 | 132 | 9.07 |
| toluene | $PhCl_3$ | $C_6H_5CH_3$ | 92.063 | 111 | 8.83 |
| ethylbenzene | $PhC_2H_5$ | $C_6H_5C_2H_5$ | 106.078 | 136 | 8.77 |
| *o*-xylene | *o*-xylene | $C_6H_4(CH_3)_2$ | 106.078 | 144 | 8.56 |
| *p*-xylene | *p*-xylene | $C_6H_4(CH_3)_2$ | 106.078 | 138 | 8.44 |
| anisole | $PhOCH_3$ | $C_6H_4OCH_3$ | 107.05 | 154 | 8.2 |

[a]Data obtained from reference 170

**Table 4.3:** Proton affinity (PA[a]; kJ/mol) of studied solvents in different forms.

| Solvent | Species | PA (kJ/mol) | Solvent | Species | PA (kJ/mol) | Solvent | Species | PA (kJ/mol) |
|---|---|---|---|---|---|---|---|---|
| acetonitrile | $[S - H]^{\bullet}$ | 538 | acetone | $[S - H]^{\bullet}$ | 778 | anisole | S | 840 |
| water | $[S - H]^{\bullet}$ | 593 | acetonitrile | S | 779 | *o*-xylene | $[S - H]^{\bullet}$ | 845 |
| methylene chloride | S | 629 | toluene | S | 784 | *p*-xylene | $[S - H]^{\bullet}$ | 866 |
| chloroform | S | ~635 | cyclohexane | cyclohexene | 784 | dimethylsulfoxide | $[S - H]^{\bullet}$ | 879 |
| hexafluorobenzene | S | 648 | ethylbenzene | S | 788 | dimethylsulfoxide | S | 884 |
| methanol | $[S - H]^{\bullet}$ | 660 | tetrahydrofuran | $[S - H]^{\bullet}$ | 789 | *N*,*N*-dimethylformamide | S | 888 |
| hexanes | S | ~680 | 2-propanol | S | 793 | methanol | $S_2$ | 891 |
| heptane | S | ~680 | *p*-xylene | S | 794 | benzene | $[S - H]^{\bullet}$ | 895 |
| iso-octane | S | ~680 | *o*-xylene | S | 796 | acetonitrile | $S_2$ | 909 |
| cyclohexane | S | 687 | heptane | Isobutene | 802 | ethanol | $S_2$ | 910 |
| water | S | 691 | isooctane | Isobutene | 802 | chlorobenzene | $[S - H]^{\bullet}$ | 913 |
| ethanol | $[S - H]^{\bullet}$ | 689 | hexanes | Hexene | ~805 | 2-propanol | $S_2$ | 927 |
| 2-propanol | $[S - H]^{\bullet}$ | 714 | acetone | S | 812 | acetone | $S_2$ | 938 |
| ethylacetate | $[S - H]^{\bullet}$ | 723 | tetrahydrofuran | S | 822 | tetrahydrofuran | $S_2$ | 948 |
| benzene | S | 750 | water | $S_2$ | 825 | ethylacetate | $S_2$ | 963 |
| chlorobenzene | S | 753 | *N*,*N*-dimethylformamide | $[S - H]^{\bullet}$ | 824 | fluorobenzene | $[S - H]^{\bullet}$ | 900 |
| methanol | S | 754 | ethylbenzene | $[S - H]^{\bullet}$ | 828 | anisole | $[S - H]^{\bullet}$ | 995 |
| fluorobenzene | S | 756 | ethylacetate | S | 836 | dimethylsulfoxide | $S_2$ | 1013 |
| ethanol | S | 776 | toluene | $[S - H]^{\bullet}$ | 838 | *N*,*N*-dimethylformamide | $S_2$ | 1014 |

[a]Data obtained from reference 1, or estimated by the method described in Appendix A-1.

For alcoholic solvents (*i.e.*, methanol, ethanol, and 2-propanol), the formation of $[S_2 + H - H_2O]^+$ ions observed are produced by the condensation reaction of a protonated alcohol with a neutral molecule to form a protonated ether ion plus water.[174]

Spectra of benzene derivative solvents all display $S^{+\bullet}$ and $[S + H]^+$, except for hexafluorobenzene, which only displays $S^{+\bullet}$. All ions possess IE values lower than helium's metastable energy and will be ionized through Mechanism 4.1 to generate $S^{+\bullet}$. However, $S^{+\bullet}$ ions cannot react with S to undergo Mechanism 4.2 since PA($S^{+\bullet}$) values are weaker than PA($[S - H]^{\bullet}$) (see Table 4.2). They still may react with water clusters via Mechanism 4.3 to form protonated solvent monomers since all PA($S_n$) > PA($H_2O$). Hexafluorobenzene spectra lack protonated solvent ions because the PA($C_6H_6$) = 648 kJ is weaker than water's (691 kJ). Additional ions were observed for hexafluorobenzene and fluorobenzene. The $[S - F + OH]^+$ ions are thought to arise from a nucleophilic aromatic substitution reaction of $S^{+\bullet}$ with water. This is an exothermic reaction (by approximately -84 kJ for both hexafluorobenzene and fluorobenzene) driven by the extremely strong bond strength of neutral HF. The presence of $[S - F + H_2O]^+$ probably arises from the reaction of protonated fluorobenzene $[S + H]^+$ with water, losing HF. Similarly, the presence of $[2S - 2F + H_2O]^+$ ions as a side product of $C_6H_5F$ (but not $C_6H_6$) implies that this likely arises ultimately from the [S + H]+ ion. For ethyl benzene, a $[S - H]^+$ ion was also observed, which could be interpreted similarly to the alkanes in the next paragraph.

Alkane solvents mainly only display $S^{+\bullet}$ since all possess IE values lower than helium's metastable energy, thus undergoing Mechanism 1.1. However, protonated

radical alkanes are known to undergo hydride/alkide abstraction reactions to form $[S^{+\bullet} - (CH_2)_n - H]^+$ ions:[175]

$$S^{+\bullet} + S \longrightarrow [S - H]^{\bullet} + C_nH_{2(n+1)} + [S - (CH_2)_n - H]^+, \text{ where } n = 0, 1, 2,\ldots$$

$[S - (CH_2)_n - H]^+$ ions may be considered as $[S + H]^+$ ions of the corresponding alkanes.

Chlorinated methane solvents also have IE values lower than helium's metastable energy and undergo Mechanism 1.1 to form $S^{+\bullet}$. These solvents are dominated by alkane and chlorinated side-products, however, as seen in Table 4.1. Note that chloroform is listed twice in Table 4.1 to due to incorporations of different preservatives commonly used in this solvent. These solvent radicals may undergo a hydride/HCl abstraction reactions to form $[S - H]^+$ and/or $[S - Cl]^+$ ions:

$$CH_2Cl_2^{+\bullet} + CH_2Cl_2 \longrightarrow CHCl_2^{\bullet} + H_2 + CHCl_2^+$$

$$CHCl_3^{+\bullet} + CHCl_3 \longrightarrow CCl_3^{\bullet} + HCl + CHCl_2^+$$

both of which accounts for $CHCl_2^+$ seen in all three solvents, and

$$CHCl_3^{+\bullet} + CHCl_3 \longrightarrow CCl_3^{\bullet} + H_2 + CCl_3^+$$

which accounts for $CCl_3^+$ found in chloroform. However, the appearance energy for $CHCl_2^+$ in $CHCl_3$ spectra is only 0.1 eV above the IE,[170] and 0.8 eV above the IE for $CH_2Cl_2$. $[S - H]^+$ and/or $[S - Cl]^+$ ions may be fragment ions formed upon ionization of the halogenated matrices. Amylene and cyclohexane preservatives are usually added to commercial methylene chloride to act as stabilizers (15- 100 ppm and 40-100 ppm, respectively). Similarly, 50 ppm pentane or 0.75% ethanol is usually

added to commercial chloroform. These preservatives were ionized and account for other detected ions in the spectra.

### 4.2.2 Analysis of Solutions

A group of test compounds were selected to represent a large range of proton affinities: , naphthalene, 1,2,4,5-tetramethylbenzene (1,2,4,5-TMB), decanoic acid, 1-naphthol, anthracene, 1,3-dimethoxybenzene (1,3-DMOB), 9-methylanthracene, 12-crown-4, *N*,*N*-dimethylaniline ($PhNMe_2$),and tributylamine. All compounds, listed in order of proton affinity (PA), are listed in Table 4.4 including formula, $M^{+\bullet}$ and $[M + H]^+$ $m/z$ values, ionization energy (IE) and common abbreviation (all structures shown in Appendix Figure A.2). IE and PA values for decanoic acid are estimated from those of smaller carboxylic acids via standard estimation schemes.[176] The PA for 1,2,4,5-TMB is taken as that of 1,2,3,5-TMB. The PA of 1-naphthol is taken as that of phenol plus the difference between the PA values of naphthalene and benzene; this estimation agrees very well with computational values for protonation para to the hydroxyl group.

Solutions were formed for most solvents (discussed in the previous section) that contained ~ 1 μL each of all ten test compounds (described in the above paragraph). The solvents used were: methanol, acetonitrile, 2-propanol, acetone, THF, ethyl acetate, DMF, DMSO, anisole, o-xylene, toluene, chlorobenzene, fluorobenzene, hexanes, heptane, iso-octane, methylene chloride, and chloroform. Relative intensities of observed peaks in these solutions are shown in Table 4.5.

**Table 4.4:** Chemical formulae, expected $m/z$ values for $M^{+\bullet}$ and $[M + H]^+$ ions, boiling points (bp), ionization energy (IE) values, and proton affinity (PA) values for the studied compounds.

| Compound | Common Abbreviation | Formula | $m/z$ of $M^{+\bullet}$ | $m/z$ of $[M + H]^+$ | BP (°C) | IE (eV) | PA (kJ/mol) |
|---|---|---|---|---|---|---|---|
| Naphthalene | naphthalene | $C_{10}H_8$ | 128.063 | 129.07 | 218 | 8.14 | 803 |
| 1,2,4,5-tetramethylbenzene | 1,2,4,5-TMB | $C_{10}H_{14}$ | 134.11 | 135.117 | 192 | 8.06 | ~846 |
| Decanoic acid | decanoic acid | $C_{10}H_{20}O_2$ | 172.146 | 173.154 | 268-270 | ~9.90 | ~848 |
| 1-Naphthol | 1-Naphthol | $C_{10}H_8O$ | 144.058 | 145.065 | 278-280 | 7.76 | ~867 |
| Anthracene | Anthracene | $C_{14}H_{10}$ | 178.078 | 179.086 | 340 | 7.44 | 877 |
| 1,3-Dimethoxybenzene | 1,3-DMOB | $C_8H_{10}O_2$ | 138.068 | 139.076 | 85-87 (7 mmHg) | 8.2 | ~892 |
| 9-Methylanthracene | 9-methylanthracene | $C_{15}H_{12}$ | 192.094 | 193.102 | 196-197 (12 mmHg) | 7.31 | 897 |
| 12-Crown-4 | 12-Crown-4 | $C_8H_{16}O_4$ | 176.105 | 177.113 | 61-70 (0.5 mmHg) | 8.8 | 927 |
| N,N-Dimethylaniline | $PhNMe_2$ | $C_8H_{11}N$ | 121.089 | 122.097 | 193-194 | 7.12 | 941 |
| Tributylamine | TBA | $C_{12}H_{27}N$ | 185.214 | 186.222 | 216 | 7.4 | 999 |

**Table 4.5**: Observed ion peaks in the DART mass spectra of analytes in solutions[a]

| | ***N*,*N*-dimethylalanine** | | **naphthalene** | | **1,2,4,5-tetramethylbenzene** | | **1,3-dimethoxybenzene** | | **1-naphthol** | |
|---|---|---|---|---|---|---|---|---|---|---|
| **Solvent** | $M^{+\bullet}$ | $[M + H]^+$ | $M^{+\bullet}$ | $[M + H]^+$ | $M^{+\bullet}$ | $[M + H]^+$ | $M^{+\bullet}$ | $[M + H]^+$ | $M^{+\bullet}$ | $[M + H]^+$ |
| methanol | | 49 | | | | | | 18 | | |
| acetonitrile | | 13 | | | | | | | | |
| isopropyl alcohol | | B | | | | | | B | | |
| acetone | | 12 | | | | | | | | |
| tetrahydrofuran | | 5 | | | | | | | B | B |
| ethylacetate | | 2 | | | | | | | | |
| anisole | 25 | 36 | | | | | | 8 | | |
| o-xylene | B | B | | | 5 | 4 | 11 | 9 | 6 | 18 |
| toluene | 27 | 35 | 4 | | 7 | 2 | 8 | 17 | 9 | 6 |
| chlorobenzene | 34 | 27 | B | B | 15 | 6 | 16 | 17 | 12 | 4 |
| fluorobenzene | 51 | 63 | 3 | | 5 | 3 | 10 | 28 | 8 | 5 |
| hexanes | 31 | 78 | 9 | 1 | 11 | 5 | 13 | 45 | 12 | 16 |
| heptane | 20 | 52 | 8 | 8 | 10 | 6 | 10 | 37 | 10 | 15 |
| iso-octane | 12 | 56 | 2 | B | 4 | 3 | 4 | 33 | 4 | 8 |
| dimethylchloride | B | 36 | | | | 3 | | B | | 3 |
| chloroform | B | 100 | | | | 5 | | B | | 12 |

[a]Ion intensity was normalized to the base peak as a percentage. The contribution of ion intensity from the isotopic peak of [$m/z$ – 1] was subtracted. The symbol "B" used in this table represents a background ion.
[b]No relevant peaks were observed when dimethylfuran or dimethylsufoxide were used.
[c]A $m/z$ 142.16 ion, which may be $[(C_4H_9)_2NCH_2]^{+\bullet}$, was observed. It may be a fragment from an unstable $M^{+\bullet}$ ion.
[d]0.75% ethanol is present as a preservative.

**Table 4.5 Continued**: Observed ion peaks in the DART mass spectra of analytes in solutions[a]

| | decanoic acid | | 12-crown-4 | | anthracene | | tributyl-amine | | 9-methyl-anthracene | |
|---|---|---|---|---|---|---|---|---|---|---|
| **Solvent** | $M^{+\bullet}$ | $[M + H]^+$ | $M^{+\bullet}$ | $[M + H]^+$ | $M^{+\bullet}$ | $[M + H]^+$ | $M^{+\bullet}$ | $[M + H]^+$ | $M^{+\bullet}$ | $[M + H]^+$ |
| methanol | | | | 31 | | | | 34 | | 7 |
| acetonitrile | | | | 27 | | | | 21 | | |
| isopropyl alcohol | | | | 18 | | | | 17 | | |
| acetone | | | | 18 | | | | 19 | | |
| tetrahydrofuran | | | | 6 | | | | 3 | | |
| ethylacetate | | | | B | B | B | | 0 | | |
| anisole | | 3 | | 12 | 5 | | 19 | 15 | 5 | 0 |
| o-xylene | | 0 | | 18 | 11 | 1 | 17 | 20 | 13 | 3 |
| toluene | | 0 | | 32 | 16 | 12 | 20 | 33 | 19 | 15 |
| chlorobenzene | | 5 | | 17 | 15 | 8 | 20 | 21 | 15 | 9 |
| fluorobenzene | B | 5 | | 36 | 13 | 8 | 19 | 63 | 13 | 12 |
| hexanes | | 7 | | 72 | 13 | 22 | 20 | 80 | 12 | 19 |
| heptane | | 9 | | 49 | 14 | 24 | 11 | 42 | 16 | 28 |
| iso-octane | | 3 | | 41 | 6 | 17 | 5 | 36 | 9 | 16 |
| dimethylchloride | | 5 | | 30 | | 6 | | 27 | | 9 |
| chloroform | | 6 | | 70 | | 19 | | 76 | | 23 |

[a]Ion intensity was normalized to the base peak as a percentage. The contribution of ion intensity from the isotopic peak of $[m/z - 1]$ was subtracted. The symbol "B" used in this table represents a background ion.
[b]No relevant peaks were observed when dimethylfuran or dimethylsufoxide were used.
[c]A *m/z* 142.16 ion, which may be $[(C_4H_9)_2NCH_2]^{+\bullet}$, was observed. It may be a fragment from an unstable $M^{+\bullet}$ ion.
[d]0.75% ethanol is present as a preservative.

Ethanol, benzene, fluorobenzene, ethyl benzene, and *p*-xylene were not analyzed because of close similarities to other solvents.

Ion intensities are normalized to the highest intensity observed: *N*,*N*-dimethylaniline in chloroform. Representative spectra for each of the following solvents of the four classes (a proton acceptor, methanol; benzene derivative, toluene; alkane, hexane; and chlorinated methane; chloroform) are displayed in Figure 4.1 - 4.4.

When analytes are dissolved in proton acceptor solvents (*i.e.*, methanol, acetonitrile, 2-propanol, acetone, THF, ethyl acetate, DMF, and DMSO), only protonated analyte molecules are detected ($[M + H]^+$). Since proton acceptor solvents are dominated by $[S_2 + H]+$ ions, the analytes are probably ionized through Mechanism 4.4:

$$[S_n + H]^+ + M \longrightarrow S_n + [M + H]^+ \quad \text{(Mechanism 4.4)}$$

which occurs when $PA(M) > PA(S_n) > PA(S - H)^-$. See Table 4.4 and 4.3 for comparison of PA values. Methanol, possessing the weakest $PA(S_2)$ among the proton acceptor solvents, results in the highest intensities for all analytes (See Table 4.5). Even with methanol, however, five of the ten analytes are missing from the methanol spectrum (Figure 4.1): naphthalene, 1,2,4,5-TMB, decanoic acid, 1-naphthol, and anthracene, which all possess proton affinities (PA) below that of methanol Thus, if PA(M)-PA(S) is negative, ionization of M will not occur. DMF and DMSO have the highest PA values and all PA(M)-PA(S) are negative.

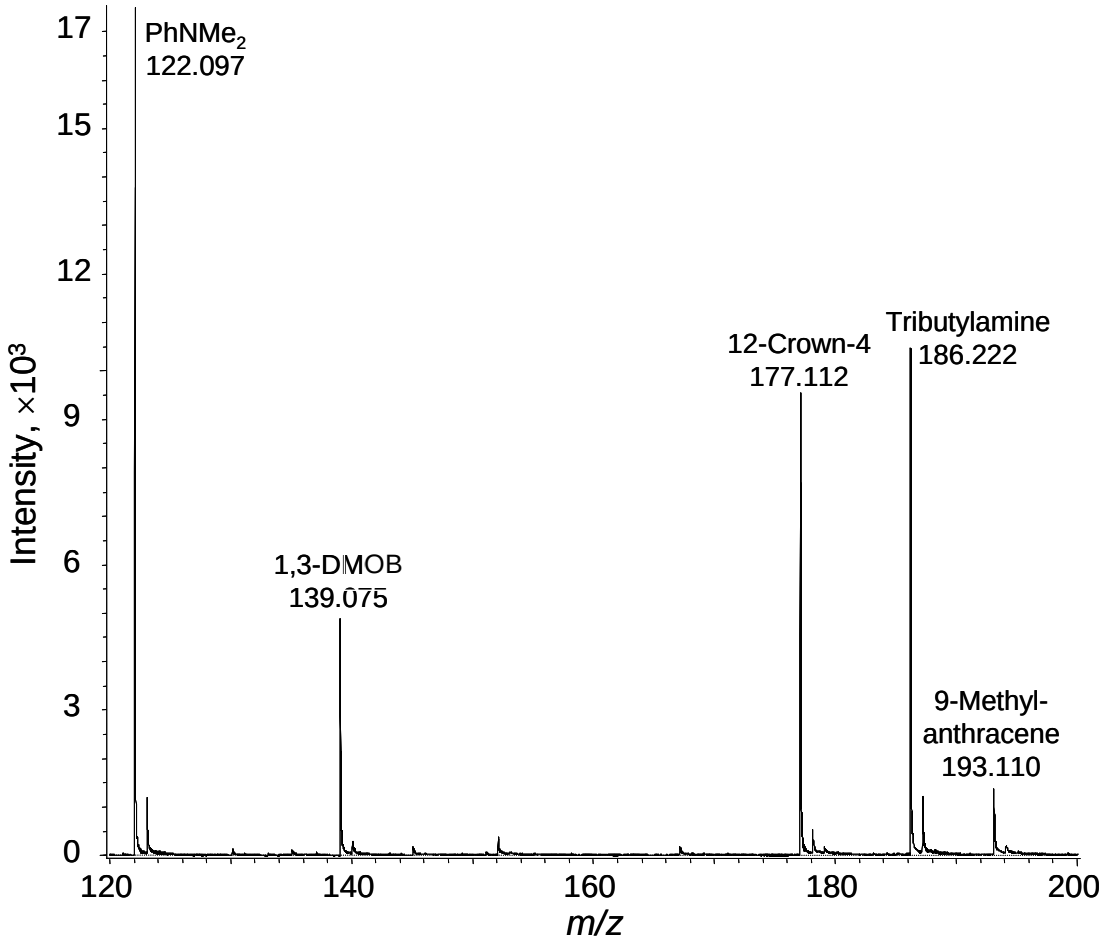


**Figure 4.1**: DART spectrum of a solution containing approximately 1 μL of naphthalene, 1,2,4,5-TMB, decanoic acid, 1-naphthol, anthracene, 1,3-DMOB, 9-methylanthracene, 12-crown-4, $PhNMe_2$ and tributylamine at a concentration of 1 μg/mL in methanol.

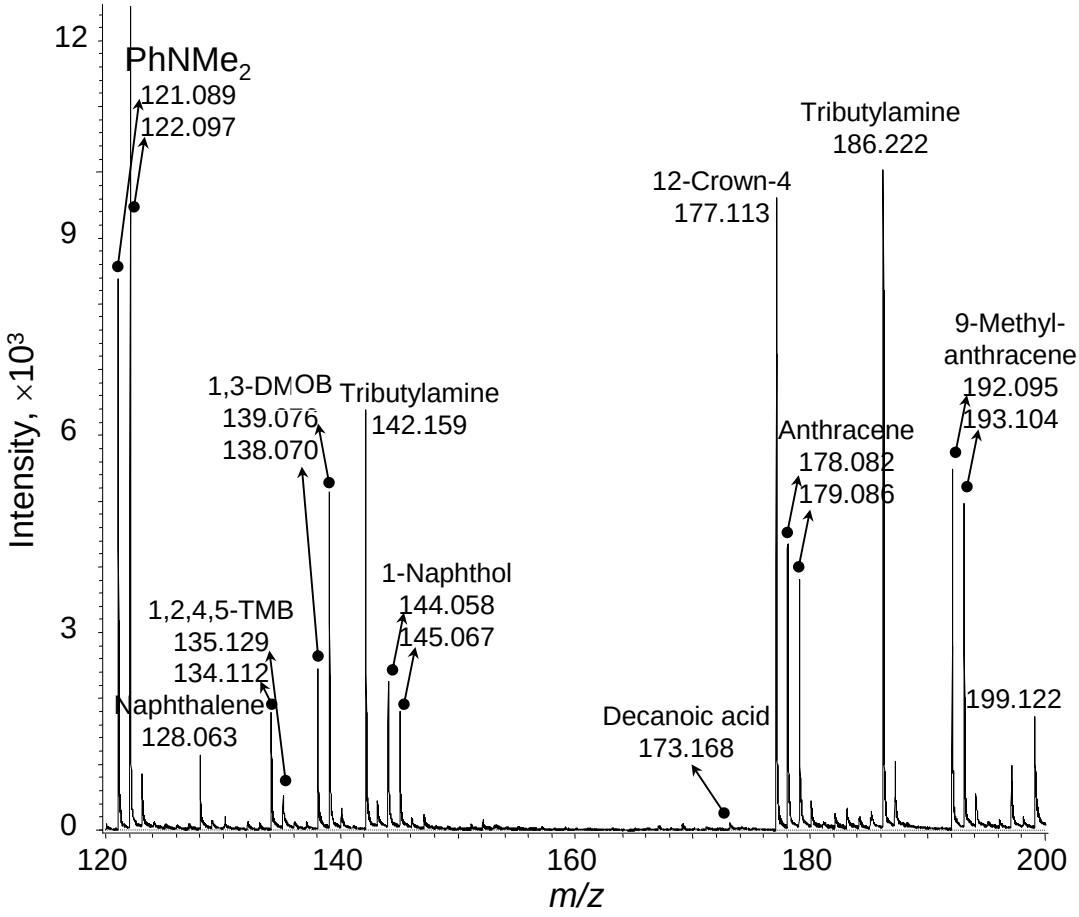


**Figure 4.2**: DART spectrum of a solution containing approximately 1 μL of naphthalene, 1,2,4,5-TMB, decanoic acid, 1-naphthol, anthracene, 1,3-DMOB, 9-methylanthracene, 12-crown-4, $PhNMe_2$ and tributylamine at a concentration of 1 μg/mL in toluene.

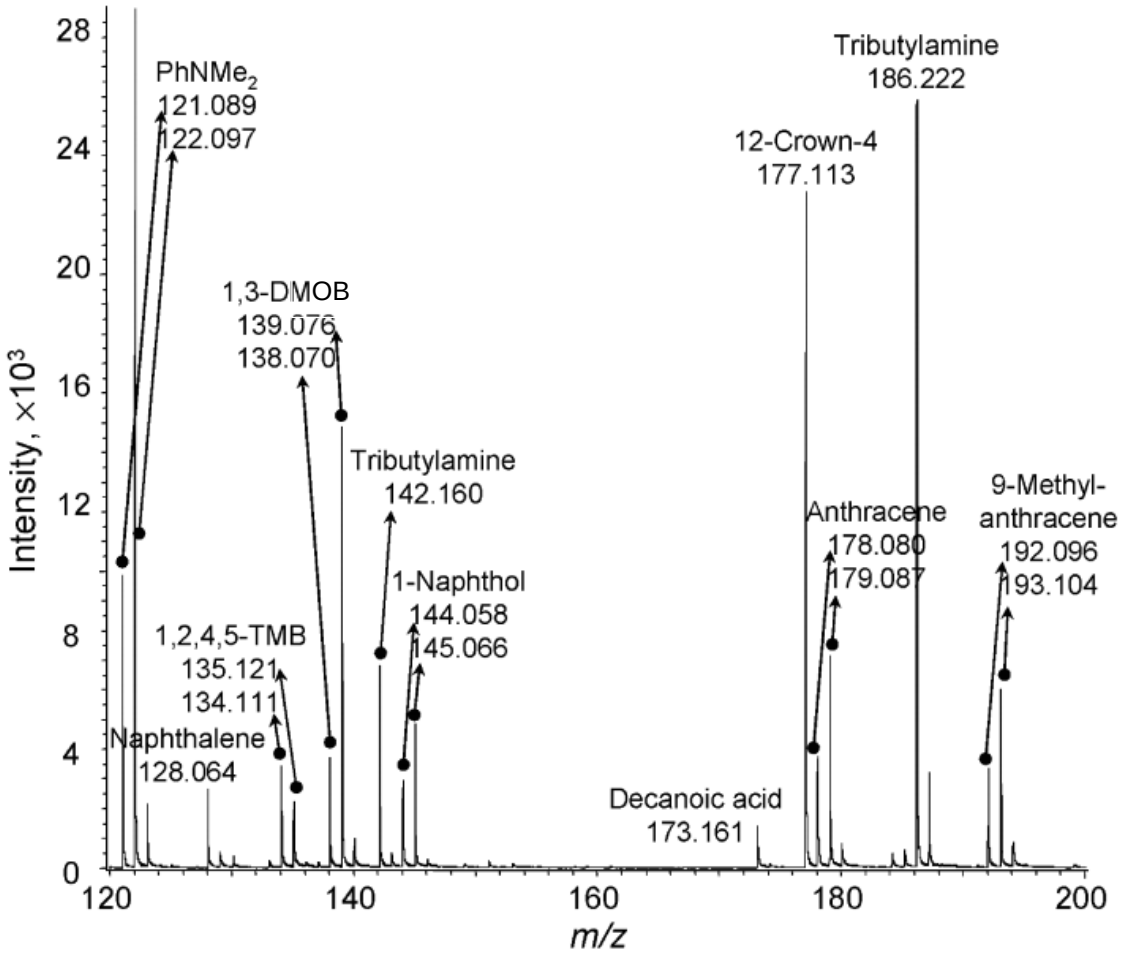


**Figure 4.3:** DART spectrum of a solution containing approximately 1 μL of naphthalene, 1,2,4,5-TMB, decanoic acid, 1-naphthol, anthracene, 1,3-DMOB, 9-methylanthracene, 12-crown-4, $PhNMe_2$ and tributylamine at a concentration of 1 μg/mL in hexanes.

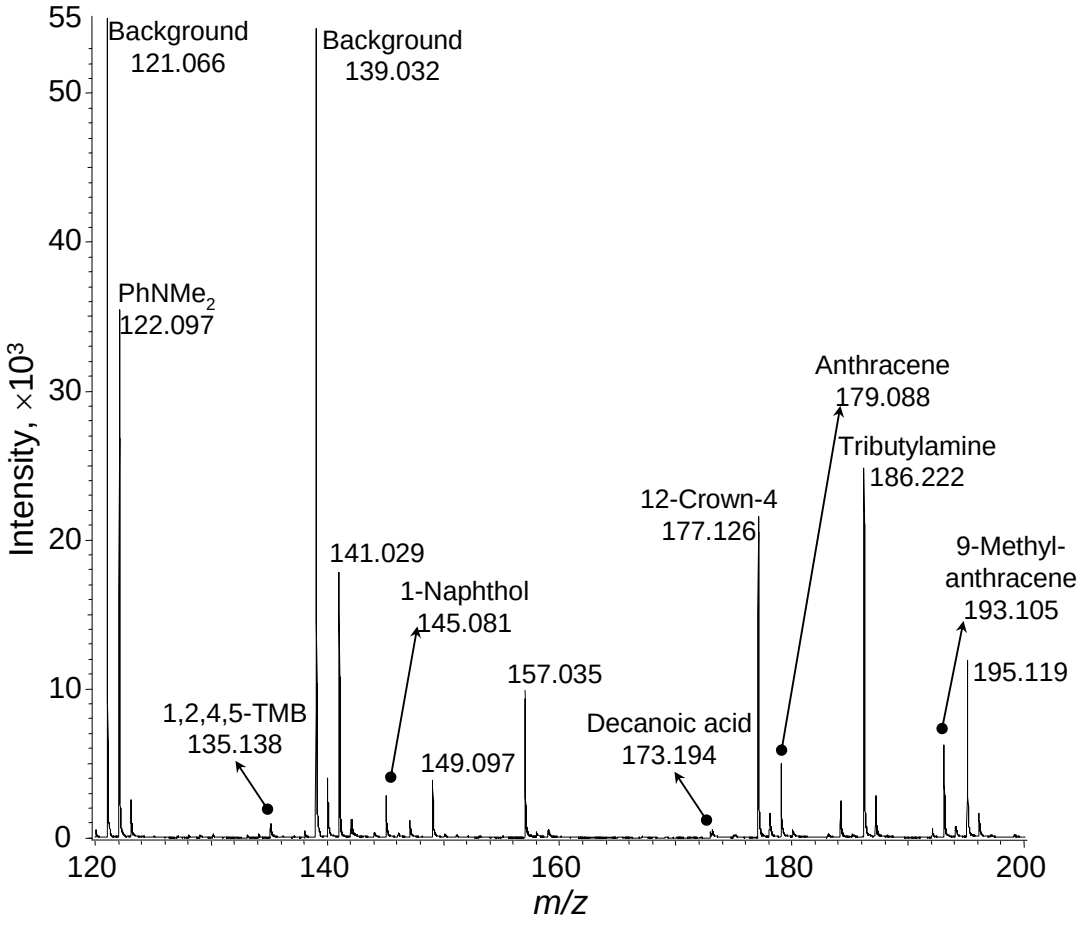


**Figure 4.4:** DART spectrum of a solution containing approximately 1 μL of naphthalene, 1,2,4,5-TMB, decanoic acid, 1-naphthol, anthracene, 1,3-DMOB, 9-methylanthracene, 12-crown-4, $PhNMe_2$ and tributylamine at a concentration of 1 μg/mL in chloroform.

DMF and DMSO are the least effective solvents because of relation and no relevant analyte peaks were observed in either solvent, whose listings were consequently omitted from Table 4.5.

Analytes dissolved in benzene derivate solvents (*i.e.*, anisole- o-xylene, toluene, chlorobenzene, and fluorobenzene) displayed ion counts considerably more abundant than the proton acceptor class, displaying more abundant $[M + H]^+$ ions as well as radical molecules ($M^{+\bullet}$). Ionization can proceed through Mechanism 4.4 to produce $[M + H]^+$ ions. Since the spectra for these solvents are dominated by $S^{+\bullet}$ and $[S + H]^+$ ions, (see Table 4.2), two additional mechanisms are possible.

$$S^{+\bullet} + M \longrightarrow [S - H]^{\bullet} + [M + H]^+ \qquad \text{(Mechanism 4.5)}$$

which occurs if PA(M) > PA$[(S - H)]^{\bullet}$ and contributes to $[M + H]^+$ ion production alongside Mechanism 4.4. Additionally, radical analytes may form via:

$$S^{+\bullet} + M \longrightarrow S + M^{+\bullet} \qquad \text{(Mechanism 4.6)}$$

which occurs when IE(M)-IE(S) values are negative. No significant $M^{+\bullet}$ ions were detected for decanoic acid because of its high IE. No $M^{+\bullet}$ ions were detected for 12-crown-4 and tributylamine, likely due to the Mechanism 4.2 (*i.e.*, PA(S)>PA($[S\text{-}H]^{\bullet}$). Analytes in naphthalene display poor ion counts likely because it possesses a PA lower than that of water. Anisole failed to ionize three of the ten analytes due to its low IE among solvents in this class. The most favorable benzene derivative solvent was toluene (spectrum in Figure 4.2). Although chlorobenzene has a higher IE, toluene was selected due to its lower boiling point (383 K vs 404 K).

Figure 4.2 displays a mass spectrum for toluene, which contains ion peaks for all analytes. Interestingly, two peaks may be attributable to tributylamine (also observed in Figure 4.3)- the $[M + H]^+$ adduct and an unexpected, fragmented and unstable $M^{+\bullet}$ ion which is likely $[(C_4H_9)_2NCH_2]^{+\bullet}$ ($m/z$ 142.16; 0.0 and 7.0 ppm error for Figure 4.2 and 4.3, respectively).

Analytes dissolved in alkane solvents (*i.e.*, hexanes, heptane, and iso-octane) displayed similar results to benzene derivative solvents. Ionization can proceed through Mechanism 4.4 to produce $[M + H]^+$ ions because PA(M)-PA(S) values are positive. This is supported by Figure 4.3 and Table 4.2 since $[S - (CH_2)_n - H]^+$ ions may be considered as $[S + H]^+$ ions. Most analytes were also ionized as $M^{+\bullet}$ ions, occurring through Mechanism 4.6, which requires the existence of $S^{+\bullet}$ ions of alkane solvents and for IE(S) > IE(M). Although peaks representing $S^{+\bullet}$ were not directly observed, they did exist as precursors to $[S - (CH_2)_n - H]^+$ ions. Such radical cations are thermochemically higher in energy, as necessary for Mechanism 4.2 (since $[S - (CH_2)_n - H]^+$ ions may be considered as $[S + H]^+$ ions), than benzene derivative radical cations. Thus, alkane radical cations may have a shorter lifetime in the source and are not observed. There was no significant difference among alkane solvents with respect to the ionization of all analytes. Figure 4.3 shows the corresponding mass spectrum when hexanes were used.

When methylene chloride and chloroform were used as solvents, lower abundances were observed for $M^{+\bullet}$ ions, which may imply a greater reactivity of $M^{+\bullet}$ ions than considered with alkanes. This is consistent with the higher IE of

methylene chloride and chloroform when compared to alkanes. In addition, the ionization of the analytes and stabilizers in the solvents seemed similar. Protonated pentene was observed in methylene chloride due to the 15-100 ppm amylene (presumably 1-pentene) used as a stabilizer. Different chloroform solutions contained separate stabilizers: 0.75% ethanol and 50 ppm pentene. This resulted in protonated monomers and dimers of ethanol were observed with the 0.75% ethanol. Protonated pentene was observed for 50 ppm pentene (with other pentene fragment ions (similar to $[S - (CH_2)_n - H]^+$ (n = 1, 2, 3…)) and $C_6H_{10}Cl^+$ of unknown provenance.

### 4.2.3 The Impact of Matrix Effects on DART

In the provided investigations discussed above, it is clear solvents impact the mass spectra generated by DART. Typical analytes usually exist in small amounts in a solvent (*i.e.*, a matrix), Cody[18,128] propose a mechanism where protonated water clusters, mostly $H_5O_2^+$, react with analytes through gas-phase ion/molecule reactions. However, protonated water dimers are statistically more likely to first encounter solvent over dissolved analyte. This mechanism does not address this observation or why different solvents yield different ionization patterns even among the same analyte.

Mechanisms 4.1 – 4.6 have been combined into a more complete DART ionization scheme, called the Transient Micro-Environment Mechanism (TMEM). When the DART gas stream contacts a sample, a transient microenvironment (TME)

will shield analytes from direct ionization by both He* and $H_5O_2^+$. The DART gas stream will therefore *directly* ionize the volatile matrix molecules (the TME), which will proceed to ionize molecules contained in the matrix through gas phase ion/molecule reactions.

Scheme 1, comprised of Equations 1.11 and 1.12 as well as Mechanisms 4.1-4.6 (and Mechanism 4.7, described in the next section), is composed of a series of reactions that describe possible pathways whereby solution components may be ionized. There are three steps:

1) When the helium gas stream, containing metastable species, is in contact with the atmosphere, molecular ions of water are formed (Equation 1.11). This, in turn, produces protonated water clusters (Equation 1.12).
2) When $He^{\bullet}$ contacts solvent molecules, a TME forms. Mechanism 4.1 describes the creation of radical solvent molecules, $S^{+\bullet}$. Radical solvent molecules will react with other solvent molecules to produce protonated solvent molecules (Mechanism 4.2). Protonated solvent molecules may also form when protonated water clusters can react with solvent molecules (Mechanism 4.3).
3) Protonated analyte molecules form through gas-phase ion/molecule reactions with protonated solvent molecules and the analyte contained in the TME (Mechanism 4.4). Solvent molecular ions may react with analyte molecules to produce both protonated analyte molecules and analyte molecular ions (Mechanism 4.5 and 4.6, respectively).

$He^* + H_2O \rightarrow He + H_2O^{+\cdot} + e^-$, as ME(He)>IE($H_2O$) (Equation 1.11)

$H_2O^{+\cdot} + (H_2O)_m \rightarrow HO^{\cdot} + [(H_2O)_m + H]^+$, as PA($(H_2O)_m$)>PA($HO^{\cdot}$) (Equation 1.12)

$He^* + S \rightarrow He + S^{+\cdot} + e^-$, as ME(He)>IE(S) (Mechanism 4.1)

$S^{+\cdot} + S_n \rightarrow [S - H]^{\cdot} + [S_n + H]^+$, if PA($S_n$)>PA($[S\text{-}H]^{\cdot}$) (Mechanism 4.2)

$[(H_2O)_m + H]^+ + S_n \rightarrow (H_2O)_m + [S_n + H]^+$ if PA($S_n$)>PA($(H_2O)_m$) (Mechanism 4.3)

$[S_n + H]^+ + M \rightarrow S_n + [M + H]^+$, if PA(M)>PA($S_n$)>PA($[S\text{-}H]^{\cdot}$) (Mechanism 4.4)

$S^{+\cdot} + M \rightarrow [S - H]^{\cdot} + [M + H]^+$, if PA(M)>PA($[S\text{-}H]^{\cdot}$)>PA($S_n$) (Mechanism 4.5)

$S^{+\cdot} + M \rightarrow S + M^{+\cdot}$, if PA($[S\text{-}H]^{\cdot}$)>PA($S_n$)

and IE(S)>IE(M) (Mechanism 4.6)

$[(H_2O)_m + H]^+ + M \rightarrow (H_2O)_m + [M + H]^+$, if the TME is thin (Mechanism 4.7)

**Scheme 4.1:** Main reactions in positive-ion DART. ME(He) is helium's metastable energy, 19.8 eV; m=1, 2, or 3; n=1 or 2. Mechanism 4.2 has a few variants for alkanes and chlorinated methanes as described in the text

Note that the TMEM is an extension and clarification of the ionization mechanism proposed by Cody. The TMEM provides a more comprehensive list of possible gas-phase ion/molecule reactions that take place in the positive-ion DART mode. In the original DART article[18], molecular ions of toluene were shown- an observation consistent with the TME.

### 4.2.4 Analysis of Solids

A TME can also consist of vapors from solids which can be desorbed by the DART gas stream and further ionized by DART. Therefore, an analysis of solids without a liquid matrix present can also provide useful information about the TME involved in the DART ionization mechanism. Most of the analytes used in this study are solids natively, so they are analyzed for that purpose.

First, the analytes were sampled by dipping the closed end of a melting point capillary directly into the solid. Approximately 0.1 mg of solid was sampled this way, and similar TMEs to those when approximately 1 μL solvents were analyzed were observed. Next, the amount of solid sample was reduced to assess the changes in the TME. The analytes were dissolved in a solvent, e.g. toluene, at individual concentration of 10 mg/mL, 100 μg/mL, and 1 μg/mL. Analytes were sampled by dipping the closed end of a melting point capillary directly into the solutions of the analytes and then allowing the solution to air dry for approximately 3 minutes. Approximately 10 μg, 100 ng and 1 ng of analytes, which were dried from approximately 1 μL of solution, were analyzed. The results indicated that

approximately 10 μg of solid was required to generate an efficient TME (*e.g.*, a point where both $M^{+\cdot}$ and $[M + H]^+$ ions were abundant for naphthalene). If liquid instead of solid was used, the required volume should be 10 nL assuming a 1 mg/mL density.

Table 4.6 lists the observed ions by positive-ion DART for approximately 10 μg of individual analyte. The generation of $[M - H]^+$, $M^{+\cdot}$ and $[M + H]^+$ ions occurred mostly through Mechanisms 4.1, 4.2, and 4.3, which were also used to interpret the generation of similar ions from the solvents. Note that no $M^{+\cdot}$ ion was observed for decanoic acid and 12-crown-4. Since the analyte is now the matrix, Mechanism 4.2 may apply to these analytes, although the PAs of the corresponding (M-H) radicals were not available. Other ions were also detected, shown in Table 4.3, because of gas-phase ion/molecule reactions, however, interpretation of their formation is beyond the scope of this study. Nevertheless, note that gas-phase reactions for the analytes seemed more complicated than the solvents most of the time.

Figure 4.5 shows a mass spectrum of 1 ng mixture composed of all the analytes considered previously. A $[M + H]^+$ ion was recorded for 1,3-DMOB, 1-naphthol, decanoic acid, 12-Crown-4, anthracene, TBA, and 9-methylanthracene. Note that no ions for naphthalene, 1,2,4,5-TMB and $PhNMe_2$ were observed. Although the absence of protonated naphthalene could be due to its weaker PA than the dimer of water, the absence of protonated 1,2,4,5-TMB and $PhNMe_2$ was puzzling. This may be due to unknown gas-phase ion/molecule reactions.

**Table 4.6**: Observed ion peaks with relative intensity over 10% in the DART mass spectra[a].

| | Relative Intensity | | | | | |
|---|---|---|---|---|---|---|
| Analytes | $[M - H]^+$ | $M^{+\cdot}$ | $[M + H]^+$ | $[M_2 + H]^+$ | Others detected ions | |
| Naphthalene | | 68% | 100% | | | |
| 1,2,4,5-TMB | 11% | 91% | 100% | | | |
| Decanoic acid | | | 61% | 100% | $[M - H_2O + H]^+$ | 58% |
| 1-Naphthol | | 43% | 100% | | | |
| Anthracene | | 51% | 100% | | | |
| 1,3-DMOB | | 17% | 100% | | $[M – H + CH_3]^+$ | 20% |
| 9-Methylanthracene | | 78% | 100% | | $[M + O]^+$<br>$[M + O_2 + H]^+$ | 12%<br>27% |
| 12-Crown-4 | | | 100% | | | |
| $PhNMe_2$ | 44% | 36% | 100% | | $[M + CH_3]^+$<br>$[M - CH_3 + 2H]^+$ | 20%<br><10% |
| Tributylamine | 24% | | 100% | | $[M - C_3H_7]^+$ | 83% |

[a]Contribution of ion intensity from the isotopic peak of [m/z – 1] was subtracted.

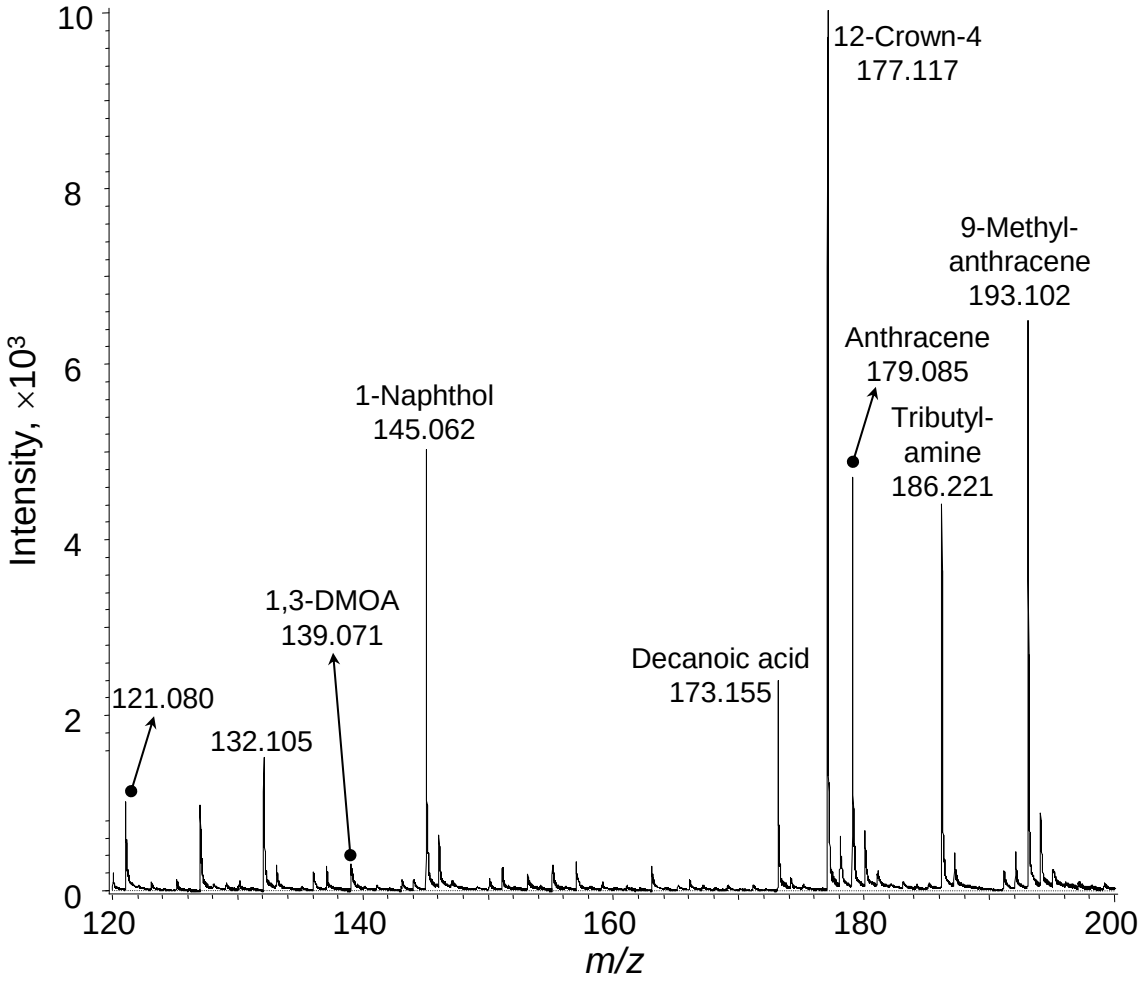


**Figure 4.5:** DART spectrum of solid residue containing approximately 1 ng each of naphthalene, 1,2,4,5-TMB, decanoic acid, 1-naphthol, anthracene, 1,3-DMOB, 9-methylanthracene, 12-crown-4, $PhNMe_2$ and tributylamine.

The lack of these ions suggests solid state DART analysis is not always a better choice than solution analysis. The DART source likely induces a very thin TME for pure, solid analytes composed of desorbed analyte. Thus, water clusters will be able to directly ionize the analyte, described by Mechanism 4.7 in Scheme 1.

### 4.2.5 Analysis of Impurities in Solids

Vapors of solids can generate an efficient TME under DART conditions. The ionization of impurities in these solids should occur through gas-phase ion/molecule reactions with the ions of these solids. Two such samples, 1 ng of 1-naphthol in 10 μg of naphthalene and 1 ng naphthalene in 10 μg of 1-naphthol (1:10,000), were analyzed. Abundant $M^{+\bullet}$ and $[M + H]^+$ ions of naphthol were observed for the sample of 1 ng naphthol in 10 μg naphthalene. As shown in Table 4.6, the TME from 10 μg naphthalene consisted of its $M^{+\bullet}$ and $[M + H]^+$ ions, which would ionize naphthol through Mechanism 4.4 and 4.6 in Scheme 4.1 because naphthol possesses a lower IE and stronger PA value than naphthalene (Table 4.4).

A critical analyte-to-matrix ratio is explored to better predict the effect of TME. When the analyte-to-matrix ratio is lower than the critical ratio value, DART ionization will be controlled by the TME. Three more samples were analyzed: 10 ng, 100 ng, and 1000 ng of naphthalene each individually in 10 μg naphthol, providing solute:solvent ratios of 1:1000, 1:100, and 1:10, respectively. $M^{+\bullet}$ and $[M + H]^+$ ions of naphthalene were observed when naphthalene is in excess of 100 ng, which indicated that the DART ionization was not controlled by the TME anymore. High

concentrations of analyte create a thicker/denser TME (see Mechanism 4.7 and the end of last section), which does inhibits the access of He* and/or water dimers to the liquid phase. Therefore, naphthalene ionization in a naphthol matrix was mainly controlled by the TME in ratios below 1:100. Note that the critical ratio should be dependent on the DART temperature and the boiling points of the analyte and matrix.

## 4.3 Conclusions

The ionization mechanism of DART previously proposed by Cody[18] has been expanded in this study by specifically addressing the matrix effect with a TMEM. The TMEM is supported by a Scheme consisting of nine gas-phase ion/molecule reactions. Simulated samples of liquids, solids and solutions were analyzed and the mass spectra were interpreted. The relevant TMEs generated from most of the common solvents in four groups, i.e. proton acceptors, benzene derivatives, alkanes, and chlorinated methanes, were studied in detail. Methanol, toluene, hexanes and chloroform were found to be the best representatives and provide complimentary data. It is important to clarify that THF, ethyl acetate, DMF and DMSO are unfavorable solvents for DART ionization. More complicated DART TMEs and ionization mechanisms can be expected when a sample contains multiple matrix components, but the ionization mechanisms should still be interpretable through the TMEM. Since DART is the premiere APCI-related OADI method, this study may

provide useful fundamentals on the ionization mechanism of other APCI-related OADI methods, especially when solvent is involved in the ionization.

# Chapter 5. Conclusions and Suggestions for Future Work

Characterization of ionization source processes is incredibly valuable to the interpretation of mass spectra. The origins of chemical changes in ionization sources must be explored in order to be cognizant of the chemical differences between an analyte in its original condensed phase and its gas-phase counterparts. Research presented in this dissertation probes the fundamental ionization mechanisms of ESI and DART in order to provide a clearer picture of how these ion sources impact analytes.

## 5.1 Electrospray Plume Temperature Determinations

This work demonstrated the first experimental determination of the evolution of droplet temperature in an electrospray plume. LIF was used to confirm, as expected, that droplets cool due to evaporation and added additional insight by quantifying plume temperature change in axial (≤ 19 K) and lateral directions (≤ 12 K) as well as variations in temperature due to changes in flow rate. These results were validated by fitting axial experimental data to two evaporation models: surface- and diffusion-control. The diffusion-controlled model is believed to be the more appropriate model as the fit parameters provide values that are in reasonable agreement with literature values (droplet velocity, partial solvent vapor pressure, and droplet radius) and adherence to the critical radius transition value. Since the spray profile began at Z = 0.25 mm, the DCM was backextrapolated to Z = 0 to provide a more complete account of droplet cooling. This modeling predicts a ~26 - 31 K temperature decrease for Z = 0 to Z = 12 mm- a ~10 K decrease solely in the

first 0.25 mm after droplet emission. Clearly, due to the magnitude of this decrease, it would be prudent to take into account any processes that can respond to temperature change in order to properly interpret mass spectrometry data.

Temperature is a parameter in two fundamental equations that may be associated with ESI: the rate at which ion emission occurs from a droplet[46] (Equation 1.5) and the rate at which a droplet evaporates[81] (Equations 3.4 and 3.5 for the DCM and SCM, respectively). Kebarle and Tang[50] were the first to attempt estimation of droplet temperature for electrospray conditions (~8 K decrease for a 10-nm droplet relative to ambient temperature). However, a number of assumptions were made to ease this calculation. First, the calculation was predicated on the assumption that the modeled droplet existed in equilibrium, where heat lost by evaporation is gained from collisions with ambient gas. This situation is unlikely to occur in a dynamic system such as an electrospray plume, as shown in Figure 3.8, where evaporative cooling is predicted, at least initially, to be greater than heat gained by the sum of vapor recondensation and collisional heating. The present study does not change the core of their work - predicting the iteration of coulombic explosions and ion evaporation - as the general trends have been validated elsewhere (see Section 1.2.4).

Our studies may be complementary, however. Calculations of radii decrease herein do not reach Kebarle and Tang's 10-nm droplet size. It is possible that droplets, if allowed to exist in ambient air, will eventually reach a 10-nm droplet size and exhibit further cooling as they discussed. As a result, the present study

investigates temperature in the early stage of a droplet's lifetime, while theirs studies droplets moments before gas-phase ions form.

Equation 3.5, which contains a parameter for temperature, is used by Kebarle and Tang for a number of calculations requiring knowledge of the decrease in droplet radius. They comprehensively model the evaporation and Coulombic explosions of an initial drop of $r_0$ = 1.5 um over time. Curiously, they calculate the temperature decrease for a 10-nm droplet and use the resulting (equilibrium) temperature for 1.5 μm droplets in charge calculations. The present study would assist in making more accurate droplet radii determinations by inserting the additional consideration that droplet temperature changes as a function of time.

Kebarle and Tang use an extremely low value for the condensation coefficient for methanol (α), a parameter only used in the SCM. More recent studies have experimentally determined α as 0.9, which is 23 times larger than that used by Kebarle and Tang. Their value, α = 0.04, may easily be substituted into the SCM model used herein and fitted against experimental data. Note that α does not appear in the DCM. Thus for illustration, the invalidity of the SCM model for droplets emitted from our system is being ignored. By making this substitution, the resulting fitting parameters wildly diverge with published literature values (Section 3.2.6). While the SCM was discounted due to predicting a droplet size greater than the critical radius, the fitted values were still in agreement with literature values. This adds confidence to our choice of condensation coefficient.

It would be incredibly interesting to study droplet temperature, using the LIF technique described herein, in tandem with determination of droplet velocity and size- two of the three fitting parameters in the evaporation models. Such a study would allow experimental monitoring of two of the three unknown parameters that this study lacked capability to observe. Gomez and Tang[45,76] as well as the groups of Vertes,[51,95,158] de la Mora,[159] and Zenobi[177] have all employed phase Doppler anemometry in the ESI plume. Mie scattering has also been employed for droplet radius and velocity determinations by Antoine,[96] though this method was unable to obtain droplet size along the axis of the capillary, where droplet density is too high, due to multi-scattering.

Partial vapor pressure, the third fitting parameter estimated in this study, could be experimentally determined as well. A KinTek humidified gas generator is able to control the temperature and relative partial pressure of a gas cycled through an enclosure. Such a gas generator is able to continuously monitor a wide variety of gas vapors including methanol. The purged enclosure utilized in this study could easily be adapted to use such a device by adding specialty vents to prevent overpressure. The opening allowing the laser into the purged enclosure (and excited light out to be detected) would need to be sealed with an optically transparent material such as glass. Such a modification may decrease overall signal intensity compared with the typical setup due to scattering off the glass, but laser power may easily be increased to compensate. Alternatively, the maximum partial pressure in the box may be reached by simply placing a vessel filled with the

electrosprayed solvent into the purged enclosure; taking caution to ventilate the area for safety would be a must. This method would lack the fine control of a gas generator, but is less expensive and would provide a method to observe the general effect of partial vapor pressure on droplet temperature.

Additional upgrades to the set-up used include adding a third translational axis to the electrospray stage. The extra translational axis would make focusing the apparatus at the beam waist of the laser easier, more precise, and convenient. An LC pump would be useful to avoid frequent interruptions in sample acquisition due to syringes running out of analyte.

A separate study characterizing the effect of the electrospray on the higher order structure of proteins would be interesting, as well. LIF may be used to probe the kinetics of protein folding and/or unfolding in ES droplets by using a solvatochromic dye such as Nile red. As a protein, such as ovalbumin, unfolds (i.e. denatures), more hydrophobic, interior surfaces become exposed. These surfaces will bind with Nile red, resulting in a quantifiable blue shift of the emission maximum. Adding an acid and/or changing temperature to the solution in a cuvette to induce denaturation and comparing that effect with spray data would help explore denaturation kinetics in the spray.

## 5.2 DART Transient Microenvironment Mechanism

By individually studying the ionization patterns of a wide range of solvents and analytes under DART, a coherent scheme was constructed to account for the

interaction between the solvent and solute. The initial mechanism Cody[18,128] proposed to account for DART ionization was broad and did not account for reasons why one solvent was preferable to another. This mechanism states that metastable helium induced Penning ionization of ambient water in open air, generating mostly protonated water dimers. These water dimers would then directly ionize analytes inside the droplet.

However, the proposed transient microenvironment mechanism suggests that analytes are shielded from direct ionization by initial desorption of the volatile matrix/solvent molecules. The DART gas will predominantly ionize the matrix first, which will in turn ionize analyte molecules dissolved inside. Helium possesses a very high ionization energy value and is clearly able to analyze a large number of compounds. However, the rest of the solvent/solute ionization mechanisms predicate on comparison between proton affinities and ionization energies of the two interacting molecules.

Methanol, toluene, hexane, and chloroform were chosen as the most favorable solvents out of their respective categories. The selection criteria consisted of a combination of their general ability to analyze the greatest quantity of analytes as well as the relative abundances of analytes that were able to be analyzed. DMF, DMSO, and THF were universally the worst solvents due to possessing the highest PA($S_2$) values.

In addition to solutions, the DART gas stream may easily analyze analytes in the solid phase. It was determined that at a minimum of 10 μg of solid is necessary

to generate a reasonable amount of molecular and/or protonated adduct ions. Interestingly, most of the time solid-phase analysis produced a more complex set of side adducts when compared to solvent analysis. The interpretation of these gas-phase ion/molecule reactions was out of the scope of the present study. However, probing the formation mechanisms of these adducts may be key to expanding upon the transient microenvironment mechanism.

# References

(1) Watson, J.; Sparkman, O. *Introduction to Mass Spectrometry: Instrumentation, Applications, and Strategies for Data Interpretation*; 4th ed.; John Wiley & Sons, Ltd.: West Sussex, 2007.
(2) Kind, T.; Fiehn, O. Advances in Structure Elucidation of Small Molecules Using Mass Spectrometry. *Bioanal. Rev.* **2010**, *2*, 23–60.
(3) Maxwell, E. J.; Chen, D. D. Y. Twenty Years of Interface Development for Capillary Electrophoresis–electrospray Ionization–Mass Spectrometry. *Anal. Chim. Acta* **2008**, *627*, 25–33.
(4) Daviau, T. R. Modern Practice of Gas Chromatography, *Fourth Edition*. Wiley Interscience, Hoboken, NJ. 2004.
(5) Niessen, W. M. A. *Liquid Chromatography-Mass Spectrometry, Third Edition*; CRC Press, 2006.
(6) Naylor, S.; Kumar, R. Emerging Role of Mass Spectrometry in Structural and Functional Proteomics. *Adv. Protein Chem.* **2003**, *65*, 217–248.
(7) Villas-Bôas, S. G.; Mas, S.; Akesson, M.; Smedsgaard, J.; Nielsen, J. Mass Spectrometry in Metabolome Analysis. *Mass Spectrom. Rev.* **2005**, *24*, 613–646.
(8) Loizides-Mangold, U. On the Future of Mass-Spectrometry-Based Lipidomics. *FEBS J.* **2013**, *280*, 2817–2829.
(9) Bouslimani, A.; Sanchez, L. M.; Garg, N.; Dorrestein, P. C. Mass Spectrometry of Natural Products: Current, Emerging and Future Technologies. *Nat. Prod. Rep.* **2014**, *31*, 718–729.
(10) Gruendling, T.; Weidner, S.; Falkenhagen, J.; Barner-Kowollik, C. Mass Spectrometry in Polymer Chemistry: A State-of-the-Art up-Date. *Polym. Chem.* **2010**, *1*, 599–617.
(11) Becker, S. *Inorganic Mass Spectrometry: Principles and Applications*; 1 edition.; Wiley-Interscience: Chichester, England ; Hoboken, NJ, 2007.
(12) Roddy, T. P.; Horvath, C. R.; Stout, S. J.; Kenney, K. L.; Ho, P.-I.; Zhang, J.-H.; Vickers, C.; Kaushik, V.; Hubbard, B.; Wang, Y. K. Mass Spectrometric Techniques for Label-Free High-Throughput Screening in Drug Discovery. *Anal. Chem.* **2007**, *79*, 8207–8213.
(13) Olivares, J. A. Mass Spectrometry in Process Analysis. In *Encyclopedia of Analytical Chemistry*; John Wiley & Sons, Ltd, 2006.
(14) Smith, D. L. Mass Spectrometry Applications in Forensic Science. In *Encyclopedia of Analytical Chemistry*; John Wiley & Sons, Ltd, 2006.
(15) Eismin, R. J.; Fu, M.; Yem, S.; Widjaja, F.; Kenttämaa, H. I. Identification of Epoxide Functionalities in Protonated Monofunctional Analytes by Using Ion/molecule Reactions and Collision-Activated Dissociation in Different Ion Trap Tandem Mass Spectrometers. *J. Am. Soc. Mass Spectrom.* **2012**, *23*, 12–22.
(16) Carroll, D. I.; Dzidic, I.; Stillwell, R. N.; Haegele, K. D.; Horning, E. C. Atmospheric Pressure Ionization Mass Spectrometry. Corona Discharge Ion Source for Use in a Liquid Chromatograph-Mass Spectrometer-Computer Analytical System. *Anal. Chem.* **1975**, *47*, 2369–2373.

(17) Andrade, F. J.; Shelley, J. T.; Wetzel, W. C.; Webb, M. R.; Gamez, G.; Ray, S. J.; Hieftje, G. M. Atmospheric Pressure Chemical Ionization Source. 1. Ionization of Compounds in the Gas Phase. *Anal. Chem.* **2008**, *80*, 2646–2653.
(18) Cody, R. B.; Laramée, J. A.; Durst, H. D. Versatile New Ion Source for the Analysis of Materials in Open Air under Ambient Conditions. *Anal. Chem.* **2005**, *77*, 2297–2302.
(19) Dole, M. Molecular Beams of Macroions. *J. Chem. Phys.* **1968**, *49*, 2240.
(20) Beckey, H. D. Field Ionization Mass Spectrometry. *Research/Development* **1969**, *20*, 26–29.
(21) Beckey, H. D. *Principles of Field Iniozation and Field Desorption in Mass Spectrometry*; Pergamon Press: Oxford, 1977.
(22) De Hoffman, E.; Stroobant, V. *Mass Spectrometry: Principles and Applications*; Third.; Wiley: West Sussex, 2007.
(23) Barber, M.; Bordoli, R. S.; Sedgwick, R. D.; Tyler, A. N. Fast Atom Bombardment of Solids (F.A.B.): A New Ion Source for Mass Spectrometry. *J. Chem. Soc. Chem. Commun.* **1981**, 325–327.
(24) Fenn, J. B.; Mann, M.; Meng, C. K.; Wong, S. F.; Whitehouse, C. M. Electrospray Ionization for Mass Spectrometry of Large Biomolecules. *Science* **1989**, *246*, 64–71.
(25) Tanaka, K.; Waki, H.; Ido, Y.; Akita, S.; Yoshida, Y.; Yoshida, T.; Matsuo, T. Protein and Polymer Analyses up to M/z 100 000 by Laser Ionization Time-of-Flight Mass Spectrometry. *Rapid Commun. Mass Spectrom.* **1988**, *2*, 151–153.
(26) Wüthrich, K.; Wider, G.; Wagner, G.; Braun, W. Sequential Resonance Assignments as a Basis for Determination of Spatial Protein Structures by High Resolution Proton Nuclear Magnetic Resonance. *J. Mol. Biol.* **1982**, *155*, 311–319.
(27) Robb, null; Covey, null; Bruins, null. Atmospheric Pressure Photoionization: An Ionization Method for Liquid Chromatography-Mass Spectrometry. *Anal. Chem.* **2000**, *72*, 3653–3659.
(28) Hanold, K. A.; Fischer, S. M.; Cormia, P. H.; Miller, C. E.; Syage, J. A. Atmospheric Pressure Photoionization. 1. General Properties for LC/MS. *Anal. Chem.* **2004**, *76*, 2842–2851.
(29) Takats, Z.; Wiseman, J. M.; Gologan, B.; Cooks, R. G. Mass Spectrometry Sampling Under Ambient Conditions with Desorption Electrospray Ionization. *Science* **2004**, *306*, 471–473.
(30) McEwen, C. N.; McKay, R. G.; Larsen, B. S. Analysis of Solids, Liquids, and Biological Tissues Using Solids Probe Introduction at Atmospheric Pressure on Commercial LC/MS Instruments. *Anal. Chem.* **2005**, *77*, 7826–7831.
(31) Huang, M.-Z.; Hsu, H.-J.; Lee, J.-Y.; Jeng, J.; Shiea, J. Direct Protein Detection from Biological Media through Electrospray-Assisted Laser Desorption Ionization/Mass Spectrometry. *J. Proteome Res.* **2006**, *5*, 1107–1116.
(32) Takáts, Z.; Cotte-Rodriguez, I.; Talaty, N.; Chen, H.; Cooks, R. G. Direct, Trace Level Detection of Explosives on Ambient Surfaces by Desorption

Electrospray Ionization Mass Spectrometry. *Chem. Commun.* **2005**, 1950–1952.
(33) Haddad, R.; Sparrapan, R.; Eberlin, M. N. Desorption Sonic Spray Ionization for (high) Voltage-Free Ambient Mass Spectrometry. *Rapid Commun. Mass Spectrom.* **2006**, *20*, 2901–2905.
(34) Sampson, J. S.; Hawkridge, A. M.; Muddiman, D. C. Generation and Detection of Multiply-Charged Peptides and Proteins by Matrix-Assisted Laser Desorption Electrospray Ionization (MALDESI) Fourier Transform Ion Cyclotron Resonance Mass Spectrometry. *J. Am. Soc. Mass Spectrom.* **2006**, *17*, 1712–1716.
(35) Chen, H.; Yang, S.; Wortmann, A.; Zenobi, R. Neutral Desorption Sampling of Living Objects for Rapid Analysis by Extractive Electrospray Ionization Mass Spectrometry. *Angew. Chem. Int. Ed Engl.* **2007**, *46*, 7591–7594.
(36) Haapala, M.; Pól, J.; Saarela, V.; Arvola, V.; Kotiaho, T.; Ketola, R. A.; Franssila, S.; Kauppila, T. J.; Kostiainen, R. Desorption Atmospheric Pressure Photoionization. *Anal. Chem.* **2007**, *79*, 7867–7872.
(37) Na, N.; Zhao, M.; Zhang, S.; Yang, C.; Zhang, X. Development of a Dielectric Barrier Discharge Ion Source for Ambient Mass Spectrometry. *J. Am. Soc. Mass Spectrom.* **2007**, *18*, 1859–1862.
(38) Nemes, P.; Vertes, A. Laser Ablation Electrospray Ionization for Atmospheric Pressure, in Vivo, and Imaging Mass Spectrometry. *Anal. Chem.* **2007**, *79*, 8098–8106.
(39) Ratcliffe, L. V.; Rutten, F. J. M.; Barrett, D. A.; Whitmore, T.; Seymour, D.; Greenwood, C.; Aranda-Gonzalvo, Y.; Robinson, S.; McCoustra, M. Surface Analysis under Ambient Conditions Using Plasma-Assisted Desorption/Ionization Mass Spectrometry. *Anal. Chem.* **2007**, *79*, 6094–6101.
(40) Harris, G. A.; Nyadong, L.; Fernandez, F. M. Recent Developments in Ambient Ionization Techniques for Analytical Mass Spectrometry. *Analyst* **2008**, *133*, 1297–1301.
(41) Van Berkel, G. J.; Pasilis, S. P.; Ovchinnikova, O. Established and Emerging Atmospheric Pressure Surface Sampling/ionization Techniques for Mass Spectrometry. *J. Mass Spectrom. JMS* **2008**, *43*, 1161–1180.
(42) Andre Venter, M. N. Ambient Desorption Ionization Mass Spectrometry. *TrAC Trends Anal. Chem.* **2008**, 284–290.
(43) Rayleigh, L. On The Instability Of Jets. *Proc. Lond. Math. Soc.* **1878**, *s1-10*, 4–13.
(44) Taylor, G. Disintegration of Water Drops in an Electric Field. *Proc. R. Soc. Lond. Ser. Math. Phys. Sci.* **1964**, *280*, 383–397.
(45) Tang, K.; Gomez, A. On the Structure of an Electrostatic Spray of Monodisperse Droplets. *Phys. Fluids* **1994**, *6*, 2317.
(46) Iribarne, J. V.; Thomson, B. A. On the Evaporation of Small Ions from Charged Droplets. *J. Chem. Phys.* **1976**, *64*, 2287.
(47) Videler, H.; Ilag, L. L.; McKay, A. R. C.; Hanson, C. L.; Robinson, C. V. Mass Spectrometry of Intact Ribosomes. *FEBS Lett.* **2005**, *579*, 943–947.

(48) Taylor, G. I.; McEwan, A. D. The Stability of a Horizontal Fluid Interface in a Vertical Electric Field. *J. Fluid Mech.* **1965**, *22*, 1–15.
(49) Cloupeau, M.; Prunet-Foch, B. Electrohydrodynamic Spraying Functioning Modes: A Critical Review. *J. Aerosol Sci.* **1994**, *25*, 1021–1036.
(50) Tang, L.; Kebarle, P. Dependence of Ion Intensity in Electrospray Mass Spectrometry on the Concentration of the Analytes in the Electrosprayed Solution. *Anal Chem* **1993**, *65*, 3654–3668.
(51) Nemes, P.; Marginean, I.; Vertes, A. Spraying Mode Effect on Droplet Formation and Ion Chemistry in Electrosprays. *Anal Chem* **2007**, *79*, 3105–3116.
(52) Hayati, I.; Bailey, A. I.; Tadros, T. F. Investigations into the Mechanisms of Electrohydrodynamic Spraying of Liquids: I. Effect of Electric Field and the Environment on Pendant Drops and Factors Affecting the Formation of Stable Jets and Atomization. *J. Colloid Interface Sci.* **1987**, *117*, 205–221.
(53) Hayati, I.; Bailey, A.; Tadros, T. F. Investigations into the Mechanism of Electrohydrodynamic Spraying of Liquids: II. Mechanism of Stable Jet Formation and Electrical Forces Acting on a Liquid Cone. *J. Colloid Interface Sci.* **1987**, *117*, 222–230.
(54) Tang, L.; Kebarle, P. Effect of the Conductivity of the Electrosprayed Solution on the Electrospray Current. Factors Determining Analyte Sensitivity in Electrospray Mass Spectrometry. *Anal. Chem.* **1991**, *63*, 2709–2715.
(55) Enke, C. G. A Predictive Model for Matrix and Analyte Effects in Electrospray Ionization of Singly-Charged Ionic Analytes. *Anal. Chem.* **1997**, *69*, 4885–4893.
(56) Constantopoulos, T. L.; Jackson, G. S.; Enke, C. G. Effects of Salt Concentration on Analyte Response Using Electrospray Ionization Mass Spectrometry. *J. Am. Soc. Mass Spectrom.* **1999**, *10*, 625–634.
(57) Blades, A. T.; Ikonomou, M. G.; Kebarle, P. Mechanism of Electrospray Mass Spectrometry. Electrospray as an Electrolysis Cell. *Anal. Chem.* **1991**, *63*, 2109–2114.
(58) Van Berkel, G. J.; McLuckey, S. A.; Glish, G. L. Electrospray Ionization of Porphyrins Using a Quadrupole Ion Trap for Mass Analysis. *Anal. Chem.* **1991**, *63*, 1098–1109.
(59) Van Berkel, G. J.; McLuckey, S. A.; Glish, G. L. Electrochemical Origin of Radical Cations Observed in Electrospray Ionization Mass Spectra. *Anal. Chem.* **1992**, *64*, 1586–1593.
(60) *Electrospray and MALDI Mass Spectrometry: Fundamentals, Instrumentation, Practicalities, and Biological Applications*; Cole, R. B., Ed.; 2nd ed.; Wiley: Hoboken, NJ, 2010.
(61) Pozniak, B. P.; Cole, R. B. Current Measurements within the Electrospray Emitter. *J. Am. Soc. Mass Spectrom.* **2007**, *18*, 737–748.
(62) Van Berkel, G. J. Insights into Analyte Electrolysis in an Electrospray Emitter from Chronopotentiometry Experiments and Mass Transport Calculations. *J. Am. Soc. Mass Spectrom.* **2000**, *11*, 951–960.

(63) Van Berkel, G. J.; Giles, G. E.; Bullock, null; Gray, L. J. Computational Simulation of Redox Reactions within a Metal Electrospray Emitter. *Anal. Chem.* **1999**, *71*, 5288–5296.
(64) Pozniak, B. P.; Cole, R. B. Negative Ion Mode Evolution of Potential Buildup and Mapping of Potential Gradients within the Electrospray Emitter. *J. Am. Soc. Mass Spectrom.* **2004**, *15*, 1737–1747.
(65) Van Berkel, G. J.; Zhou, F.; Aronson, J. T. Changes in Bulk Solution pH Caused by the Inherent Controlled-Current Electrolytic Process of an Electrospray Ion Source. *Int. J. Mass Spectrom. Ion Process.* **1997**, *162*, 55–67.
(66) Konermann, L.; Silva, E. A.; Sogbein, O. F. Electrochemically Induced pH Changes Resulting in Protein Unfolding in the Ion Source of an Electrospray Mass Spectrometer. *Anal. Chem.* **2001**, *73*, 4836–4844.
(67) Ijames, C. F.; Dutky, R. C.; Fales, H. M. Iron Carboxylate Oxygen-Centered-Triangle Complexes Detected during Electrospray Use of Organic Acid Modifiers with a Comment on the Finnigan TSQ-700 Electrospray Inlet System. *J. Am. Soc. Mass Spectrom.* **1995**, *6*, 1226–1231.
(68) Smith, D. P. H. The Electrohydrodynamic Atomization of Liquids. *IEEE Trans. Ind. Appl.* **1986**, *IA-22*, 527–535.
(69) López-Herrera, J. M.; Barrero, A.; Boucard, A.; Loscertales, I. G.; Márquez, M. An Experimental Study of the Electrospraying of Water in Air at Atmospheric Pressure. *J. Am. Soc. Mass Spectrom.* **2004**, *15*, 253–259.
(70) Cloupeau, M. Recipes for Use of EHD Spraying in Cone-Jet Mode and Notes on Corona Discharge Effects. *J. Aerosol Sci.* **1994**, *25*, 1143–1157.
(71) Cloupeau, M.; Prunet-Foch, B. Electrostatic Spraying of Liquids in Cone-Jet Mode. *J. Electrost.* **1989**, *22*, 135–159.
(72) Fernández de la Mora, J. The Fluid Dynamics of Taylor Cones. *Annu. Rev. Fluid Mech.* **2007**, *39*, 217–243.
(73) Grimm, R. L.; Beauchamp, J. L. Evaporation and Discharge Dynamics of Highly Charged Droplets of Heptane, Octane, and P-Xylene Generated by Electrospray Ionization. *Anal. Chem.* **2002**, *74*, 6291–6297.
(74) Grimm, R. L.; Beauchamp, J. L. Evaporation and Discharge Dynamics of Highly Charged Multicomponent Droplets Generated by Electrospray Ionization. *J. Phys. Chem. A* **2010**, *114*, 1411–1419.
(75) Davis, E. J.; Bridges, M. A. The Rayleigh Limit of Charge Revisited: Light Scattering from Exploding Droplets. *J. Aerosol Sci.* **1994**, *25*, 1179–1199.
(76) Gomez, A.; Tang, K. Charge and Fission of Droplets in Electrostatic Sprays. *Phys. Fluids* **1994**, *6*, 404.
(77) Taflin, D. C.; Ward, T. L.; Davis, E. J. Electrified Droplet Fission and the Rayleigh Limit. *Langmuir* **1989**, *5*, 376–384.
(78) Rayleigh, Lord. XX. On the Equilibrium of Liquid Conducting Masses Charged with Electricity. *Philos. Mag. Ser. 5* **1882**, *14*, 184–186.
(79) Loscertales, I. G.; Mora, J. F. de la. Experiments on the Kinetics of Field Evaporation of Small Ions from Droplets. *J. Chem. Phys.* **1995**, *103*, 5041–5060.

(80) Thomson, B. A.; Iribarne, J. V. Field Induced Ion Evaporation from Liquid Surfaces at Atmospheric Pressure. *J. Chem. Phys.* **1979**, *71*, 4451.
(81) Davies, C. N. Evaporation of Airborne Droplets. In *Fundamentals of Aerosol Science*; Shaw, D. T., Ed.; Wiley-Interscience: New York, 1978; pp. 135–164.
(82) Fenn, J. B. Ion Formation from Charged Droplets: Roles of Geometry, Energy, and Time. *J Am Soc Mass Spectrom* **1993**, *4*, 524–535.
(83) Zhan, D.; Rosell, J.; Fenn, J. B. Solvation Studies of Electrospray Ions—method and Early Results. *J. Am. Soc. Mass Spectrom.* **1998**, *9*, 1241–1247.
(84) Znamenskiy, V.; Marginean, I.; Vertes, A. Solvated Ion Evaporation from Charged Water Nanodroplets. *J. Phys. Chem. A* **2003**, *107*, 7406–7412.
(85) Gamero-Castano, null; Mora, null. Kinetics of Small Ion Evaporation from the Charge and Mass Distribution of Multiply Charged Clusters in Electrosprays. *J. Mass Spectrom. JMS* **2000**, *35*, 790–803.
(86) Gamero-Castaño, M.; Mora, J. F. de la. Direct Measurement of Ion Evaporation Kinetics from Electrified Liquid Surfaces. *J. Chem. Phys.* **2000**, *113*, 815–832.
(87) Schmelzeisen-Redeker, G.; Bütfering, L.; Röllgen, F. W. Desolvation of Ions and Molecules in Thermospray Mass Spectrometry. *Int. J. Mass Spectrom. Ion Process.* **1989**, *90*, 139–150.
(88) Winger, B. E.; Light-Wahl, K. J.; Loo, R. R. O.; Udseth, H. R.; Smith, R. D. Observation and Implications of High Mass-to-Charge Ratio Ions from Electrospray Ionization Mass Spectrometry. *J. Am. Soc. Mass Spectrom.* **1993**, *4*, 536–545.
(89) Fernandez de la Mora, J. Electrospray Ionization of Large Multiply Charged Species Proceeds via Dole's Charged Residue Mechanism. *Anal. Chim. Acta* **2000**, *406*, 93–104.
(90) Tolić, L. P.; Anderson, G. A.; Smith, R. D.; Brothers II, H. M.; Spindler, R.; Tomalia, D. A. Electrospray Ionization Fourier Transform Ion Cyclotron Resonance Mass Spectrometric Characterization of High Molecular Mass Starburst™ Dendrimers. *Int. J. Mass Spectrom. Ion Process.* **1997**, *165–166*, 405–418.
(91) Iavarone, A. T.; Williams, E. R. Mechanism of Charging and Supercharging Molecules in Electrospray Ionization. *J. Am. Chem. Soc.* **2003**, *125*, 2319–2327.
(92) De La Mora, J. F.; Loscertales, I. G. The Current Emitted by Highly Conducting Taylor Cones. *J Fluid Mech* **1994**, *260*, 155–184.
(93) Smith, J. N.; Flagan, R. C.; Beauchamp, J. L. Droplet Evaporation and Discharge Dynamics in Electrospray Ionization†. *J. Phys. Chem. A* **2002**, *106*, 9957–9967.
(94) Duft, D.; Achtzehn, T.; Müller, R.; Huber, B. A.; Leisner, T. Coulomb Fission: Rayleigh Jets from Levitated Microdroplets. *Nature* **2003**, *421*, 128–128.
(95) Olumee, Z.; Callahan, J. H.; Vertes, A. Droplet Dynamics Changes in Electrostatic Sprays of Methanol–Water Mixtures. *J Phys Chem A* **1998**, *102*, 9154–9160.
(96) Girod, M.; Dagany, X.; Antoine, R.; Dugourd, P. Relation between Charge State Distributions of Peptide Anions and pH Changes in the Electrospray Plume. A

Mass Spectrometry and Optical Spectroscopy Investigation. *Int J Mass Spectrom* **2011**, *308*, 41–48.
(97) Schweizer, J. W.; Hanson, D. N. Stability Limit of Charged Drops. *J. Colloid Interface Sci.* **1971**, *35*, 417–423.
(98) Chen, M.; Cook, K. D. Oxidation Artifacts in the Electrospray Mass Spectrometry of Aβ Peptide. *Anal Chem* **2007**, *79*, 2031–2036.
(99) Kelly, M. A.; Vestling, M. M.; Fenselau, C. C.; Smith, P. B. Electrospray Analysis of Proteins: A Comparison of Positive-Ion and Negative-Ion Mass Spectra at High and Low pH. *Org. Mass Spectrom.* **1992**, *27*, 1143–1147.
(100) Ashton, D. S.; Beddell, C. R.; Cooper, D. J.; Green, B. N.; Oliver, R. W. A. Mechanism of Production of Ions in Electrospray Mass Spectrometry. *Org. Mass Spectrom.* **1993**, *28*, 721–728.
(101) Wang, G.; Cole, R. B. Disparity between Solution-Phase Equilibria and Charge State Distributions in Positive-Ion Electrospray Mass Spectrometry. *Org. Mass Spectrom.* **1994**, *29*, 419–427.
(102) Le Blanc, J. C. Y.; Wang, J.; Guevremont, R.; Siu, K. W. M. Electrospray Mass Spectra of Protein Cations Formed in Basic Solutions. *Org. Mass Spectrom.* **1994**, *29*, 587–593.
(103) Mirza, U. A.; Chait, B. T. Effects of Anions on the Positive Ion Electrospray Ionization Mass Spectra of Peptides and Proteins. *Anal. Chem.* **1994**, *66*, 2898–2904.
(104) Wang, G.; Cole, R. B. Mechanistic Interpretation of the Dependence of Charge State Distributions on Analyte Concentrations in Electrospray Ionization Mass Spectrometry. *Anal. Chem.* **1995**, *67*, 2892–2900.
(105) Schnier, P. D.; Gross, D. S.; Williams, E. R. Electrostatic Forces and Dielectric Polarizability of Multiply Protonated Gas-Phase Cytochrome c Ions Probed by Ion/Molecule Chemistry. *J. Am. Chem. Soc.* **1995**, *117*, 6747–6757.
(106) Schnier, P. D.; Gross, D. S.; Williams, E. R. On the Maximum Charge State and Proton Transfer Reactivity of Peptide and Protein Ions Formed by Electrospray Ionization. *J. Am. Soc. Mass Spectrom.* **1995**, *6*, 1086–1097.
(107) Mansoori, B. A.; Volmer, D. A.; Boyd, R. K. "Wrong-way-round" Electrospray Ionization of Amino Acids. *J Rapid Commun Mass Spectrom* **1997**, *11*, 1120–1130.
(108) Gatlin, C. L.; Turecek, F.; Vaisar, T. Determination of Soluble Cu(I) and Cu(II) Species in Jet Fuel by Electrospray Ionization Mass Spectrometry. *Anal Chem* **1994**, *66*, 3950–3958.
(109) Zhou, S.; Prebyl, B. S.; Cook, K. D. Profiling pH Changes in the Electrospray Plume. *Anal Chem* **2002**, *74*, 4885–4888.
(110) Zhou, S.; Edwards, A. G.; Cook, K. D.; Van Berkel, G. J. Investigation of the Electrospray Plume by Laser-Induced Fluorescence Spectroscopy. *Anal Chem* **1999**, *71*, 769–776.
(111) Zhou, S.; Cook, K. D. Probing Solvent Fractionation in Electrospray Droplets with Laser-Induced Fluorescence of a Solvatochromic Dye. *Anal Chem* **2000**, *72*, 963–969.

(112) Kiselev, P.; Rosell, J.; Fenn, J. B. Determining the Composition of Liquid Droplets in a Gas of Different Composition. *Ind Eng Chem Res* **1997**, *36*, 3081–3084.
(113) Wang, R.; Zenobi, R. Evolution of the Solvent Polarity in an Electrospray Plume. *J Am Soc Mass Spectrom* **2010**, *21*, 378–385.
(114) Peng, X.; Draney, D. R.; Volcheck, W. M.; Bashford, G. R.; Lamb, D. T.; Grone, D. L.; Zhang, Y.; Johnson, C. M. Phthalocyanine Dye as an Extremely Photostable and Highly Fluorescent near-Infrared Labeling Reagent. In; 2006; Vol. 6097, p. 60970E–60970E–12.
(115) Ideue, S.; Sakamoto, K.; Honma, K.; Clemmer, D. E. Conformational Change of Electrosprayed Cytochrome c Studied by Laser-Induced Fluorescence. *Chem. Phys. Lett.* **2001**, *337*, 79–84.
(116) Rodriguez-Cruz, S. E.; Khoury, J. T.; Parks, J. H. Protein Fluorescence Measurements within Electrospray Droplets. *J Am Soc Mass Spectrom* **2001**, *12*, 716–725.
(117) Grandori, R.; Matecko, I.; Müller, N. Uncoupled Analysis of Secondary and Tertiary Protein Structure by Circular Dichroism and Electrospray Ionization Mass Spectrometry. *J. Mass Spectrom. JMS* **2002**, *37*, 191–196.
(118) Wang, H.; Agnes, G. R. Kinetically Labile Equilibrium Shifts Induced by the Electrospray Process. *Anal Chem* **1999**, *71*, 4166–4172.
(119) Schrum, K. F.; Williams, A. M.; Haerther, S. A.; Ben-Amotz, D. Molecular Fluorescence Thermometry. *Anal Chem* **1994**, *66*, 2788–2790.
(120) Lou, J.; Hatton, T. A.; Laibinis, P. E. Fluorescent Probes for Monitoring Temperature in Organic Solvents. *Anal Chem* **1997**, *69*, 1262–1264.
(121) Figueroa, I. D.; el Baraka, M.; Quiñones, E.; Rosario, O.; Deumié, M. A Fluorescent Temperature Probe Based on the Association between the Excited States of 4-(N,N-Dimethylamino)benzonitrile and Beta-Cyclodextrin. *Anal. Chem.* **1998**, *70*, 3974–3977.
(122) Gallery, J.; Gouterman, M.; Callis, J.; Khalil, G.; McLachlan, B.; Bell, J. Luminescent Thermometry for Aerodynamic Measurements. *Rev. Sci. Instrum.* **1994**, *65*, 712–720.
(123) Sakakibara, J.; Adrian, R. J. Whole Field Measurement of Temperature in Water Using Two-Color Laser Induced Fluorescence. *Exp Fluids* **1999**, *26*, 7–15.
(124) Coppeta, J.; Rogers, C. Dual Emission Laser Induced Fluorescence for Direct Planar Scalar Behavior Measurements. *Exp Fluids* **1998**, *25*, 1–15.
(125) Kim, H. J.; Kihm, K. D.; Allen, J. S. Examination of Ratiometric Laser Induced Fluorescence Thermometry for Microscale Spatial Measurement Resolution. *Int J Heat Mass Tran* **2003**, *46*, 3967–3974.
(126) Shelley, J. T.; Wiley, J. S.; Chan, G. C. Y.; Schilling, G. D.; Ray, S. J.; Hieftje, G. M. Characterization of Direct-Current Atmospheric-Pressure Discharges Useful for Ambient Desorption/Ionization Mass Spectrometry. *J. Am. Soc. Mass Spectrom.* **2009**, *20*, 837–844.

(127) Gross, J. H. Direct Analysis in Real Time--a Critical Review on DART-MS. *Anal. Bioanal. Chem.* **2014**, *406*, 63–80.
(128) Cody, R. B. Observation of Molecular Ions and Analysis of Nonpolar Compounds with the Direct Analysis in Real Time Ion Source. *Anal. Chem.* **2009**, *81*, 1101–1107.
(129) Song, L.; Dykstra, A. B.; Yao, H.; Bartmess, J. E. Ionization Mechanism of Negative Ion-Direct Analysis in Real Time: A Comparative Study with Negative Ion-Atmospheric Pressure Photoionization. *J. Am. Soc. Mass Spectrom.* **2009**, *20*, 42–50.
(130) Jorabchi, K.; Hanold, K.; Syage, J. Ambient Analysis by Thermal Desorption Atmospheric Pressure Photoionization. *Anal. Bioanal. Chem.* **2013**, *405*, 7011–7018.
(131) Cristoni, S.; Bernardi, L. R.; Biunno, I.; Tubaro, M.; Guidugli, F. Surface-Activated No-Discharge Atmospheric Pressure Chemical Ionization. *Rapid Commun. Mass Spectrom. RCM* **2003**, *17*, 1973–1981.
(132) Furuya, H.; Kambara, S.; Nishidate, K.; Fujimaki, S.; Hashimoto, Y.; Suzuki, S.; Iwama, T.; Hiraoka, K. Quantitative Aspects of Atmospheric-Pressure Penning Ionization. *J. Mass Spectrom. Soc. Jpn.* **2010**, *58*, 211–213.
(133) Dane, A. J.; Cody, R. B. Selective Ionization of Melamine in Powdered Milk by Using Argon Direct Analysis in Real Time (DART) Mass Spectrometry. *The Analyst* **2010**, *135*, 696–699.
(134) Yang, H.; Wan, D.; Song, F.; Liu, Z.; Liu, S. Argon Direct Analysis in Real Time Mass Spectrometry in Conjunction with Makeup Solvents: A Method for Analysis of Labile Compounds. *Anal. Chem.* **2013**, *85*, 1305–1309.
(135) Song, L.; Zhu; Bartmess, J. E. Ionization Mechanism of Positive-Ion Nitrogen Direct Analysis in Real Time, 2014.
(136) Penning, F. M. Über Ionisation durch metastabile Atome. *Naturwissenschaften* **1927**, *15*, 818–818.
(137) Hiraoka, K.; Ninomiya, S.; Chen, L. C.; Iwama, T.; Mandal, M. K.; Suzuki, H.; Ariyada, O.; Furuya, H.; Takekawa, K. Development of Double Cylindrical Dielectric Barrier Discharge Ion Source. *The Analyst* **2011**, *136*, 1210–1215.
(138) Laramée, J. A.; Cody, R. B.; Nilles, J. M.; Durst, H. D. Forensic Application of DARTTM (Direct Analysis in Real Time) Mass Spectrometry. In *Forensic Analysis on the Cutting Edge*; Chemist, R. D. B. R. former S., Ed.; John Wiley & Sons, Inc., 2007; pp. 175–195.
(139) Fernández, F. M.; Cody, R. B.; Green, M. D.; Hampton, C. Y.; McGready, R.; Sengaloundeth, S.; White, N. J.; Newton, P. N. Characterization of Solid Counterfeit Drug Samples by Desorption Electrospray Ionization and Direct-Analysis-in-Real-Time Coupled to Time-of-Flight Mass Spectrometry. *ChemMedChem* **2006**, *1*, 702–705.
(140) Vaclavik, L.; Cajka, T.; Hrbek, V.; Hajslova, J. Ambient Mass Spectrometry Employing Direct Analysis in Real Time (DART) Ion Source for Olive Oil Quality and Authenticity Assessment. *Anal. Chim. Acta* **2009**, *645*, 56–63.

(141) Petucci, C.; Diffendal, J.; Kaufman, D.; Mekonnen, B.; Terefenko, G.; Musselman, B. Direct Analysis in Real Time for Reaction Monitoring in Drug Discovery. *Anal. Chem.* **2007**, *79*, 5064–5070.
(142) Kebarle, P. A Brief Overview of the Present Status of the Mechanisms Involved in Electrospray Mass Spectrometry. *J Mass Spectrom* **2000**, *35*, 804–817.
(143) Zhou, S.; Cook, K. D. A Mechanistic Study of Electrospray Mass Spectrometry: Charge Gradients within Electrospray Droplets and Their Influence on Ion Response. *J Am Soc Mass Spectrom* **2001**, *12*, 206–214.
(144) Pramanik, B. N.; Ganguly, A. K.; Gross, M. L. *Applied Electrospray Mass Spectrometry*; CRC Press, 2002.
(145) Davis, D.; Portelius, E.; Zhu, Y.; Feigerle, C.; Cook, K. D. Profiling an Electrospray Plume Using Surface-Enhanced Raman Spectroscopy. *Anal Chem* **2005**, *77*, 8151–8154.
(146) Gibson, S. C.; Feigerle, C. S.; Cook, K. D. Fluorometric Measurement and Modeling of Droplet Temperature Changes in an Electrospray Plume. *Anal. Chem.* **2014**, *86*, 464–472.
(147) Haefliger, O. P.; Jeckelmann, N. Direct Mass Spectrometric Analysis of Flavors and Fragrances in Real Applications Using DART. *Rapid Commun. Mass Spectrom.* **2007**, *21*, 1361–1366.
(148) Moffat, A. C.; Cody, R. B.; Jee, R. D.; O'Neil, A. J. Identification of Counterfeit Cialis Tablets by Direct Analysis in Real Time (DART) Time-of-Flight Mass Spectrometry. *J. Pharm. Pharmacol.* **2007**, *59*, A26.
(149) Schurek, J.; Vaclavik, L.; Hooijerink, H. (Dick); Lacina, O.; Poustka, J.; Sharman, M.; Caldow, M.; Nielen, M. W. F.; Hajslova, J. Control of Strobilurin Fungicides in Wheat Using Direct Analysis in Real Time Accurate Time-of-Flight and Desorption Electrospray Ionization Linear Ion Trap Mass Spectrometry. *Anal. Chem.* **2008**, *80*, 9567–9575.
(150) Pierce, C. Y.; Barr, J. R.; Cody, R. B.; Massung, R. F.; Woolfitt, A. R.; Moura, H.; Thompson, H. A.; Fernandez, F. M. Ambient Generation of Fatty Acid Methyl Ester Ions from Bacterial Whole Cells by Direct Analysis in Real Time (DART) Mass Spectrometry. *Chem. Commun. Camb. Engl.* **2007**, 807–809.
(151) Kpegba, K.; Spadaro, T.; Cody, R. B.; Nesnas, N.; Olson, J. A. Analysis of Self-Assembled Monolayers on Gold Surfaces Using Direct Analysis in Real Time Mass Spectrometry. *Anal. Chem.* **2007**, *79*, 5479–5483.
(152) Banerjee, S.; Madhusudanan, K. P.; Khanuja, S. P. S.; Chattopadhyay, S. K. Analysis of Cell Cultures of Taxus Wallichiana Using Direct Analysis in Real-Time Mass Spectrometric Technique. *Biomed. Chromatogr. BMC* **2008**, *22*, 250–253.
(153) Banerjee, S.; Madhusudanan, K. P.; Chattopadhyay, S. K.; Rahman, L. U.; Khanuja, S. P. S. Expression of Tropane Alkaloids in the Hairy Root Culture of Atropa Acuminata Substantiated by DART Mass Spectrometric Technique. *Biomed. Chromatogr. BMC* **2008**, *22*, 830–834.

(154) Yew, J. Y.; Cody, R. B.; Kravitz, E. A. Cuticular Hydrocarbon Analysis of an Awake Behaving Fly Using Direct Analysis in Real-Time Time-of-Flight Mass Spectrometry. *Proc. Natl. Acad. Sci.* **2008**, *105*, 7135–7140.
(155) Song, L.; Gibson, S. C.; Bhandari, D.; Cook, K. D.; Bartmess, J. E. Ionization Mechanism of Positive-Ion Direct Analysis in Real Time: A Transient Microenvironment Concept. *Anal. Chem.* **2009**, *81*, 10080–10088.
(156) Pérez, J. J.; Harris, G. A.; Chipuk, J. E.; Brodbelt, J. S.; Green, M. D.; Hampton, C. Y.; Fernández, F. M. Transmission-Mode Direct Analysis in Real Time and Desorption Electrospray Ionization Mass Spectrometry of Insecticide-Treated Bednets for Malaria Control. *Analyst* **2010**, *135*, 712–719.
(157) Wang, H.; Agnes, G. R. Evaluation of Electrospray Mass Spectrometry as a Technique for Quantitative Analysis of Kinetically Labile Solution Species. *Anal Chem* **1999**, *71*, 3785–3792.
(158) Olumee, Z.; Callahan, J. H.; Vertes, A. Velocity Compression in Cylindrical Capacitor Electrospray of Methanol-Water Mixtures. *Anal Chem 71*, 4111–4113.
(159) De Juan, L.; de la Mora, J. F. Charge and Size Distributions of Electrospray Drops. *J. Colloid Interface Sci.* **1997**, *186*, 280–293.
(160) Chamarthy, P.; Garimella, S. V.; Wereley, S. T. Measurement of the Temperature Non-Uniformity in a Microchannel Heat Sink Using Microscale Laser-Induced Fluorescence. *Int. J. Heat Mass Transf.* **2010**, *53*, 3275–3283.
(161) Synchronous Excitation Spectroscopy. In *Modern Fluorescence Spectroscopy*; Wehry, E., Ed.; Plenum Press: New York, 1981; p. 282.
(162) Novák, A. A Method for Routine Corrections of Inner Filter Effects in Measurements of Excitation and Fluorescence Spectra. *Collect. Czechoslov. Chem. Commun.* **1978**, *43*, 2869–2878.
(163) Hinds, W. C. *Aerosol Technology*; 2nd ed.; John Wiley and Sons, Inc.: New York, 1999.
(164) Wang, R.; Allmendinger, P.; Zhu, L.; Gröhn, A. J.; Wegner, K.; Frankevich, V.; Zenobi, R. The Role of Nebulizer Gas Flow in Electrosonic Spray Ionization (ESSI). *J. Am. Soc. Mass Spectrom.* **2011**, *22*, 1234–1241.
(165) Wilhelm, E.; Battino, R. Estimation of Lennard-Jones (6,12) Pair Potential Parameters from Gas Solubility Data. *J Chem Phys* **1971**, *55*, 4012–4017.
(166) Mikami, S.; Kobayashi, K.; Ota, T.; Fujikawa, S.; Yano, T.; Ichijo, M. Molecular Gas Dynamics Approaches to Interfacial Phenomena Accompanied with Condensation. *Exp Therm Fluid Sci* **2006**, *30*, 795–800.
(167) *CRC Handbook of Chemistry and Physics*; Lide, D. R., Ed.; 86th ed.; CRC Press: Boca Raton, FL, 2005.
(168) Poling, B. E.; Prausnitz, J. M.; O'Connell, J. P. *The Properties of Gases and Liquids*; 5th ed.; McGraw-Hill: New York, 2001.
(169) *Enthalpies of Vaporization of Organic Compounds*; Majer, V.; Svoboda, V., Eds.; 1st ed.; Blackwell Scientific Publications: Oxford, 1985.
(170) NIST Webbook.

(171) Vargaftik, N. B.; Filippov, L. P.; Tarzimanov, A. A.; Totskii, E. E. *Handbook of Thermal Conductivity of Liquids and Gases*; CRC Press, 1993.
(172) Altshuller, A.; Cohen, I. Application of Diffusion Cells to the Production of Known Concentrations. *Anal. Chem.* **1960**, *32*, 802–810.
(173) Chen, N. H.; Othmer, D. F. New Generalized Equation for Gas Diffusion Coefficient. *J Chem Eng Data* **1962**, *7*, 37–41.
(174) Henis, J. M. S. Ion Cyclotron Resonance Study of Ion-Molecule Reactions in Methanol. *J. Am. Chem. Soc.* **1968**, *90*, 844–851.
(175) Harrison, A. G. *Chemical Ionization Mass Spectrometry*; CRC Press: Boca Raton, FL, 1983.
(176) Lias, S. G.; Bartmess, J. E.; Liebman, J. F.; Holmes, J. L.; Levin, R. D.; Mallard, W. G. Gas Phase Ion and Neutral Thermochemistry. *J Phys Chem Ref Data* **1988**, *17*, 18–25.
(177) Wortmann, A.; Kistler-Momotova, A.; Zenobi, R.; Heine, M. C.; Wilhelm, O.; Pratsinis, S. E. Shrinking Droplets in Electrospray Ionization and Their Influence on Chemical Equilibria. *J. Am. Soc. Mass Spectrom.* **2007**, *18*, 385–393.

# Appendix

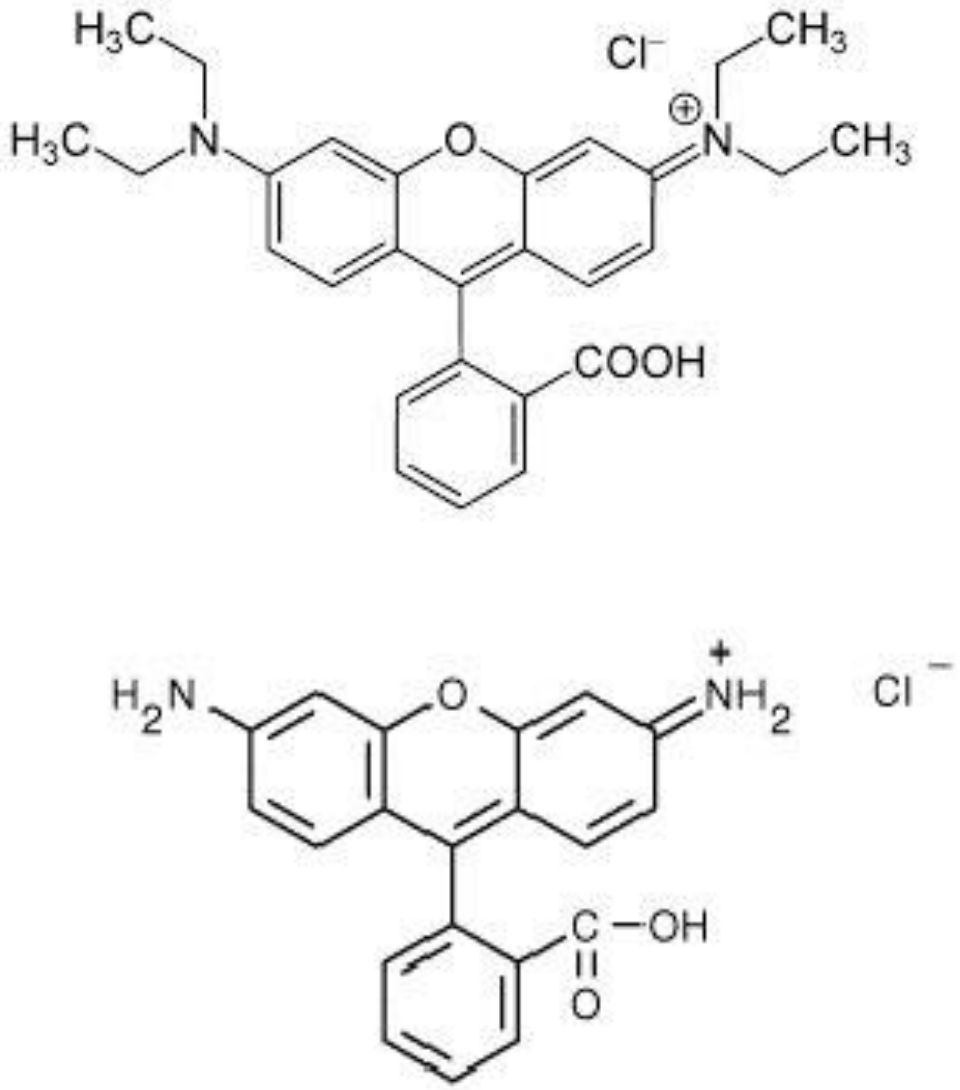


**Figure A.1:** Molecular structures of dyes used in experiments described in Chapter 3. Top: Molecular structure of rhodamine B ($C_{28}H_{31}ClN_2O_3$; molecular weight = 479.02). Bottom: Molecule structure of rhodamine 110 ($C20H15ClN_2O_3$; molecular weight = 366.80).

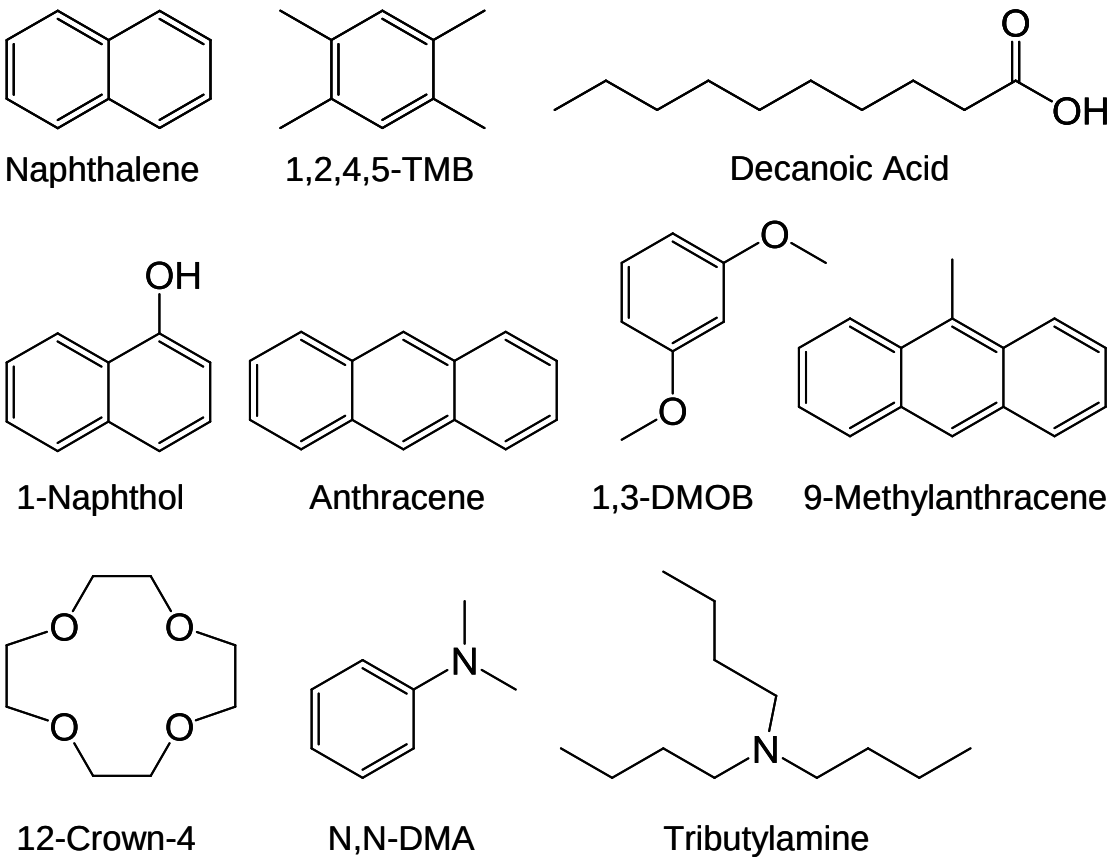


**Figure A.2:** Molecular structures of analytes used in Chapter 4.

**Section A-1**: Estimation of PA values.

The PA of an $[S\text{-}H]^{\cdot}$ radical was calculated as follows, from enthalpies of formation, IEs, and bond dissociation energies (BDEs):

$$PA(A\cdot) = \Delta_fH^o(A\cdot) + \Delta_fH(H^+) - \Delta_fH(AH^{+\cdot})$$

$$\Delta_fH^o(A\cdot) = BDE(A\text{-}H) - \Delta_fH^o(H\cdot) + \Delta_fH^o(AH)$$

$$\Delta_fH^o(AH^{+\cdot}) = \Delta_fH^o(AH) + IE(AH)$$

thus $PA(A\cdot) = BDE(A\text{-}H) - \Delta_fH^o(H\cdot) + \Delta_fH^o(AH) + \Delta_fH(H^+) - \Delta_fH^o(AH) + IE(AH)$

$$= BDE(A\text{-}H) + IE(H.) + IE(AH)$$

This ignores the fact that IEs are 0 K quantities, while BDEs and PAs are 298 K quantities. There should be only a small temperature effect on IEs, however, because the integrated heat capacities of AH and $AH^{+\cdot}$ should approximately cancel, due to their similar structures.

The PA corresponding to an $S_2H^+$ ion can be taken as the PA of the monomer plus the binding enthalpy of the proton-bound dimer, $\Delta H_{01}(S..SH^+)$. This assumes that on proton loss, the conjugate base of $S_2H^+$ is two free bases, and not a neutral dimer. Neutral dimer binding enthalpies are typically 10-20 kJ/mol, but entropy favors separation into two free S species on proton loss. In addition, $\Delta H_{01}(S..SH^+)$ is roughly constant at 130±8 kJ/mol for the range of bases here. This is because for constant structure at the binding site of OH+..O, as the monomer S becomes a stronger base and thus stronger hydrogen bond acceptor, its conjugate acid $SH^+$ becomes a weaker hydrogen bond donor. These effects roughly cancel to give a near

constant $\Delta H_{01}$. For those bases where $\Delta H_{01}(S..SH^+)$ is not known, we assign the PA of the dimer as that of the monomer plus 126 kJ/mol, the experimental value of $\Delta H_{01}(S..SH^+)$ for acetone.[170]

## Vita

Stephen Colin Gibson was born in Newark, NJ on September 18th, 1984 and was raised in Franklin, TN. He graduated from Centennial High School in Franklin, TN in 2002 and began his undergraduate career at Western Kentucky University that fall. Stephen graduated with his B.S. in chemistry and a minor in mathematics and biology in the spring of 2007. He began his graduate career in focusing in Analytical Chemistry at the University of Tennessee under Dr. Kelsey Cook and Dr. Charles Feigerle. Stephen defended his dissertation in July 2014 and will graduate in December 2014 with his Ph.D. in Analytical Chemistry.